ESA ESTEC
Keplerlaan 1
2201 AZ Noordwijk
The Netherlands

EE11 WIVERN MISSION
MISSION REQUIREMENTS DOCUMENT (MRD)

Prepared by	The WIVERN Mission Team ESTEC
Document Type	Requirement Document (Mission)
Reference	EOP-XXX/XXXX-XX-XXX/XXX/xxx
Issue/Revision	1.0
Date of Issue	01/08/2025
Status	Draft

APPROVAL

Title	EE11 WIVERN MISSIONMISSION REQUIREMENTS DOCUMENT (MRD)		
Issue Number	1	Revision Number	0
Author	The WIVERN Mission Team	Date	01/08/2025
Reviewed by		Date of Review	
Approved by		Date of Approval	
P.Martimort			

CHANGE LOG

Reason for change	Issue Nr.	Revision Number	Date
Initial draft with inputs from MATER and EOP Generic SSRD	0	1	20/11/2023
Preiliminary issue	0	1	
Second revision	0	2	
Third revision	0	3	07/06/2024
Fourth revision	0	3	26/08/2024
First issue	1	0	01/08/2025

CHANGE RECORD

Issue Number 1	Revision Number 0		
Reason for change	Date	Pages	Paragraphs(s)
Initial draft by ESA. Split of MATER requirements into MRD and SRD. Added EOP Generic SSRD requirements, with tailoring for the WIVERN mission	20/11/2023	all	all
Observation and measruements requirements updated. Section about data products reworked	07/06/2024	all	all
Minor revision. Observation and measruements requirements updated.	07/06/2024	all	all
Updates of scientific background & justification, research objectives and observation requirements to align with the Report for Mission Selection. Addition of the ocean products in the data products section.	01/08/2025	all	all

DISTRIBUTION

Name/Organisational Unit

Table of Contents

1. INTRODUCTION AND EE11 BACKGROUND

1.1. Scope and Organisation of the Document

This document establishes the mission requirements applicable to the WIVERN mission. This document, together with the System Requirements Document (SRD), supersedes the MATER document that was applicable in Phase 0. The WIVERN MRD is managed by the Phase 0/A Mission Scientist according to the ESA internal QMS procedure.

The MRD presents the scientific goals and mission objectives, and specifies the mission requirements, as outlined in [RD-7], and it comprises scientific inputs received from the MAG and the SCience Requirements and Consolidation (SciRec) study. The SRD presents the system level requirements to be used for the mission design, specification, development, testing and verification. The SRD is established by the engineering team supporting the ESA Phase 0/A Study Manager, and takes into consideration both technical and programmatic constraints emerging from the industrial studies.

The requirements in this document are expressed as follows:

ZZZ-YYY

The requirement text is in special style paragraph, with a unique identifier. Where relevant, there are references to documents [AD], [RD], terms [def], or standard [ECSS-M-ST-10C].

Note: Added here any note to the requirement in italic style paragraph

Confidence Level :	number of sigma
Goal/Threshold :	”T” for Threshold or ”G” for Goal
Justification :	justification text to the requirement is provided in a normal style paragraph
Old MATER ID :	MRD-XXX

The requirements identifiers format is **ZZZ-YYY** where **YYY** is a unique number and **ZZZ** indicates the applicable mission level according to the following convention:

- **MIS**: System-wide Mission Requirements
- **OBS**: Observation Requirements
- **MSR**: Measurement Requirements
- **DAT**: Data Products Requirements

A requirement uses the word “shall” to request a specific function of performance. Where the required function or performance can have several features or values presenting a range of possible corresponding concepts, two separate requirements will be written, with the second duplicating the first except with the word “may” instead of shall and the alternative feature, value,

or range thereof.

Performances shall be reported for design options meeting the threshold, breakthrough and goal requirements. The baseline requirement to be used for the Phase A system studies shall be the Breakthrough requirements if provided. Otherwise, the threshold shall be considered.

All references shall be noted as [RD-XX] and included in section 1.3.2, where XX indicates the reference number. Scientific references are, furthermore, repeated in a bibliography style in Annex A (Author, date).

1.2. EE11 Programmatic background

Earth Explorer (EE) missions form the science and research element of the dual-strategy Living Planet Programme, which also includes the operational service-oriented Earth Watch missions. The Earth Explorer missions focus on the atmosphere, biosphere, hydrosphere, cryosphere and the Earth's interior with emphasis on the interactions between these components and on the impact that human activities have on the Earth's processes. More background on the Earth Explorer missions is available in [RD-2] and [RD-6].

WIVERN is a candidate for the 11th selection cycle (EE11), which started with a Phase 0 study as per the phasing of ESA projects [RD-3]. At the end of the Phase 0, WIVERN together with CAIRT have been selected to be move to the next step of a Phase A feasibility study, for which the current document provides the mission requirements. Ultimately, one of the two missions will be selected for implementation. Further to the requirements, the programmatic constraints applicable to EE11 are:

- Ceiling cost of 250 M€ at 2020 economic conditions for the industrial development cost for the space segment, from Phase B to Phase E1 [RD-3], both included, excluding launcher procurement, FOS adaptation, in-orbit operations, generic ground segment, Ground processors.
- Establishment of mission feasibility and definition of system and sub-systems as per by the start of the Preliminary Requirements Review as per [RD-3] i.e. at the end of Phase A.
- A sufficient technology readiness as per [RD-4] so that a minimum Technology Readiness Level (TRL) of 5 is achieved at the end of Phase B1, and TRL 6 by the end of Phase B2, especially for the payload elements and any other critical technology. TRL 4 will also be targeted for critical elements at the end of Phase A.
- A sufficient Science Readiness as per [RD-3] so that a minimum Science Readiness Level (SRL) of 4 by the end of Phase 0 and SRL 5 by the end of Phase A.
- Start of Phase B1 by the fall of 2026, launch by the end of 2031/2032.

- Launch shall be nominally assumed with a VEGA-C launcher.
- Use of ESA rules and standards for management and procurement, customised for EE11.
- Another constraint was initially set on in-kind contributions, but it is not relevant for the WIVERN candidate.

1.3. Tracked Changes

This document is a clean version, so track changes have been suppressed.

1.3.1. Applicable Documents (ADs)

The following documents, listed in order of precedence, contain requirements applicable to the definition of the requirements. The applicable documents are identified as [AD-xx].

[AD-1]	Guidelines for the computation of Delta-V and propellant budget, EOP-FM-2024-07-177, v3.0
[AD-2]	ESA's Space Debris Mitigation Requirements, ESSB-ST-U-007, v1.0
[AD-3]	Replaced by [RD-53]
[AD-4]	Re-entry Safety Requirements, ESSB-ST-U-004, v1.0
[AD-5]	Guidelines for the computation of the end to end data flow analysis. EOP-ΦM/2021-11-2321, v1.0 (available at later update of the document)
[AD-6]	Vega-C User Manual, issue draft + updated chapters 2,3,4 ref DC/BD/ST/VBA/MBE/L/22-03)
[AD-7]	Ariane-6 User Manual, Issue 2, Revision 0, February 2021
[AD-8]	Replaced by [SD-48]
[AD-9]	WIVERN Mission Statement of Work
[AD-10]	Generic Operations Interface Requirements Document, ESA-GEN-OPS-RS-0002, issue 1.0, 25 May 2023
[AD-11]	Copernicus Expansion Product Assurance and Safety Requirements Phase B2/C/D/E1, CSCE-RS-ESA-PA-0002, issue 3.0
[AD-12]	Guidelines for DeltaV and propellant budget computation for B2CDE, EOP-ΦMP/2019-07-2155/AG/ag, issue 1
[AD-13]	Copernicus Expansion tailoring and verification items for ECSS Engineering standards (platform), CSCE-RS-ESA-SY-0003, Issue 3.0
[AD-14]	Sentinels HPCM Security Package IRD, COP-IC-ESC-FS-3800, issue 1.1 LIMITED DISTRIBUTION DOCUMENT
[AD-15]	Design for Removal – Interface Requirement Document for LEO missions, ESAOPS-SC-RD-2023-001, issue 1.0

1.3.2. Reference Documents (RDs)

The following list contains all references used in this document. Scientific references are provided separately in a bibliography style in Appendix B.

The reference documents are identified as [RD-xx]. Reference documents provide additional

information; they do not form part of the Agency's requirements.

[RD-1]	WIVERN, A WInd VElocity Radar Nephoscope for observing global winds, clouds and precipitation, EE11/01, proposal submitted to ESA in response to the Call for Earth Explorer-11 Mission Ideas, 4 December 2020
[RD-2]	The Future Earth Observation Programme FutureEO Period-1, Call for Earth Explorer 11 Mission Ideas, ESA/EXPLORER/EE11
[RD-3]	Replaced by [SD-100]
[RD-4]	Replaced by [SD-101]
[RD-5]	EOP-SM/2776 Iss 1 Rev 1 Science Readiness Level (SRL) Handbook
[RD-6]	ESA SP-1329(2) ESA's Living Planet Programme - Challenges and Achievements
[RD-7]	ESA-EOP-QMS-PR-2050, v5.0 Appendix 3 of ESA Earth Observation Procedure for Mission Requirements Management
[RD-8]	AE-RP-ESA-SY-001 / EOP-SM/2047/AGS, v2.0 ADM-Aeolus Mission Requirements Document
[RD-9]	EC-RS-ESA-SY-012 / EOP-SM/1567/TW, v5.0 EarthCARE Mission Requirements Document
[RD-10]	ESA-EOPSM-AEOL-TN-3695, v1.1 Aeolus SAG recommendations for operational Doppler Wind Lidar (DWL) observation requirements in the 2030-2040 timeframe
[RD-26]	EO-MA-DMS-GS-0001 Is. Rev. 4.20, 30/11/2020 - Earth Observation Mission CFI Software - CONVENTIONS DOCUMENT
[RD-27]	World Geodetic Standard 84 (WGS84)
[RD-30]	EO-MA-DMS-GS-0018 Iss.4.20 30/11/2020 Earth Observation Mission CFI Software MISSION SPECIFIC CUSTOMIZATIONS
[RD-31]	Replaced by [SD-102]
[RD-32]	Replaced by [SD-49]
[RD-33]	ESA web site on Pointing Error Engineering http://peet.estec.esa.int/ Application examples (PointingSat) and the Pointing Error Engineering Tool (PEET).
[RD-34]	ADVANCED ENCRYPTION STANDARD (AES), FIPS PUB 197, NIST

continued on next page...

...continued from previous page

[RD-35]	Recommendation for Block Cipher Modes of Operation: The CMAC Mode for Authentication, NIST Special Publication 800-38B
[RD-36]	SAVOIR Functional Reference Architecture, SAVOIR-TN-001, Issue-2, 5th April 2016
[RD-37]	Low Earth Orbit (LEO) 26 GHz (K-band) Study Group, Final Report, prepared by LEO26SG (sub-group) of Interagency Operations Advisory Group (IOAG), Nov. 2016.
[RD-38]	Definition and E2E Analysis for the use of ACM techniques in the 26 GHz Downlink in future EO Missions, “Final Report” ESA Contract 4000111232, 26-July-2016
[RD-39]	Cross Support Reference Model—Part 1: Space Link Extension Services, CCSDS 910.4-B-2 (October 2005)
[RD-40]	OPS Angle Definition & Calculation. PE-TN-ESA-SY-338, 25th Sept 2012
[RD-41]	Registration, Evaluation and Authorization of Chemicals (REACh): both the Candidate List (http://echa.europa.eu/web/guest/candidate-list-table) and the Authorisation List (http://echa.europa.eu/addressing-chemicals-ofconcern/authorisation/recommendation-for-inclusion-in-the-authorisationlist/authorisation-list)
[RD-42]	Restriction of Hazardous Substances (RoHS): http://www.rohsguide.com/rohssubstances
[RD-43]	EU Critical Raw Material List: http://eur-lex.europa.eu/legalcontent/EN/TXT/PDF/?uri=CELEX:52014DC0297&from=ENs
[RD-44]	ESSB-HB-U-005 Is. 1, Space system Life Cycle Assessment (LCA) guidelines, 31st Oct 2016
[RD-45]	Zero Debris – Applicability to SSO EO Missions – batch 1, ESA-TECSYE-TN-2023-001205, 24/04/2023
[RD-48]	COP-RS-ESA-SY-0067 Iss.1, Rev.0, EOP Generic SSRD Inputs for Ph B2CDE1. Date of Issue 23/06/2023.

continued on next page...

...continued from previous page

[RD-52]	Coordination Agreement between the European Space Agency (ESA) and the Scientific Committee on Frequency Allocations for Radio Astronomy and Space Science (IUCAF) on the mutual planning procedure for EESS (active) cloud profile radar operations with radio astronomy service observations in the band 94-94.1 GHz between EARTHCARE and IUCAF, version 2, January 2022.
[RD-53]	Space Debris Mitigation Compliance Verification Guidelines, ESSB-HB-U-002, v2.0
[RD-54]	Earth Explorer 11 Candidate Mission WIVERN Report for Mission Selection, ESA-EOPSM-WIVE-RP-4798, 06/06/2025.

All applicable ECSS standards are available for download at: http://www.ecss.nl.

CCSDS documents are available at: https://public.ccsds.org/Publications/AllPubs.aspx

In case of conflicts between this document and the applicable documents the conflict shall be brought to the attention of the Agency for resolution. The latest issue of the applicable document shall apply, unless otherwise stated.

1.4. Terms and Definitions

A summary of definitions valid for this document is given here. The definitions for accuracy, bias, instrument related observation errors and precision are based on ISO standard 3534-1 (ISO, 1993).

Accuracy
The closeness of agreement between a measurement and the accepted reference value. The term accuracy, when applied to a set of measurements, involves a combination of random components and a common systematic error or bias component, and can be expressed as follows:
Eq. 1. Accuracy $= \sqrt{(\text{Precision}^2 + \text{Bias}^2)}$

Bias
The difference between the expectation of measurements and the accepted reference value. The bias is the total systematic error. There may be one or more systematic error components contributing to the bias

Breakthrough
Level at which the observations result in a significant improvement for the target application (e.g. significant positive NWP impact). The breakthrough level may be considered as an optimum, from a cost-benefit point of view, when planning or designing observing systems

Field-of-View or Look angle γ
For the WIVERN conically scanning radar instrument, the Look angle (γ) is the angle between the local nadir to the WGS84 Earth model and the nominal direction of the antenna boresight. The Instrument Field of View (FoV) is the angle of the cone of the radar scan and in nominal conditions, it equals to twice the Look angle.

Geocentric Nadir and Geodetic Nadir

- Geocentric nadir is defined as the line from the satellite centre of mass to the centre of the Earth.
- Geodetic nadir is defined as the line from the satellite centre of mass to the perpendicular of the reference ellipsoid tangent using the WGS-84 model [RD-27].

When nadir is mentioned, it shall be always specified whether it is the geocentric or the geodetic nadir.

Goal
Maximum requirement level, beyond which a significant further improvement in the target application is not expected

Incidence Angle (θ)
The local incidence angle, calculated in a target position, is the angle between the local nor-

mal to the WGS84 Earth model and the line connecting the target position to the origin of the instrument reference frame.

Requirements Level Definition (see also Table DAT-3 for a more detailed definition):

Level 0
Instrument source packet (ISP) data with raw measurement data, i.e. I and Q and noise power, instrument housekeeping data and platform housekeeping data, sampling grid information, calibrated housekeeping data and instrument health parameters

Level 1A
Reconstructed, unprocessed measurement data at full resolution, time-referenced, and annotated with ancillary information, including radiometric and geometric calibration coefficients and georeferencing parameters (e.g., platform ephemeris) computed and appended but not applied to the Level 0 data (or if applied, in a manner that Level 0 is fully recoverable from Level 1 data).

Level 1B
Derived, internally calibrated products:

- Line-of-Sight (LOS) Doppler speed, corrected for satellite velocity and mis-pointing
- Reflectivities and polarimetric variables
- Internally calibrated brightness temperature

Level 2A
Externally calibrated Level 1B products by applying auxiliar information (AUX_MET) from NWP models (ECMWF model). The derived Gas attenuation profile, Feature mask and Hydrometeor Identification shall be included as well.

Level 2B
Derived geophysical variables (e. g., Horizontally projected Line-of-Sight (HLOS) wind, Ice Water Content (IWC), Liquid Water Path (LWP), etc.) at the same resolution and location as Level 1 data.

Level 3
Variables mapped on uniform spacetime grid scales, usually with some completeness and consistency (e. g., missing points interpolated, complete regions mosaicked together from multiple orbits, etc.).

Measurement
Mission observable / data at Level 0 and Level 1

Mission Objective
Related to the mission itself and traceable to the Scientific Objective. Can be achieved by

using primarily data from the mission with limited use of (retrieval) models and auxiliary data files during the mission lifetime. In general, a Mission Objective is related to a data product at Level 1, 2, or 3 and shall be achieved in Phases E1 or E2 (SRL 7 & 8).

Mission Requirement
A requirement related to the mission activity and its scientific/user goals and objectives (e.g. including measurement and observation requirements)

Observation
Mission observable / data at Level 2 and higher, i.e. geophysical parameters

Performance and Knowledge Error Indices
Performance specifications and error budgets shall follow as much as possible the conventions from [AD-08] and [RD-31]. Specifically, for the definition of the following terms, the ones contained in [AD-08] and [RD-31] shall apply:

- Absolute Performance Error (APE)
- Mean Performance Error (MPE)
- Relative Performance Error (RPE)
- Performance Stability Error (PSE)
- Performance Drift Error (PDE)
- Performance Reproducibility Error (PRE)
- Absolute Knowledge Error (AKE)
- Mean Knowledge Error (MKE)
- Relative Knowledge Error (RKE)

Also statistical interpretations of uncertainty budgets (temporal/ensemble/mixed) are defined in the same documents.
To complement the information in [AD-08] and [RD-31], the ESA Pointing Error Engineering Handbook [RD-32] gives more detailed information specifically for the creation of pointing budgets, and is compatible with [AD-08] and [RD-31]. [RD-32] goes into more detail and provides detailed instructions for the pointing engineering process, from identifying sources, making transfers to pointing errors, to handling probability distributions and statistics under the different statistical interpretations. It also contains the summation rules that can be applied in each case.

Precision
The closeness of agreement between independent test results obtained under stipulated conditions. It depends only on the distribution of the random errors. It is computed as the standard deviation of the measurements

Probability of gross error
The complement to unity of the percentage of estimates (bad estimates) contained in the pedestal of uniform distribution over the observation range. Estimates outside the search window should always be considered 'bad' and thus rejected. It is expected that the on-ground data processing will be able to remove most gross-errors through quality control (QC). The requirement in this document refers to the maximum amount of gross errors not being detected by the data processing and QC

Radar return power unit
The return power detected by the radar shall be expressed in terms of the power relative to the power from a single 1mm liquid raindrop present in a concentration of one per cubic meter at the range sampled by the radar which is defined as having an effective reflectivity of 1 mm^6 m^{-3}. Accordingly, the units for the return power signal shall be expressed in units of dBZ relative to a target with a Z of 1 mm^6 m^{-3}

Random error
The closeness of agreement between independent test results obtained under stipulated conditions. It is computed as the standard deviation of the measurements (see definition of precision)

Revisit time
The time elapsed between two consecutive overpasses such that a given area on ground (or at a given altitude of reference) is completely within the instrument FoV, under any acquisition geometry.
Note: to be considered into the statistics of revisit time, it is sufficient that a given point is covered by the Instrument FoV or, equivalently, by the swath. This definition of revisit time does NOT constrain the intersection of the cycloid track with the same exact location on ground.
The mean revisit time refers to the revisit time averaged in time and in longitude. Therefore, a statistics for each latitude can be computed.
The maximum revisit time refers to the maximum in both space and time.

Scientific goal/objective
Related to broad scientific challenges or questions, e.g. as defined in a strategy document. Can be achieved by combining models, observations and measurements from many different sources at any point in time in Phases E1, E2, or F (SRL 8 & 9).

Swath
The swath width is the across-track extent of the intersection of the Instrument FoV with the Earth reference ellipsoid.

System Requirement
A requirement related to any hardware or software of the Observation or Processing System (e.g. including system, instrument, operations, and data processing requirements).

Systematic error
Originated from the instrument and platform characterization, calibration and data processing. In the case of WIVERN, this will include biases due to undetected/uncorrected instrument mis-alignments, platform miss-pointing and errors in the instrument response calibration.

Time period definitions:

Short term:
Time between the emission of each pulse pair

Medium term:
To be defined

Long term:
To be defined

Threshold
Minimum requirement level ensuring useful data (e.g., resulting in neutral or small positive NWP impact)

Trueness
The closeness of agreement between the average value obtained from a large series of measurements and an accepted reference value. The measure of trueness is in the document expressed in terms of bias

WGS84
World Geodetic System. Earth reference coordination system, including a reference ellipsoid, a standard coordinate system, altitude data, and a geoid. Origin is defined at the Earth's centre mass

2. THE WIVERN MISSION

Gaining insight into the dynamics of cloud systems is central to advancing our understanding of storms, clouds and their feedbacks, as well as precipitation, and is key to improving weather prediction, hazard preparedness, and climate modelling. Winds within clouds play a crucial role in governing clouds structure, precipitation processes, storm intensifications and the vertical transport of moisture and energy. Yet, despite their importance, winds within clouds remain unobserved.

The atmosphere has motions on all scales, but for most of them, especially within cloud systems, we have no direct observation of the wind strength and its three-dimensional structure. This represents a critical gap in the global observing system and in our understanding of cloud dynamics and processes.

The WIVERN (WInd VElocity Radar Nephoscope) mission addresses this long-standing gap by delivering the first-ever global observations of horizontal and vertical wind profiles within clouds. Using a cutting-edge conically scanning, polarimetric Doppler radar operating at W-band (94 GHz), sampling an 800 km swath, Wind Velocity Radar Nephoscope (WIVERN) will provide unprecedented three-dimensional wind measurements across a wide range of scales, from 1 to 1000 km, from the tropics to high latitudes (up to ±86°). These capabilities represent a major step forward in Earth observation.

In addition to wind profiling, WIVERN will also contribute to the observation of cloud microphysics, and precipitation processes. The collocated measurement of wind profiles alongside cloud and precipitation properties is a distinctive feature of the mission, and will drive key scientific advancements in areas such as understanding storms, constraining clouds and precipitation impact on climate, and improving Numerical Weather Prediction and Earth System Models.

Beyond its primary science objectives, WIVERN will also contribute to two additional areas of Earth science: sea ice and snow, as well as ocean currents. With its unique simultaneous radar and radiometer measurements at 94 GHz, WIVERN will deliver high spatial resolution, multiple sub-daily observations of sea ice concentration and snow properties over sea ice, which are critical for regulating Arctic heat fluxes and influencing climate feedbacks.

Also, by providing the first routine Doppler Frequency Shift observations of the ocean surface, WIVERN offers a new potential to reveal aspects of ocean current dynamics that cannot be captured by satellite altimetry. WIVERN will further provide unique collocated measurements of atmospheric wind profiles and ocean surface kinematics, opening up new opportunities to monitor ocean-atmosphere interactions.

In summary, WIVERN represents a transformative step in Earth observation by addressing one of the most significant blind spots in the global observing system: the three-dimensional wind

fields within clouds. Its innovative measurement capabilities advance the scientific understanding of storms, clouds, and their role in the climate system. Its wide-ranging benefits, spanning atmosphere, cryosphere, and ocean science, make it a truly multidisciplinary mission with far-reaching societal impact.

3. BACKGROUND AND SCIENTIFIC JUSTIFICATION

3.1. Clouds, Storms, Climate, and Forecasts: Seeing the Bigger Picture

The Earth continues to warm! The Copernicus Climate Change Service (C3S) (2025) has reported:

> "2024 is confirmed to be the warmest year on record globally, and the first calendar year that the average global temperature exceeded 1.5°C above its pre-industrial level."

As the climate warms, the frequency and intensity of storms is expected to change, precipitation patterns shift and extreme weather events are expected to become more frequent and more severe (Intergovernmental Panel on Climate Change (IPCC), 2021).

In the context of the rapidly changing global climate, a key question for individuals is how the climate will change where they live, and the events most people worry about are the extremes. For example, will Valencia in Spain or the Eifel catchment in Germany experience even more intense rainfalls than the previous years? Where are cyclones most likely to make landfall in the future? These questions are rooted in the direct societal impacts of climate extremes, especially those associated with storms.

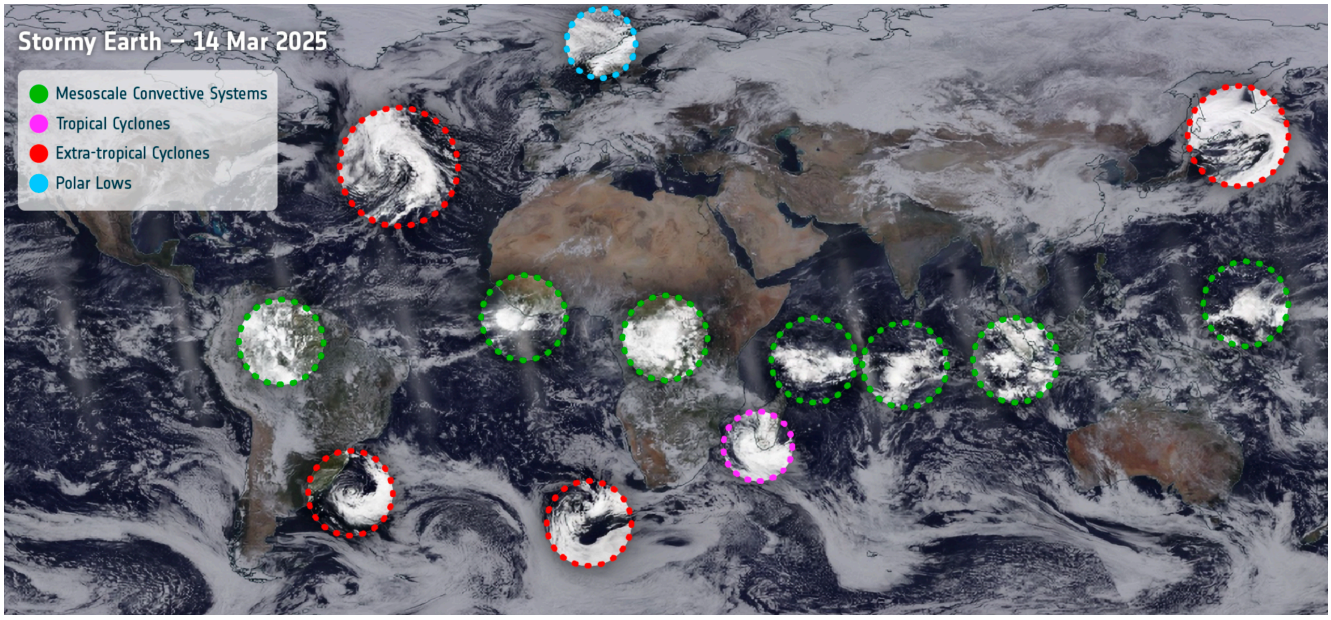

Figure 1: Stormy Earth. Satellite imagery showing a range of storm types, including Tropical Cyclones (TCs), extratropical cyclones, Mesoscale Convective Systemss (MCSs), and polar lows, highlighting the widespread and dynamic nature of atmospheric circulation across the globe on a single day, 14 March 2025. For better visibility, not all the occurrences of a category have been shown.

Storms (Figure 1), ranging from summer thunderstorms and mesoscale convective systems to

tropical cyclones, extratropical cyclones, and polar lows, produce most precipitation on Earth. They can be very localised, occurring on the scale of a European city, or extend over thousands of kilometres. These storms are widespread across the globe at all times, shaping local weather patterns and producing extreme events. Understanding how rainfall patterns and extremes are changing, and why, requires insight into storm dynamics, particularly how air moves within these systems. The timing, location, thermodynamic phase, and amount of precipitation formed are driven by the movement of air within the storm, both horizontally and vertically.

Storms become visible on geostationary satellite imagery through the extensive cloud systems that accompany them, systems that often extend far beyond the regions where precipitation occurs. These clouds influence storm dynamics and are also key components of the climate system, affecting the Earth's energy balance and shaping the planet's response to rising CO_2 concentrations. Their response to warming remains one of the largest sources of uncertainty in climate projections, as repeatedly highlighted by reports from the Intergovernmental Panel on Climate Change (IPCC). Some of these clouds, such as high-level ice clouds, are directly embedded within storms and influenced by their dynamics. Others, including the frequently studied shallow cumuli and stratocumuli, are linked to the descending branch of large-scale circulation, which balances the upward motion within storms. As demonstrated in recent assessments (Sherwood et al., 2020), reducing uncertainty in cloud feedbacks requires integrating multiple lines of evidence, including direct observations and a robust physical understanding.

Despite decades of climate modelling, many of the regional fingerprints of global warming came as a surprise (see examples provided in Figure 2, and Shaw et al. 2024; Shaw and Stevens 2025; Simpson et al. 2025). The ability to anticipate future shifts in regional precipitation patterns or extremes remains limited. This highlights how closely storms, clouds, and precipitation are linked across different scales, and the gaps that still exist in our understanding, modelling tools and observations.

The key challenge lies in the intrinsic link between water, heat, and circulation, which together drive motions across all scales. Within storms, air moves dynamically as water vapour condenses, releasing latent heat that drives vertical motion. This process, known as diabatic heating (see Infobox 3.1), reinforces storm development by altering local pressure fields, sustaining uplift, and generating horizontal circulation patterns whose scale depends on the size of the diabatic heating perturbation. In other words, small-scale motions can self-organise and cascade upscale (see Infobox 3.2, and Figure 3 b). The traditional assumption that large-scale flows can be modelled independently of small-scale processes is increasingly being challenged (Shaw and Stevens, 2025). In the tropics, theoretical studies have demonstrated how small-scale systems can organise into mesoscale, influencing intraseasonal variability (Emanuel et al., 2014; Zhang et al., 2020). In the midlatitudes, interactions between water, heat, and circulation at the mesoscale are crucial, not only for extreme precipitation but also for the persistence of dry conditions and heatwaves (Neal et al., 2022; Röthlisberger and Papritz, 2023). The mesoscale,

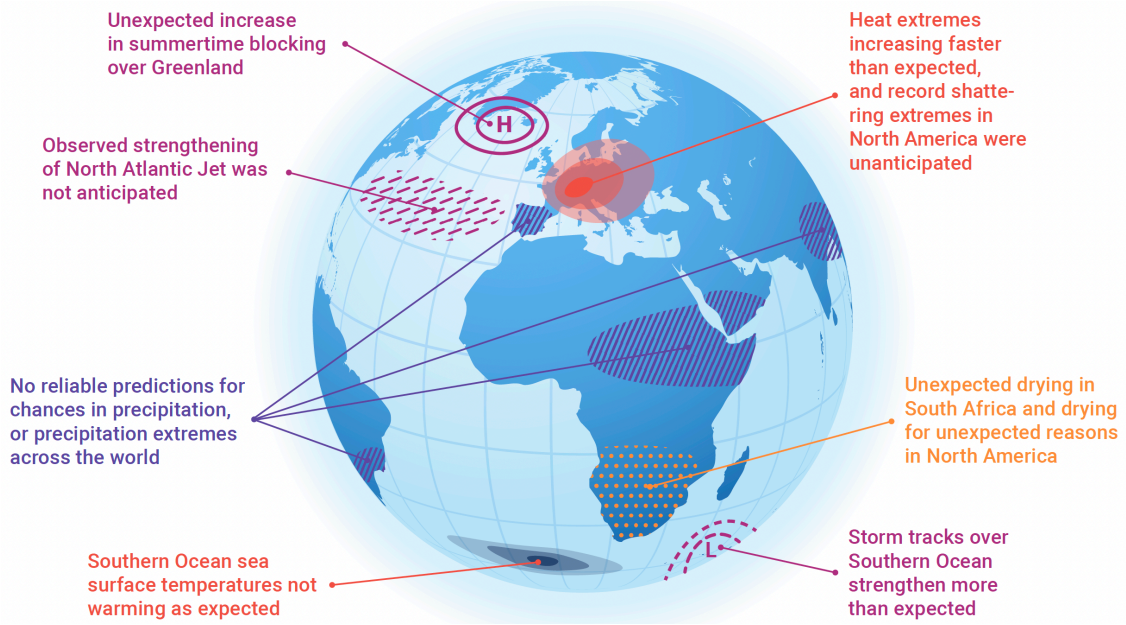

Figure 2: Schematic representation highlighting regions with persistent discrepancies between real-world observations and state-of-the-art climate model predictions, illustrated here for the Atlantic sector. While climate models perform well at the global scale, uncertainties remain at regional scales. Similar issues are found across other regions of the globe. Adapted from Shaw and Stevens (2025).

long neglected in global observing systems, emerges as the critical link between small scales (up to 10 km) and large-scale (larger than 1000 km) circulations.

Infobox 3.1: Diabatic Processes

Diabatic processes involve the gain or loss of heat. Examples include phase changes (e.g. condensation warming the air and evaporation cooling it), radiative processes (absorption of radiation warms the air), or surface heat fluxes.

Infobox 3.2: Storm-Scale Ranges Used in This Document

"Small-scale" refer to motions smaller than 10 km, "mesoscale" for motions between 10-1000 km and "large-scale" for motions larger than 1000 km.

Fully capturing storm dynamics across scales, and their coupling with water and heat, requires a significant advancement in observations. On the modelling side, the need to resolve explicitly the air movement within storms, from the small to large scales, has been widely recognised. For example, European Centre for Medium-range Weather Forecasts (ECMWF) medium-range weather forecasts are run globally using an atmospheric model with a grid spacing of 9 km. Such models are often referred to as storm-resolving, as they can capture the full spectrum of storms that shape the weather.

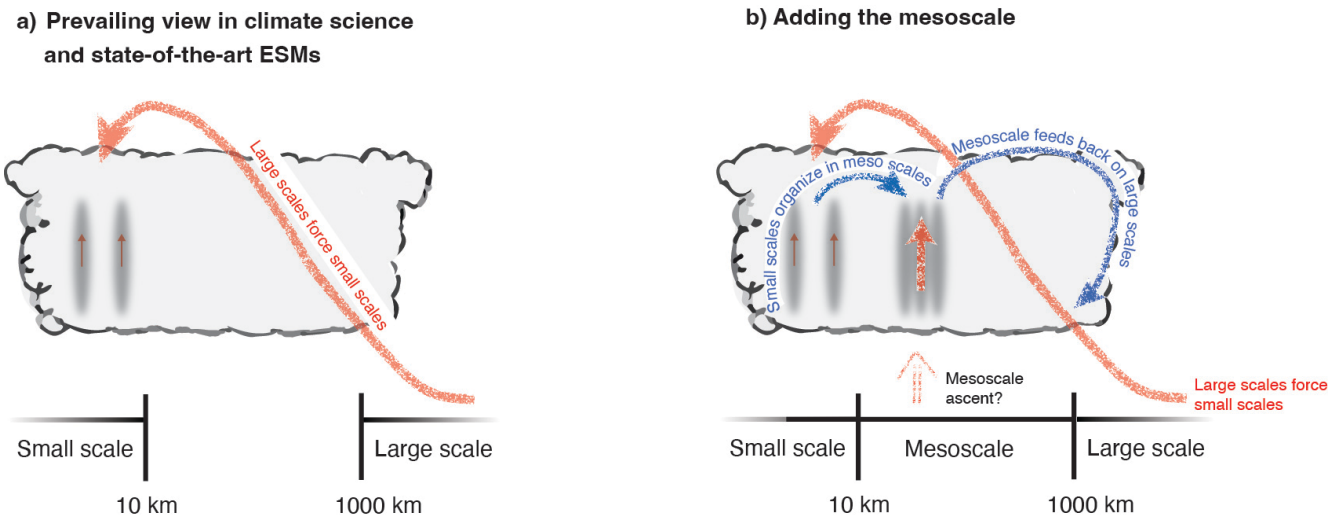

Figure 3: Simplified view of storms and their scale dependency with a) the traditional view in climate science, and b) the addition of the missing mesoscale component, highlighting how processes across scales are interconnected. A full understanding requires capturing interactions across the entire system.

Similarly, through ambitious programs such as Destination Earth (https://destination-earth.eu/), Europe is now at the forefront of developing and operationalising next-generation storm-resolving climate models (Hohenegger et al., 2023; Rackow et al., 2025; Segura et al., 2025). On the observational side, detailed measurements of storm dynamics across different scales and systems are currently lacking. Existing global observing systems mainly capture clear-sky conditions or cloud tops, leaving a significant gap in our knowledge of processes occurring within storm systems. These observations are essential, not only to deepen our understanding of storms, clouds, and precipitation, and their responses to climate change, but also to enhance storm-resolving models and improve forecasts of storms and related extreme events, such as atmospheric rivers.

The underpinning motivation of the WIVERN mission is to fill this critical gap. It will, for the first time, provide simultaneous global observations of in-cloud winds and condensed mass, from convective storms to large-scale extratropical stratiform systems. These new measurements will support three interconnected scientific objectives:

- **Understanding storms:** WIVERN will provide detailed information on how air and hydrometeors move within a wide range of storm systems across the globe, revealing the physical processes driving storm organisation, evolution, and intensity (Section 3.3).
- **Constraining cloud and precipitation impacts on climate:** By resolving vertical profiles of cloud and precipitation mass alongside wind, with a high spatial sampling, WIVERN will better constrain precipitation amounts and improve our understanding of how cloud morphology responds to climate change and feedbacks on the temperature response

(Section 3.4).

- **Improving Numerical Weather Prediction (NWP) and Earth System Models:** WIVERN will enhance weather forecasts through assimilation into NWP systems, and serve as a benchmark for next-generation storm-resolving Earth system models (Section 3.5).

WIVERN offers Europe a unique opportunity to lead this observational frontier, capturing the dynamics of storms where they matter most: inside the clouds, across scales, and around the globe.

Beyond these core objectives, WIVERN will also contribute to additional scientific advancements, including:

- Bridging Observational Gaps in Polar Sea Ice and Snow for Climate Research (Section 3.6.1)
- Revealing What Satellite Altimetry Misses: Advancing Our Understanding of Ocean Surface Current Dynamics (Section 3.6.2)

3.2. Status of the Global Wind Observing System

In-cloud winds are key to understanding cloud and storm processes and the coupling between water, heat, and atmospheric circulation, yet they remain one of the major gaps in the Global Observing System (GOS). This section provides a review of GOS for wind measurements, and shows that this critical component is significantly under-represented. An overview of the existing global wind observing system, alongside planned initiatives such as Aeolus-2 and the proposed WIVERN mission, is presented in Figure 4.

Atmospheric Motion Vectors (AMVs): AMV winds are normally derived by tracking atmospheric features such as clouds or water vapour using successive images from infrared and visible sensors. They offer near global coverage and high temporal resolution. However, their wind information is at a single vertical level, i.e. the height of the tracked feature. This height assignment carries considerable uncertainty (Salonen et al., 2015).

Aeolus: ESA's Aeolus mission (2018–2023) (Reitebuch, 2012) provided the first near globally distributed profiles of Horizontal Line of Sight (HLoS) winds from space using an off-nadir pointing Doppler wind lidar, and demonstrated one of the highest forecast impacts per satellite instrument (Rennie et al., 2021). Building on Aeolus success, ESA and EUMETSAT are now preparing the Aeolus-2 mission, planned for launch in 2034, (Marseille et al., 2023; Lean et al., 2023). However, like Aeolus, Aeolus-2 observations will be limited to clear skies, optically thin clouds and the tops of optically thick clouds with the lidar pointing at a fixed off-nadir angle, thus providing only a two-dimensional curtain of wind observations.

EarthCARE: ESA's EarthCARE (Earth Cloud, Aerosol and Radiation Explorer) mission, launched in 2024, carries a Cloud Profiling Radar (CPR) that provides Doppler radar measurements with

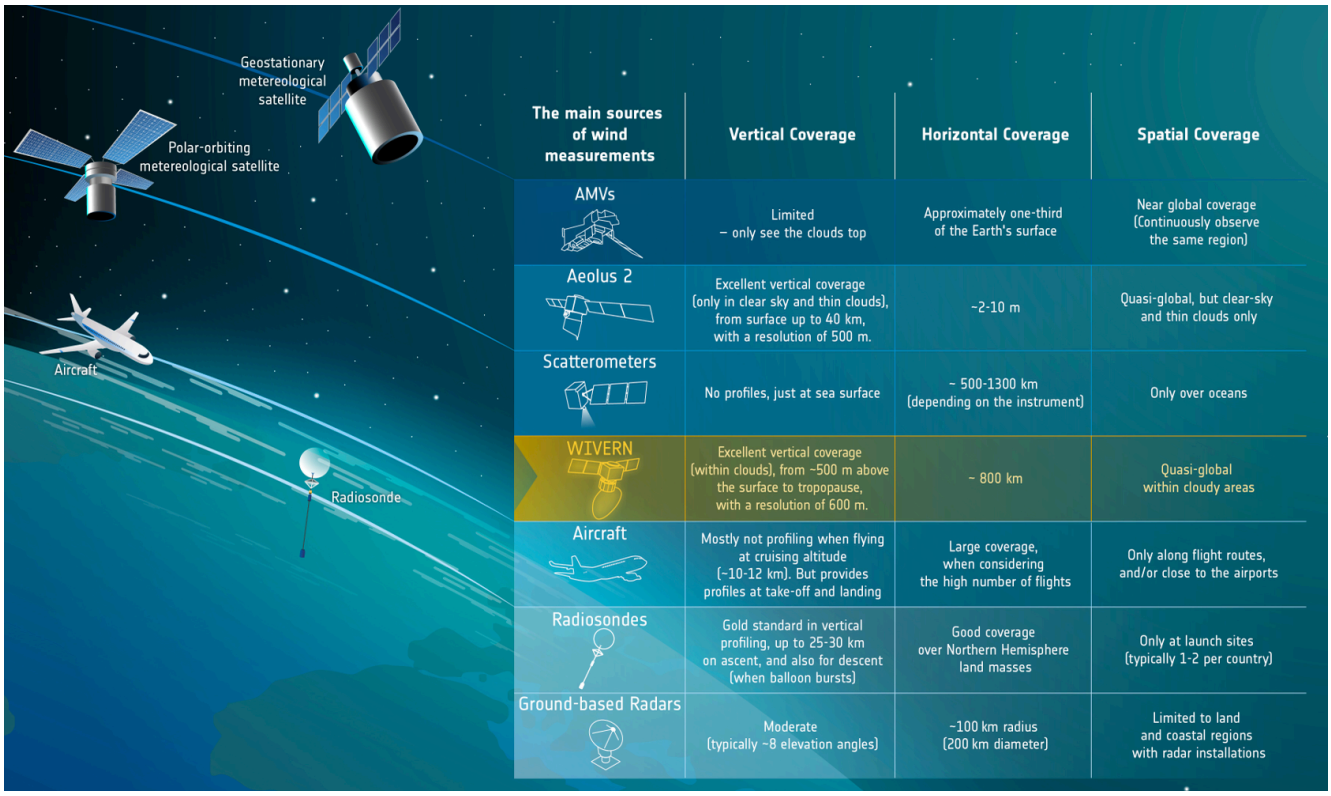

The main sources of wind measurements	Vertical Coverage	Horizontal Coverage	Spatial Coverage
AMVs	Limited – only see the clouds top	Approximately one-third of the Earth's surface	Near global coverage (Continuously observe the same region)
Aeolus 2	Excellent vertical coverage (only in clear sky and thin clouds), from surface up to 40 km, with a resolution of 500 m.	~2-10 m	Quasi-global, but clear-sky and thin clouds only
Scatterometers	No profiles, just at sea surface	~ 500-1300 km (depending on the instrument)	Only over oceans
WIVERN	Excellent vertical coverage (within clouds), from ~500 m above the surface to tropopause, with a resolution of 600 m.	~ 800 km	Quasi-global within cloudy areas
Aircraft	Mostly not profiling when flying at cruising altitude (~10-12 km). But provides profiles at take-off and landing	Large coverage, when considering the high number of flights	Only along flight routes, and/or close to the airports
Radiosondes	Gold standard in vertical profiling, up to 25-30 km on ascent, and also for descent (when balloon bursts)	Good coverage over Northern Hemisphere land masses	Only at launch sites (typically 1-2 per country)
Ground-based Radars	Moderate (typically ~8 elevation angles)	~100 km radius (200 km diameter)	Limited to land and coastal regions with radar installations

Figure 4: A summary of the status of the global wind observing system.

high sensitivity and sub-kilometre horizontal resolution, but only along a narrow <1 km wide vertical curtain. While it can occasionally sample vertical velocities within convective updrafts, this is not sufficient to reconstruct the mesoscale circulation associated with storms or to accurately quantify the strength of the more intense vertical motions. Horizontal winds cannot be observed.

Satellite Active and Passive Microwave Observations: They offer surface wind vector observations over oceans with dense global horizontal coverage. The scatterometric surface winds are complemented by finely resolved Synthethic Aperture Radars (SARs), and radiometry-based passive microwave observations. Measurements from Global Navigation Satellite System (GNSS) reflectometry are also being tested through proof-of-concept missions, such as NASA's CYclone GNSS (CYGNSS) and ESA's HydroGNSS. Vertically-resolved wind profiles cannot be derived.

Airborne Systems: Commercial aircraft contribute a large number of horizontal wind vector observations. They provide high-resolution profiles near airports during take-off and landing; otherwise observations are restricted to specific cruising altitudes and flight path. Moreover, for safety reasons, aircraft typically avoid flying through storms.

Radiosondes: These balloon-borne instruments provide high-accuracy vertical profiles of wind, from fixed ground stations. They offer wind measurements throughout the depth of the tropo-

sphere and into the lower stratosphere. However, their spatial coverage is sparse, particularly over oceans and in the tropics, and their temporal resolution is limited to only twice a day.

Operational Networks of Ground-based Radars: They provide observations with very high temporal resolution, on the order of a few minutes. Their operation requires precipitation to detect wind, and non-precipitating clouds are generally below their detectability threshold. The vertical resolution is coarse and the coverage is limited to land and coastal areas.

Another important consideration for wind observations is how the wind is measured. Missions such as Aeolus and WIVERN provide near-direct wind measurements through their Doppler capability. Similarly, winds derived from radiosondes and aircraft can be considered close to direct measurements. In contrast, scatterometers, radiometers, as well as Geostationary (GEO) and Low Earth Orbit (LEO) imagers infer wind indirectly, either from the effect of wind on ocean surface roughness, or from the apparent motion of cloud features, which can introduce significant uncertainty due to confounding factors.

As demonstrated, wind observations are sparse and unevenly distributed, especially in cloudy regions, on the mesoscale, and in the vertical dimension. Given the importance of wind observations, the following two specific recommendations were made to Space Agencies at the 7th World Meteorological Organisation (WMO) workshop on “The impact of Various Observing Systems on NWP” (WMO, 2020):

Recommendations made by WMO to Space Agencies

- Space Agencies are encouraged to continue pursuing wind profile measurements from space.
- Effort is encouraged to assess complementary/synergies between different wind measurement systems/technologies (e.g. Aeolus and Atmospheric Motion Vectors).

Building on these recommendations and addressing the critical gap in global observations of three-dimensional (3D) in-cloud winds, the following sections highlight the importance of in-cloud wind data and their direct contribution to tackling key scientific challenges.

3.3. Understanding Storms

Earth is stormy. This becomes most apparent when viewed from space, where the numerous clouds generated by storm systems are clearly visible across the globe (see Figure 1). Storms are classified into different types depending on their formation mechanism, regions of occurrence, and horizontal extent. In the tropics, and during summer, convective instability (Infobox 3.3) is the dominant formation mechanism. Convective instability gives rise to individual convective cells (thunderstorms), which can then organise into larger storm systems such as squall lines (a linearly organised cluster of convective cells), MCSs (clusters of convective cells spanning over 100 km), or TCs. While the motion within individual convective cells is mostly

vertical, the organisation into convective systems generates horizontal mesoscale circulations that influence the broader atmospheric circulation. Vertical wind-shear also play an important role in the organisation and lifetime of convective storms.

Infobox 3.3: Convective Instability

Convective instability refers to a state in the atmosphere where the vertical distribution of temperature and moisture allows air parcels to rise freely through the atmosphere, until they have lost their buoyancy. This upward motion, known as convection, is a key driver in the formation of thunderstorms and deep convective cloud systems.

In the mid-latitudes, lines of equal temperatures and pressure are not parallel (which is called baroclinicity, Infobox 3.4), creating a three-dimensional circulation. This leads to formation of fronts and extratropical cyclones, as well as atmospheric rivers, known for their extreme water transport. Convective cells can also be embedded in these systems. Additionally, polar lows are intense mesoscale maritime cyclones that occur in polar to sub-polar regions (Renfrew, 2003). They typically develop within or along the edge of marine cold-air outbreaks, where cold, dry air masses, originating from continental regions or sea ice, flow over the relatively warmer open ocean (Terpstra et al., 2021).

Infobox 3.4: Baroclinic Processes

Baroclinic processes occur when surfaces of constant pressure and temperature are not aligned, which leads to the generation of vorticity, a measure of how much the air is spinning or rotating. This mechanism is fundamental to the development of large-scale weather systems such as extratropical cyclones.

Despite different names, all storms share common features: each storm is embedded within, and interacts with a larger-scale environment; air moves both horizontally and vertically within them; and water changes phases depending on the temperature and specific humidity of the air (Figure 3). These phase changes heat or cool the atmosphere locally, driving further air motion.

Gaining knowledge on how storms work is of utmost importance for understanding the evolution of several types of high-impact weather events, with the associated repercussions to forecasts and predictability (Rodwell et al., 2013). It is also key to understand the climate impacts of storms (Section 3.4) and project how storms will change under global warming. WIVERN is uniquely suited to address two storm-related research topics: **1) better characterise and understand the internal dynamical storm structure**, and **2) untangle the complex interplay between water, heat, and circulation**, both within storms and in their interactions with the broader-scale environment.

3.3.1. Storm Structure and Dynamics

Figure 5 shows our understanding of different storm archetypes in forms of conceptual models, as derived from theoretical studies, numerical simulations, and localised observational campaigns. Scientific questions relating to storm structure fall into two main categories: a) improving these conceptual models, and b) evaluating how well they apply, or need to be adapted, to capture the full diversity of storm types across different Earth's climates. For instance, in the relatively simple geometry of an intense squall line (a linearly organised cluster of convective cells - see Figure 5b), two contrasting views exist regarding the depth of the wind shear layer: one suggests it is restricted to the boundary layer, while the other assumes it extends deep into the troposphere. The first case suggests that storm morphology is controlled by a physical process, specifically, entrainment within convective cores (Mulholland et al., 2021). The second case suggests that a dynamical feature, namely a mid-tropospheric overturning circulation, as identified in simulations, control the extend of the storm system (Coniglio et al., 2006). Observing the wind profile within many squall lines and the frequency of occurrence of a mid-level circulation would help favor one over the other argument.

Likewise, there is uncertainty in how the secondary circulation of a mature TC is described. The general view of several foundational studies is that it consists of a boundary layer inflow, which first rises in the deep convective towers of the eyewall, and then turns outward to form the cirrus outflow cloud shield just below the tropopause (Houze, 2010). In this widely accepted view, updrafts within the outer rainbands are not considered to contribute to the primary outflow (see Figure 5c). However, novel model simulations by Nolan et al. (2025), based on an examination of the mass and moisture budgets of the cirrus outflow shield present a different view: on average, around 50% of the dry air mass flux, and an even larger fraction of the condensate in the outflow, is supplied by deep convection in the surrounding rainbands. This highlights the importance of the rainband convection in determining the size and thickness of the outflow cloud shield, which influences storm intensity and its intensification processes (Wu and Soden, 2017).

The wind field structure is also essential for the growth of extratropical cyclones, especially the vertical wind shear along the tropopause (Birner et al., 2006; Schäfler et al., 2020). However, the role of tropopause sharpness[1] in modulating baroclinic development (Infobox 3.4) is still not fully understood (Haualand and Spengler, 2021). Its representation in model analyses, and its broader influence on extratropical cyclones dynamics and development is uncertain.

For polar lows, there is even a lack of a universally accepted conceptual model (Moreno-Ibáñez

[1] Tropopause sharpness refers to how suddenly temperature and wind change at the boundary between the troposphere and stratosphere

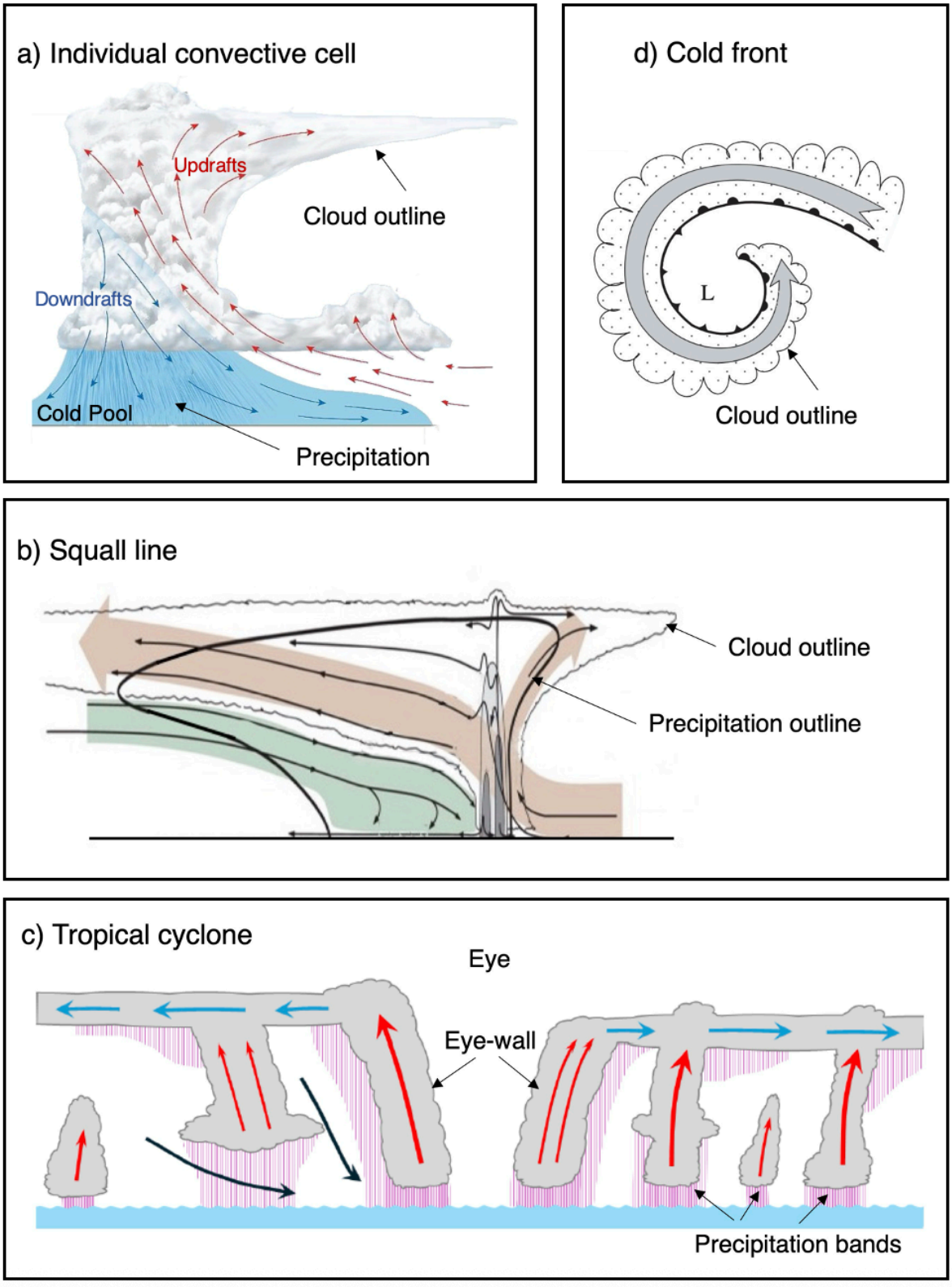

Figure 5: Conceptual models of various storms, as derived from dedicated field campaigns and model studies. The conceptual models retain the key features of storms, namely the cloud, the precipitation, and the air motion within the storms. Panel a): Individual convective cell, from Eby (2010); b): Squall line, from Zhang (2022); c): TC, from Nolan et al. (2025); and d): Cold front associated with an extratropical cyclone, from Schultz and Browning (2017).

et al., 2021). This reflects the wide range of proposed formation mechanisms, which span from dry and moist baroclinic instability (Infobox 3.4) concepts to hurricane-like intensification driven by strong surface fluxes. In contrast, recent studies emphasise the importance of diabatic processes (Infobox 3.1) and wind shear (Stoll et al., 2022), particularly those related to latent heat release and precipitation (Terpstra et al., 2015), during the early development phase, aligning polar lows more closely with extratropical cyclones.

Our limited knowledge of storm structure, and the ongoing debates over their underlying mechanisms, reflect the shortage of observations and the difficulty of representing storms in traditional atmospheric models. Coarse-resolution models are unable to simulate squall lines, TCs, or polar lows. Models also face challenges in accurately representing the magnitude and distribution of diabatic processes during cyclone development (Schäfler et al., 2018; Wernli and Gray, 2024). This contributes to errors in forecast, particularly for high-impact weather events (Rodwell et al., 2013, 2018). Although storm-resolving models can capture the various storm types, deficiencies remain, as discussed in Section 3.5.

Advances in our understanding of storm structure is also essential to better characterise storm propagation. Understanding the factors that control propagation of storms is important, as slowly moving or stationary cloud systems can cause severe flooding, as they bring continuous precipitation to a region. Although basic theories on storm propagation exist, the lack of global observations of internal storm dynamics hinders a thorough understanding of how storms propagate, and how their speed varies across different Earth's climates. For example, it is unclear whether TCs will propagate faster or slower as the climate warms (Kossin, 2018).

At present, the dynamical structure of storms can only be observed through localised field campaigns, which limits the ability to generalise findings. While space-borne observations could provide the necessary sampling, current observing capabilities are largely restricted to measuring precipitation and hydrometeors distribution. They do not provide information on the in-cloud horizontal wind field or internal storm circulation and its variability, specifically the horizontal and vertical wind shear.

The key scientific question related to "Storm Structure and Dynamic" is: **What is the role of internal storm dynamics, including horizontal and vertical wind shear, in governing the development, intensification, and propagation of different storm types across spatial and temporal scales?**

3.3.2. Water, Heat and Circulation

The laws of energy and mass conservation tightly link water, heat (thermodynamics), and circulation (dynamics), as shown in Fig. 6a. Within a storm, changes in the phase of water and the absorption or emission of radiation release or consume energy. The resulting diabatic heating (see Infobox 3.1) drives air motion. This mechanism is relevant to both tropical and extratrop-

ical storms. The circulation induced by diabatic heating is superimposed on any pre-existing background flow. The central challenge, therefore, is to understand how water, heat, and circulation interact on smaller scales within the storm, and how these processes contribute to and interact with the broader mesoscale and large-scale circulations.

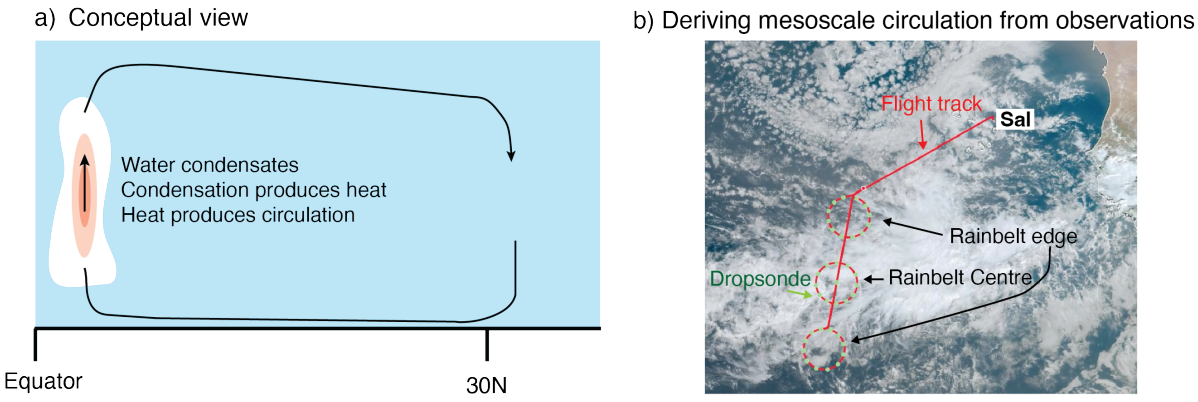

Figure 6: Panel a) Conceptual illustration of one form of coupling between water, heat, and circulation; and b) measurement of mesoscale circulation strength at the edges and centre of the tropical Atlantic rainbelts, using dropsondes released in a circular pattern from an aircraft during the ORCESTRA field campaign.

Considering the coupling between water, heat, and circulation at small scales within storms, uncertainty in the representation of microphysical processes, such as the formation of ice particles, translates directly into dynamical uncertainty in model simulations. For instance, Fan et al. (2017) studied an intense mid-latitude MCS and showed how sensitive various storm attributes (e.g. intensity and structure) are to the microphysical assumptions that drive the diabatic heating.

Some of these attributes, at the small-scale (1 km), directly reflect the water-heat-circulation coupling driven by the conservation of energy and mass, and lead to uncertainties in the estimation of both surface precipitation and vertical velocity. Vertical velocity profiles can differ by up to 30% between microphysical schemes, with the largest discrepancies found above 8 km altitude, within the ice-phase region of storms, and with downdrafts often under-represented (Varble et al., 2020). These sensitivities are evident not only in mid-latitude storms but also in deep tropical convection (Varble et al., 2011). Uncertainty in storm dynamics, coupled with uncertainty in both ice and warm precipitation processes, has direct implications for surface precipitation estimates.

Moreover, the true dynamical nature of the storm further amplifies this sensitivity, especially

in relation to mesoscale structural characteristics such as the underlying cold pool[2] with up to ∼30% uncertainty in its strength (Fan et al., 2017). These uncertainties can ultimately hinder a full understanding of the storm's lifecycle. In other words, small-scale processes grow upscale through the coupling between water, heat and circulation.

An alternative perspective places greater emphasis on mesoscale processes and the circulation within the core of the storm, rather than on small-scale features. In this view, MCSs are embedded within a broader region of mesoscale ascent, which plays a key role in supporting their development and maintenance (Houze, 2004; Galarneau et al., 2023). Testing this perspective requires measurements of horizontal winds across the mesoscale area occupied by a storm, an objective that demands observations capable of capturing the three-dimensional wind field at the mesoscale.

As further discussed in Section 3.1 and shown in Figure 3, the mesoscale connects the small- and the large-scale motions. Despite the clear visibility of mesoscale features in satellite imagery (Figure 1), current theories explaining the large-scale climatological characteristics of rainbelts, such as their position and width, only rely on large-scale arguments (Bischoff and Schneider, 2016; Byrne and Schneider, 2016). There is renewed interest in understanding the internal mesoscale dynamics of the marine rainbelts, with key questions emerging, such as whether low-level convergence[3] tends to occur at the centre of these belts or along their flanks (Windmiller and Stevens, 2024).

Satellite missions like Tropical Rainfall Measuring Mission (TRMM) and Global Precipitation Measuring mission (GPM) have provided global observations of vertical profiles of diabatic heating (Tao et al., 2016), but not of the associated circulations, limiting our ability to achieve a comprehensive understanding of the water-heat-circulation coupling across the diversity of storm types and spatial scales. Field campaigns have demonstrated the importance of measuring internal storm characteristics, associated diabatic heating profiles, and the larger-scale circulation, by combining ground-based and airborne measurements (e.g. Figure 6 b). The larger-scale circulation is obtained by deploying arrays of soundings over extended areas, enabling estimates of mean mass convergence and divergence (Yanai et al., 1973; Bony and Stevens, 2019). However, such campaigns are limited in space and time. These limitations underscore the need for a space-borne sensor capable of observing internal storm structures with broad coverage, such as WIVERN, offering the determination of mean mesoscale convergence and divergence.

[2]Cold pool refers to the cool, dense air mass that spreads beneath the storm due to precipitation (see Figure 5a).
[3]Low-level convergence refers to horizontal inflow of air near the Earth's surface, where air from different directions converges.

The EUREC[4]A field campaign (Stevens et al., 2021) employed airplanes flying in circles of 200 km diameter over fields of shallow cumulus to determine the mesoscale mass convergence. The results showed that contrary to common understanding, cloud fraction is more strongly linked to convergence than to humidity (Vogel et al., 2022). A similar approach has been applied to deep convection (Figure 6b), as demonstrated by the recent ORCESTRA field campaign (https://orcestra-campaign.org/). While retrieving vertical velocity in shallow convection environments may be challenging for WIVERN (since the vertical velocities in shallow convection are usually too weak to be detected by WIVERN), the mission will be capable of observing vertical motions in deep convection. WIVERN will also regularly sample congestus cloud fields[4] Although they produce precipitation, their role in the tropical climate system remains uncertain. One hypothesis is that congestus clouds pre-moisten the atmosphere, helping the development of deep convection and the organisation of large-scale convective systems such as the Madden-Julian Oscillation (MJO) (Waite and Khouider, 2010; Ruppert and Johnson, 2015), though this has been challenged by others (Hohenegger and Stevens, 2013; Jiang et al., 2020). Another hypothesis is that fields of congestus clouds generate mesoscale circulations, which promote the development and organisation of deep convection.

In the extra-tropics, likewise, our understanding of the intensification of extratropical cyclones and the factors that determine their tracks remains limited, largely due to the difficulty of disentangling the complex coupling between water, heat, and circulation. For example, Coronel et al. (2015) showed that incorporating water processes into idealised model simulations leads to a more intense surface cyclone and faster storm propagation. This acceleration happens because of the interaction between the spinning winds near the surface ahead of the storm and the opposite spinning winds higher up in the atmosphere.

Similarly, Tamarin-Brodsky and Kaspi (2017) proposed another explanation for the anticipated poleward shift of storm tracks in a warming climate. They highlighted changes in storm propagation linked to stronger upper-level winds and enhanced latent heating from microphysical processes. However, the representation of these moist microphysical processes in current atmospheric models remains highly uncertain (Wandel et al., 2021; Heitmann et al., 2024).

Observing wind profiles and hydrometeor content at the scale of individual storms would offer a critical opportunity to test such model-based hypotheses regarding storm lifecycles and their sensitivity to warming. This is particularly relevant for features such as atmospheric rivers and warm conveyor belts, where much of the latent heat release takes place. Atmospheric rivers, which typically form ahead of a cyclone's cold front (see Figure 5d), are often associated with

[4]Congestus clouds typically reach heights of around 8 km, do not contain ice particles, and form the third major cloud population in the tropics, after shallow and deep convection (Johnson et al., 1999).

intense rainfall upon landfall (Ralph et al., 2011).

The key scientific question related to “Water, Heat and Circulation” is: **What is the relationship between water, heat, and circulation at the storm scale? How strong is the feedback from storms onto the mesoscale, and how do mesoscale circulations influence the development of larger-scale dynamics?**

WIVERN Contribution to Goal 1 - Understanding Storms

Achieving a global understanding of storm structure, dynamics, and their coupling with water and heat requires continuous observations across different regions and seasons. This is only feasible with a polar-orbiting satellite capable of providing detailed, wide-swath measurements of winds and hydrometeors. A Doppler radar operating at high frequency is essential to detect clouds and resolve cloud processes bridging between the mesoscale and the large scale. WIVERN is uniquely designed to meet these requirements, offering unparallel sampling, global coverage, and the ability to observe the vertical structure of even hurricane-force winds within clouds.

3.4. Constraining Cloud and Precipitation Impacts on Climate

Clouds and precipitation systems are linked to planetary-scale overturning circulations. Figure 7 provides a schematic illustration of Earth’s principal cloud regimes and, crucially, their connection to the atmosphere’s overturning circulation. These links begin with regions of deep convection in the tropics, which gives rise to high-level clouds, while low-level clouds form beneath the descending branches of the same overturning circulation, which is partly driven by the convection itself. In addition, deep convection plays a fundamental role in Earth’s heat engine, transferring energy from the tropics to mid-latitudes. From there, extratropical cyclones carry this energy further towards the poles, while bringing clouds and precipitation to the mid-latitudes and polar regions.

Three cloud and precipitation systems where WIVERN observations are expected to offer significant advances over current and planned satellite missions are: **convective anvil clouds**, **shallow oceanic clouds**, and **polar snowfall**. The first two are critical for cloud–radiation feedbacks (InfoBox 3.5), while polar snowfall plays a central role in high-latitude water budgets and interactions between the atmosphere and cryosphere. A satellite perspective on these features is illustrated in Figure 8.

For anvil clouds produced by deep convection in the tropics, a key question is how their vertical and horizontal extent relates to the parent convection and what controls their development. For shallow oceanic clouds, the main question concerns their mesoscale organisation, as seen in the horizontal variability captured by satellite imagery. This organisation is evident in both stratocumulus and cumulus cloud regimes. In polar lows and cold-air outbreaks, there remains both a need to understand the mechanisms behind the observed cloud organisation and to

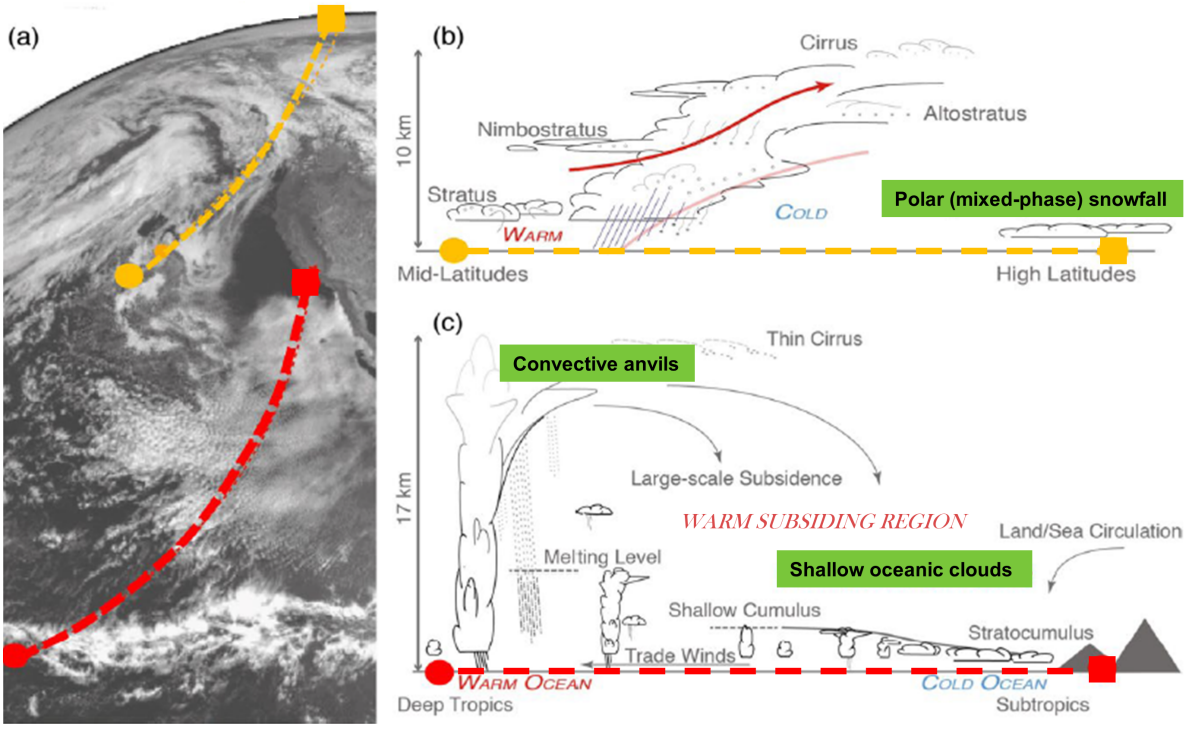

Figure 7: Panel (a): Visible imagery from a geostationary satellite. Panel (b): Schematic cross-section along the orange dashed line highlighted in (a), showing a typical warm front of an extratropical cyclone, with associated cloud types, from the mid- to high latitudes. Panel (c): Schematic cross-section along the red dashed line in (a), indicating the Hadley cell from deep convection in the low-latitudes to stratocumulus in the subtropics. Adapted from Stephens et al. (2024).

improve quantitative estimates of associated snowfall.

Infobox 3.5: Cloud Feedback and Its Climate Impact

Cloud feedback refers to the change in the Earth's radiation budget caused by changes in cloud properties (e.g. amount, height, thickness, type) as the planet warms. If clouds reflect more sunlight or trap more infrared radiation in response to warming, they can either dampen (negative feedback) or amplify (positive feedback) the temperature rise. The feedback is typically expressed in watts per square meter per kelvin ($W\,m^{-2}\,K^{-1}$).

Simply measuring precipitation amounts or cloud radiative properties is not, on its own, sufficient to predict future changes. A physical understanding of the underlying processes is essential. The aspects of climate change, in which the highest confidence exists, are those supported by robust physical explanations. Therefore, improving our understanding of storms (Section 3.3), clouds, and precipitation is strongly linked to enhancing our ability to assess and project their climatic impacts.

The subsequent sections explore the three systems mentioned above in more detail, and indi-

cate how WIVERN observations can provide a step change in advancing our understanding of them.

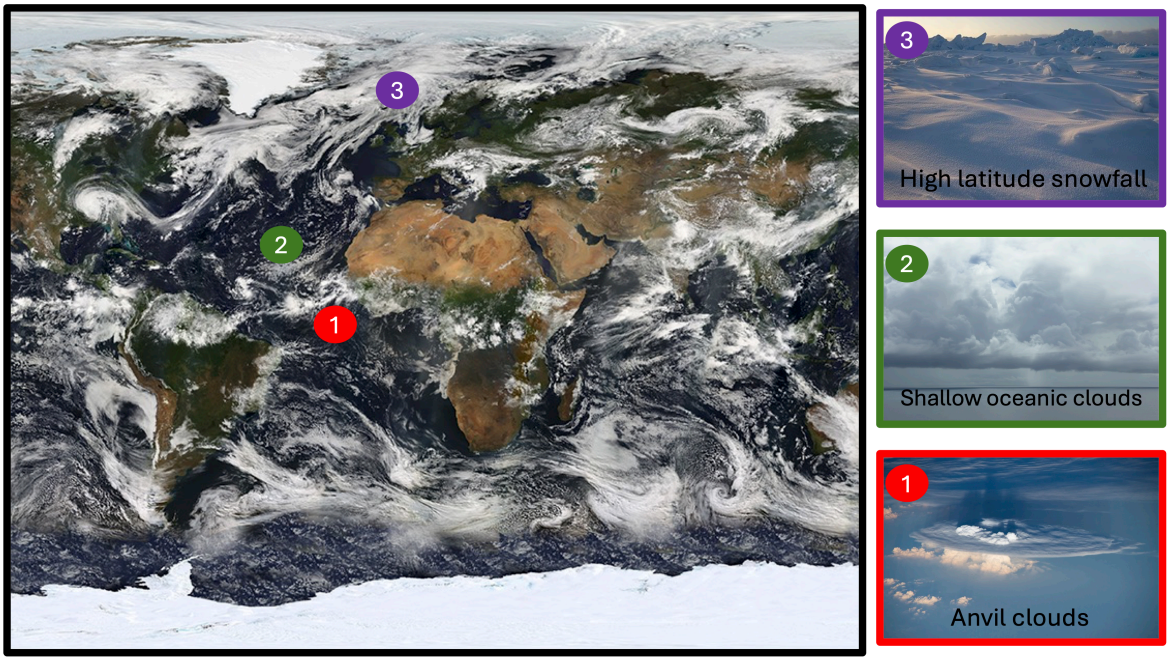

Figure 8: A satellite view of global cloud coverage, highlighting 1) anvil clouds, 2) shallow oceanic clouds, and 3) high-latitude (polar) snowfall.

3.4.1. Anvil Cloud Feedback

Anvils are cirrus clouds that form at the top of thunderstorms, where rising air parcels in the convective tower lose their buoyancy and spread out horizontally into the surrounding environment (Figure 9). Lindzen et al. (2001) first proposed that as the climate warms, the area of anvil clouds decreases, allowing more longwave radiation to escape into space and acting as a strong negative feedback against warming. However, their methodology, which relied on geostationary satellite observations, has been criticised first by Hartmann and Michelsen (2002) and many subsequent studies for using data that may not be representative of global anvil cloud behaviour and for oversimplifying cloud processes.

Sherwood et al. (2020) combined multiple lines of evidence and estimated that the feedback associated with a change in anvil cloud area, the so-called anvil cloud area feedback, is $-0.2 \pm 0.2\,\mathrm{W\,m^{-2}\,K}$ More recently, McKim et al. (2024) revised this estimate to $0.02 \pm 0.07\,\mathrm{W\,m^{-2}\,K^{-1}}$. If true, such a reduction of the anvil cloud area feedback by $0.2\,\mathrm{W\,m^{-2}}$ would correspond to an additional 0.6 K warming under a doubling of CO_2. This adjustment is noteworthy, as it highlights how relatively small changes in cloud feedbacks can lead to substantial differences in projected global warming.

Despite decades of research since Lindzen et al. (2001), accurately quantifying the anvil cloud

area feedback remains challenging due to the limited length of the observational record. While climate models can offer longer-term perspectives, they rely on parametrisation (see Infobox 3.6) of the processes involved in cloud formation, making their estimates also uncertain given biases associated with the representation of convection (see Section 3.5).

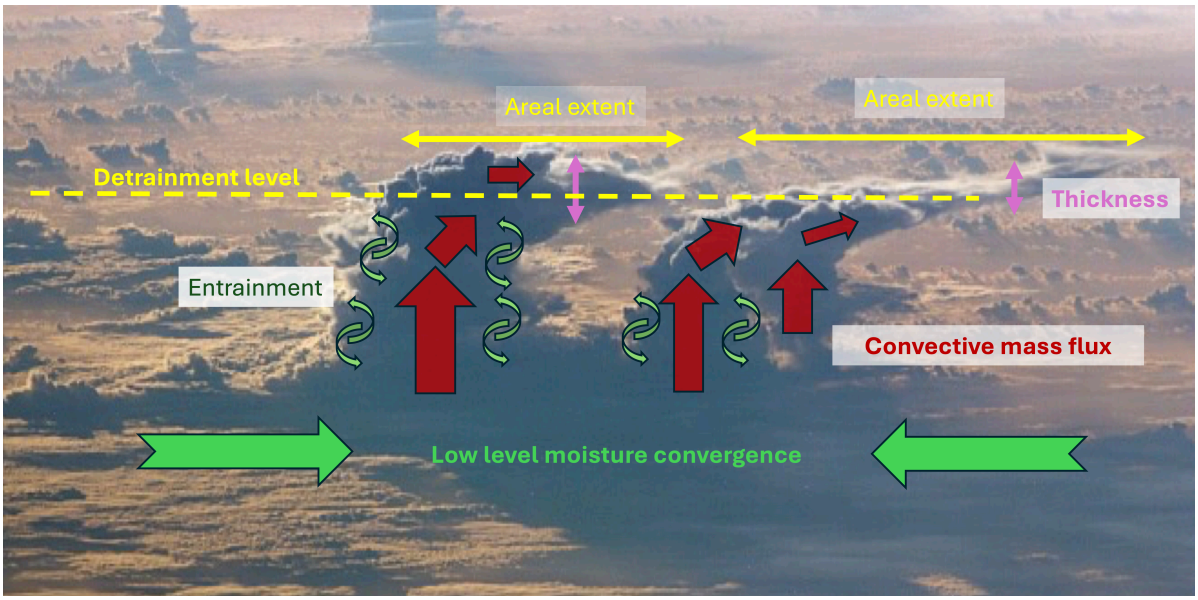

Figure 9: Schematic illustrating the relationship between convective mass flux, upper-level detrainment, and anvil cloud properties (area and thickness). The parent convection is initiated by low-level moisture convergence and atmospheric instability. The convective cores are characterised by the vertical transport of heat and condensate via strong updraughts, and they interact with the surrounding near-storm environment through entrainment and mixing processes. Near the level of neutral buoyancy, the uplifted condensate detrains into the environment, giving rise to extensive convective anvils (child clouds).

More fundamentally, the uncertainty in estimates of the anvil cloud area feedback reflects our poor physical understanding of the processes that control anvil area. One hypothesis is that anvil cloud area is determined by the mass detrained from thunderstorms into the surrounding environment (Bony et al., 2016). Another idea, based on km-scale idealised simulations of anvil evolution, suggests that anvil area is controlled by a combination of cloud radiative process and latent heating, which together shape a double-cell circulation (Gasparini et al., 2019). A further idea emerging from such simulations is that tropical anvil clouds are rather formed by the long lifetime of upper-tropospheric condensates due to slow evaporation rates rather than by mass detrainment (Seeley et al., 2019). Falsifying one or the other of these competing hypotheses requires horizontal wind measurements within anvil clouds and observations of mass detrainment, both of which do not currently exist. These observations will be uniquely provided by WIVERN. As shown in recent assessments (Sherwood et al., 2020; McKim et al., 2024), reducing the uncertainty in cloud feedbacks requires a storyline approach, one that integrates multiple lines of evidence, including direct observations and physical understanding.

The other uncertain feedback related to anvil clouds is their potential change in albedo as the climate warms. A key challenge in understanding albedo changes lies in determining whether anvil clouds will thicken (producing a negative feedback by reflecting more short-wave radiation) or thin (leading to a positive feedback due to increased long-wave radiation absorption) as the climate warms. This, in turn, depends on the fundamental processes governing anvil cloud lifecycles. Previous observational studies have reported both an increase (McKim et al., 2024) and a decrease (Kubar and Waliser, 2019) in cloud albedo with warming. To resolve this uncertainty, systematic observations of anvil detrainment height, mass, thickness, and air movement, as a function of distance from convection, are needed across a diverse range of convective systems.

The key scientific question related to "Anvil Cloud Feedback" is: **What is the relationship between convective mass flux and the extent and depth of anvil clouds in tropical storms, and which mechanism mainly controls their fate?**

3.4.2. Shallow Oceanic Clouds

Shallow clouds cover vast areas of the ocean and contribute to cooling the planet. However, due to their small scale, climate models struggle to represent them accurately, resulting in significant uncertainty in climate projections (Bony et al., 2020; Kazil et al., 2024). Model predictions vary widely, from scenarios in which shallow cumuli largely vanish, amplifying surface warming, to projections indicating minimal change.

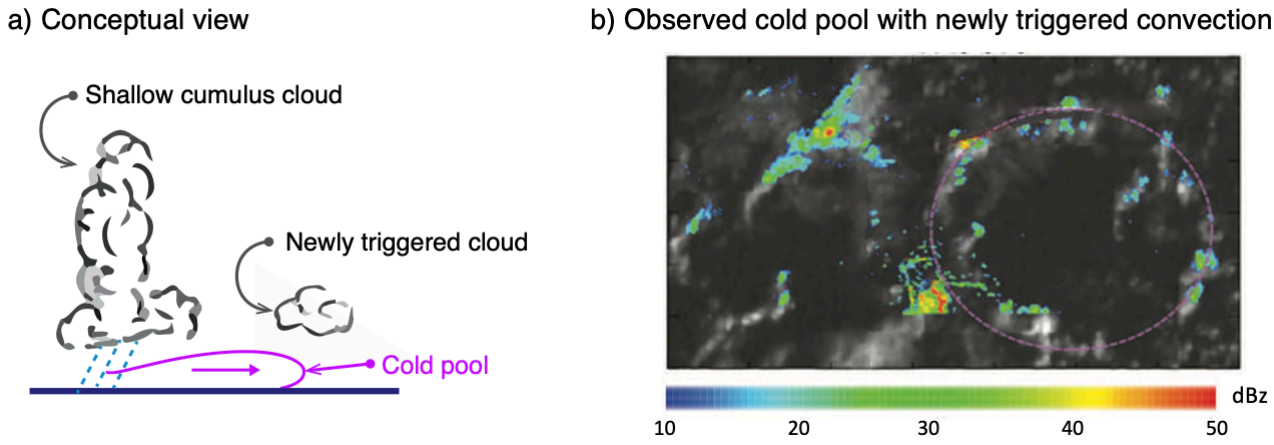

Figure 10: (a) The evaporation of precipitation below a parent convective cell leads to the formation of a cold pool that triggers new convective cells at its edge, thus organizing the convection field (conceptual view); (b) observed cold pool (fuchsia outline) with its ring of newly triggered convective cells. Panel (b) shows GOES-12 visible image (1145 UTC, 11 January) overlaid with S-Pol radar reflectivities (adapted from Zuidema et al. (2012)). The parent cell has already dissipated in (b).

Although it has long been recognised that shallow oceanic clouds frequently organise on the

mesoscale in diverse patterns (Stevens et al., 2019), the role this organisation may play in cloud feedbacks remains under-explored (Nuijens and Siebesma, 2019; Vial et al., 2017). Bony et al. (2020) first showed that different cloud mesoscale patterns have distinct impacts on the radiation budget, opening a new avenue for investigating low-level cloud feedbacks and improving climate change projections through the study of cloud organisation. More recently, satellite observations by McCoy et al. (2023) suggest that climate change is likely to increase net positive cloud feedback by enhancing mesoscale cellular organisation in boundary layer clouds (see InfoBox 3.5).

Given this renewed interest in low-level shallow cloud organisation, the question *"what controls mesoscale organisation"* has been defined as one of the three questions addressed by the Global Atmospheric System Studies panel, one of the core projects of the Global Energy and Water Exchanges (GEWEX) program of the World Climate Research Program.

A key factor influencing the organisation of shallow clouds is the evaporation of precipitation below the cloud base (Zuidema et al., 2017). This process generates dense surface outflows, or "cold pools" (see Figure 10), whose edges often become favourable locations for new convective cell formation. These outflows are sometimes visible in geostationary satellite imagery as arcs radiating from the parent convective cells. While Figure 10 illustrates this process for shallow cumuli, precipitation also plays a key role in stratocumulus clouds. It breaks up the closed cloud deck, reorganising it into mesoscale pockets of open cells, which strongly influences their albedo and the radiation budget (Stevens et al., 2005).

Geostationary satellites provide high spatio-temporal resolution imagery, enabling detailed observation of the organisation and morphology of low-level cloud fields over the oceans (Bony et al., 2020). However, their reliance on visible and infrared sensors restricts them to observing only cloud tops. Existing scanning space-borne radar systems, such as TRMM and GPM, lack the sensitivity and resolution necessary to detect precipitation associated with these precipitating clouds, while microwave imagers are similarly constrained by their limited resolution, which is too coarse to resolve the broken nature of these cloud fields. Instruments such as the Cloud Profiling Radar (CPR) on CloudSat and EarthCARE, along with their synergistic observations, can offer valuable information on total water path and precipitation rates within these clouds. Nevertheless, the typically low fractional cloud coverage of these cloud systems hampers the ability of these missions to gather statistically significant datasets across specific sea surface temperature and water vapour regimes.

In addition, observations of Cloud Water Path (CWP) are essential for understanding the influence of cloud microphysics and aerosols on precipitation formation. Passive microwave measurements of total Liquid Water Path (LWP) are particularly useful in this context, but they are subject to uncertainties due to biases in cloud fraction estimates and the challenge of distinguishing between cloud and rainwater contributions (Greenwald et al., 2018). While the combined use of passive microwave, visible–infrared, and active radar observations has improved

retrieval accuracy (Elsaesser et al., 2017), microwave emission signals from cloud water often are superimposed with those from precipitation-sized hydrometeors. This overlap increases the uncertainty of LWP estimates, especially in areas experiencing significant rainfall.

The key scientific question related to “Shallow Clouds” is: **How frequently and how strong do oceanic shallow clouds precipitate and what is the relationship between precipitation, organisation and shallow cloud feedbacks?**

3.4.3. Polar Snowfall

In mid-latitudes, most precipitation is formed through the ice phase as snowfall (Mülmenstädt et al., 2015), while in high latitudes and mountainous regions, it is the dominant form of precipitation at the ground (Field and Heymsfield, 2015). Snowfall not only removes moisture from the atmosphere but also plays a crucial interlinking role in the climate system. In the cryosphere, snowfall is the only mass source term for glaciers and ice sheets (Souverijns et al., 2018a; Davison et al., 2023; Bailey and Hubbard, 2025). Because the largest uncertainty in projections of future sea level rise is rooted in knowledge gaps in the mass balance of the ice sheets of Greenland and Antarctica, regional and seasonal precipitation measurements in these locations are particularly important. On sea ice, snow forms an insulating layer between the sea ice and atmosphere, influencing sea ice longevity (Perovich et al., 2017). On land, snow modifies the surface albedo, which is particularly relevant for the ice-albedo feedback mechanism, which amplifies surface warming (Hall, 2004). Additionally, snow cover has broader socio-economic and environmental impacts, such as influencing ecology (Slatyer et al., 2022), traffic safety (Strong et al., 2010), recreation (Steiger et al., 2019), and freshwater storage, which is also important for hydropower generation (Wasti et al., 2022). In a warming climate, precipitation amounts, including extreme snowfall events, are expected to increase (Quante et al., 2021). However, the exact magnitudes of these changes are associated with large uncertainties (Lopez-Cantu et al., 2020; Fiddes et al., 2022), stemming from our limited understanding of the complex interactions between ice particles, liquid water, cloud dynamics, and aerosol particles during snow formation (Morrison et al., 2012; Griesche et al., 2021).

In situ snowfall observations are highly uncertain due to the nature of their measurement techniques and the strong spatial variability of precipitation. Moreover, such observations are almost entirely absent in remote polar regions. Ground-based remote sensing, such as weather radar, is typically limited to densely populated areas, with only a handful of radar-equipped sites in the polar regions. (e.g., Souverijns et al. (2018b); Li et al. (2021); Schoger et al. (2021); Matrosov et al. (2022); Tridon et al. (2022); Alexander et al. (2023)). As such, space-borne techniques are required to observe snowfall on a regional or global scale. Passive microwave sensors (Kidd et al., 2021) provide good spatial coverage due to their kilometre-scale imaging capabilities. However, they are impacted by surface properties (Skofronick-Jackson et al., 2004; Skofronick-Jackson and Johnson, 2011) and the presence of supercooled liquid water

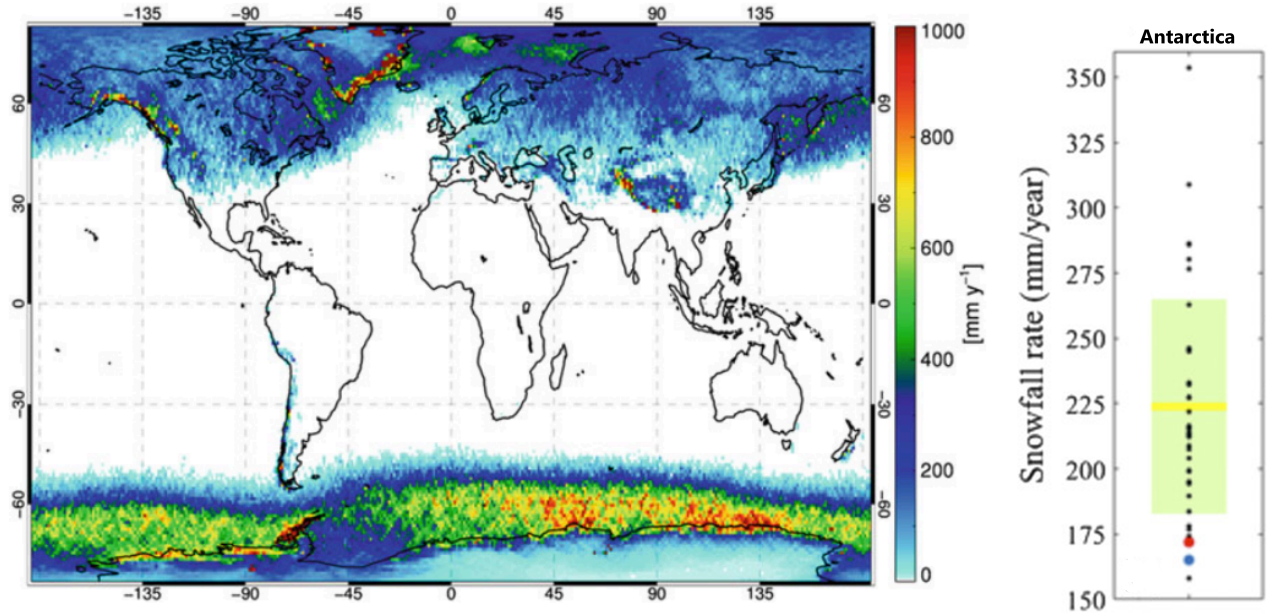

Figure 11: Left panel: CloudSat mean annual snowfall rate in 1° grid boxes for the 2006–2016 period. Despite averaging over 10 years, the data is noisy. Extracted from Kulie et al. (2020). Right panel: Mean annual snowfall rate (mm water equivalent per year) over Antarctica, from CMIP5 models (black dots), CloudSat observations for 2007–2010 (red dot). Note the substantial spread across model and observational estimates. Adapted from Stephens et al. (2018).

(Battaglia and Panegrossi, 2020; Panegrossi et al., 2022; Camplani et al., 2024), which are difficult to separate from atmospheric scattering contributions by frozen hydrometeors.

Due to their unique profiling capabilities, radar can provide detailed vertical profiles of hydrometeors and distinguish scattering by hydrometeors from the surface. Although converting radar measurements into snowfall rates introduces uncertainties, polar-orbiting satellites, such as CloudSat (Stephens et al., 2018) and EarthCARE (Wehr et al., 2023), provide some of the best opportunities for observing snowfall globally (Milani and Kidd, 2023). CloudSat snowfall measurements have been successfully evaluated against ground-based in situ data and radar networks (Mroz et al., 2021), leading to the development of snowfall climatologies (Liu et al., 2008; Palerme et al., 2014; Stephens et al., 2018; Bennartz et al., 2019; Kulie et al., 2020), which are especially valuable in regions with sparse in situ observations like Antarctica or Greenland. CloudSat data has also been used to investigate seasonal cycles (Kulie and Milani, 2018), to evaluate climate models (Palerme et al., 2017) and study the surface mass balance of ice sheets (Boening et al., 2012; Milani et al., 2018). However, CloudSat revisit time of 16 days, combined with its km-size footprint, led to sparse spatial sampling, introducing noise into snowfall climatologies even when averaged over a 10-year period (Figure 11).

CloudSat is also limited by surface clutter contamination and cannot observe snowfall in the “blind zone” (up to 1200 m above the surface), leading to potential underestimation of snowfall

rates for shallow events and overestimation in presence of sublimation (Maahn et al., 2014). Due to the similar design, these limitations also apply to EarthCARE.

The key scientific question related to “Polar Snowfall” is: **How can improved quantification of polar snowfall processes reduce uncertainties in snowfall accumulation and surface mass balance, and enhance the representation of snow-related processes in climate and weather prediction models?**

WIVERN Contribution to Goal 2 - Constraining Cloud and Precipitation Impacts on Climate

By providing global, high-resolution observations of vertically resolved cloud structure, mass, and dynamics, WIVERN will help reducing uncertainties in cloud feedbacks. It will offer unprecedented insight into the lifecycle of anvil clouds, including detrainment height, horizontal extent, mass flux, and thickness. Thanks to its beam-matched radar-radiometric mode, wide-swath coverage, high sampling frequency and reduced blind zone over the ocean, WIVERN will enhance sensitivity to and sampling of liquid precipitation and liquid water path in light rain and drizzle in shallow oceanic clouds, as well as snowfall in high latitudes.

3.5. Improving Numerical Weather Prediction and Earth System Models

Building on the enhanced understanding of storm dynamics and the improved constraints on cloud and precipitation processes described in the previous sections, WIVERN will provide crucial observations to advance NWP and Earth System Models (ESMs). These models are essential tools for understanding and forecasting atmospheric and climate processes. NWP models simulate the short-term evolution of the atmosphere, typically a few days ahead, while ESMs provide long-term projections of the Earth system spanning decades to centuries. In the decade to come, both types of model are expected to operate globally with kilometre-scale resolution. These future global km-scale models have the advantage that they can directly resolve the spectrum of storms and air motions associated with them. They will thus require fine-scale observations of the dynamic and cloud properties to evaluate and better constrain them.

For NWP, it is well established that a more accurate initial state leads to better forecasts. Data Assimilation (DA) schemes optimally combine the latest observations with the current model state, accounting for the uncertainties in both, to produce an improved initial state (i.e. analysis) for forecasting. Even emerging Artificial Intelligence (AI)-based forecasting systems rely on observations, to estimate the initial state, and to train the AI models. In the following, the need for better or novel observations to support DA (Section 3.5.1), model evaluation (Section 3.5.2), and AI-based approaches (Section 3.5.3) is explained.

3.5.1. Improving the Initial State of NWP Models

A weather forecast's accuracy is limited by how well the current state is known. Therefore, improving the current atmospheric state of numerical models through new global observing capabilities is a key lever for improving forecast quality.

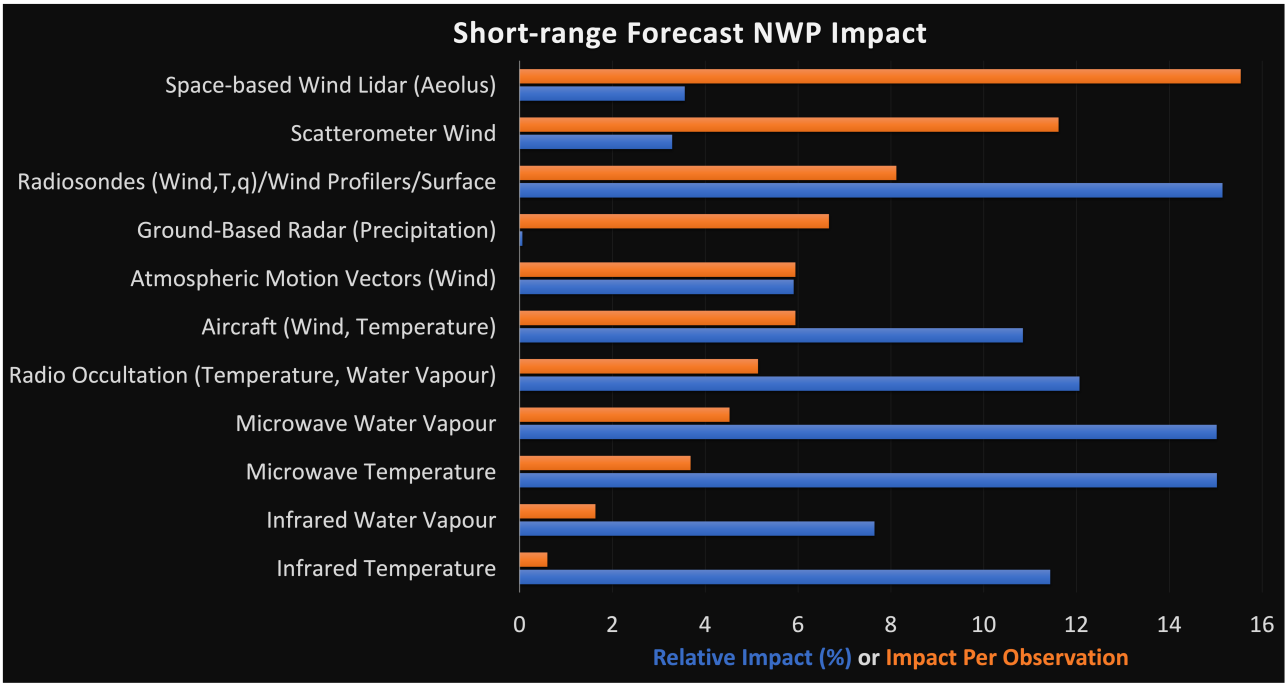

Figure 12: ECMWF global model FSOI results for the period December 2022 to February 2023. It shows the overall short-range forecast global NWP impact for each observation group i.e. relative FSOI (%) (blue) and this impact then normalised by the data count per observation group (orange) in arbitrary units.

The value of individual observations can be assessed using the Forecast to Sensitivity Observations Impact (FSOI) technique (Cardinali, 2009; Eyre, 2021), which quantifies how much each observation contributes to reducing short-range forecast error. Numerous studies (e.g., Baker et al., 2014; Horányi et al., 2015) have shown that, among all variables, **wind observations** have a particularly strong positive impact on NWP analyses and forecasts. This is confirmed in ECMWF FSOI scores which show that the impact per wind observation is particularly strong (see Figure 12). Wind measurements account for only 8% of the data count, yet provide 26% of the overall impact.

A prominent example is the Aeolus HLoS wind measurements; when assimilated into NWP models, they led to one of the strongest positive impacts for a single instrument, contributing ~3.5% (~4.5% in 2019) of the relative FSOI (Figure 12). NWP centre's Observing System Experiments (OSEs) further confirmed that assimilating Aeolus wind profiles led to statistically significant reductions in wind vector, temperature and humidity forecast errors by several per-

cent into the medium-range, with greatest improvements in the tropics (Rennie et al., 2021; Pourret et al., 2022). As a result, Aeolus data were operationally assimilated by ECMWF, the Deutscher Wetterdienst (DWD), Météo-France, and the UK Met Office between 2020 and 2023 (Pourret et al., 2022; Rennie et al., 2021; Martin et al., 2023), a remarkable achievement for a scientific demonstration mission lasting only a few years.

Next in the FSOI impact ranking per observation are ocean surface scatterometer winds, radiosondes and radar wind profilers. Then Atmospheric Motion Vector (AMV) winds account for ~6% of the relative FSOI. Recent studies have demonstrated their positive impact on forecasts, mostly in the lower and upper troposphere (Bormann et al., 2019; Chambon et al., 2023; Sasso et al., 2025). As shown in Figure 12, the AMV data comes via 16 satellites, however, lots of data are rejected in the assimilation, as they are typically associated with height-assignment errors, especially in the mid-latitudes over land. Additionally, as they are derived from infrared and visible observations, they are only sensitive to the upper layers of the clouds.

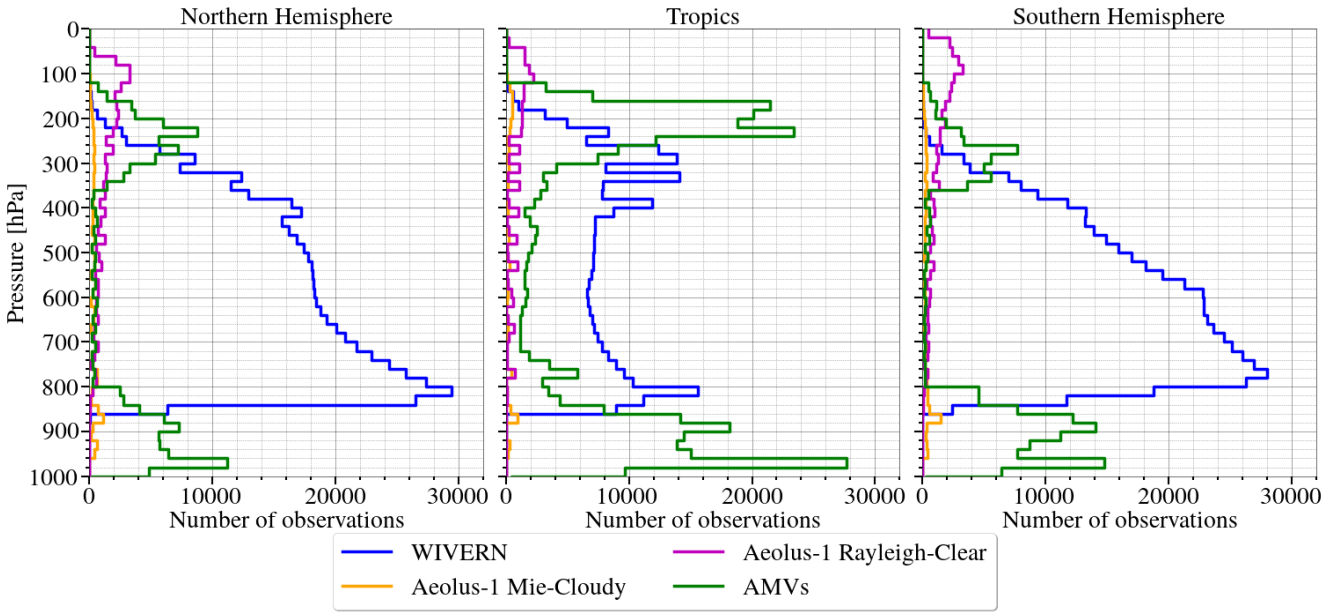

Figure 13: Histograms of the number of observations assimilated into the assimilation system, as if predicted using the Météo-France operational global NWP model (Bouyssel et al., 2022), averaged over a 21 day period in September 2021. It is clear that WIVERN data (blue) occurs in the areas with much lower coverage from AMVs (green) and Aeolus (magenta and orange). Taken from Sasso et al., 2025.

WIVERN will provide complementary observations of wind profiles within optically thick clouds, which are inaccessible to both AMVs and Aeolus-2. This is illustrated in Figure 13, which presents the daily average vertical distribution of AMV (green), Aeolus-1 Rayleigh-clear (magenta), Aeolus Mie-cloudy (yellow), WIVERN (blue) observations across the Northern Hemisphere (left), tropics (centre), and Southern Hemisphere (right). These average vertical distribution have been calculated using the global NWP model Action de Recherche Petite Echelle

Grande Echelle (ARPEGE) (Bouyssel et al., 2022) for a 3-week period in September 2021. In the stratosphere, the observations is largely dominated by Aeolus. The upper troposphere (above ∼300 hPa) and lower troposphere (below ∼850 hPa) are dominated by AMV data. In contrast, the mid-troposphere (between ∼850 and 300 hPa), particularly in the mid-latitudes, is primarily covered by the simulated WIVERN observations. This figure clearly demonstrates the vertical complementarity between Aeolus, AMVs, and WIVERN. By addressing the persistent observational gap of winds in cloudy and precipitating regions, WIVERN will improve NWP forecasts at all vertical levels within the troposphere, and in all geographical domains.

While wind observations are clearly valuable for defining the dynamic state, they are still sparse and unevenly distributed, compared to all kind of other observations. Indeed, of the total data count assimilated in the global ARPEGE model (~34 million observations) WIVERN contributes 4.2%, AMVs 1.7%, and Aeolus 0.4%, respectively. This further highlights a significant underrepresentation of wind observations, despite their crucial role in reducing forecast errors. Although great progress has been made in global NWP in recent decades, recent studies in predictability (e.g. Selz et al. (2022)) state that forecast skill still has plenty of room for improvement due to being far from saturated with observation information. Skillful forecast range could be extended by a further 4–5 days if initial condition errors were reduced by 90%, hence suggesting the need for much improved sampling of critical variables like the wind field.

In addition to wind data, **radar reflectivity observations** (a key parameter for detecting clouds and precipitation) are appealing for initialising NWP models, as they are highly sensitive to hydrometeors with excellent vertical resolution. The profiles are especially valuable for resolving vertical structures of clouds and precipitation, which are critical for studying mesoscale systems.

Over recent decades, radar reflectivity data has been primarily assimilated into km-scale NWP models, which feature high vertical and horizontal resolution (e.g., around 1 km for most operational mesoscale models). These models explicitly resolve convective storms, requiring fine-scale observations to better constrain and validate model outputs. As a consequence, ground-based radar reflectivities have been especially useful for regional NWP models, with many meteorological centres assimilating such data operationally (e.g., Caumont et al., 2010; Wattrelot et al., 2014; Simonin et al., 2017). These data are not distributed evenly at a global scale, and are therefore not used operationally in global NWP models.

At the global scale, NWP models are evolving to match the resolution of current regional models, thus potentially benefiting from assimilating these high resolution observations. Initial studies using space-borne radar observations, such as CloudSat 1.6 km swath and GPM 250 km swath, have shown significant improvements in global forecast errors (Janisková and Fielding, 2020; Ikuta et al., 2021b). These improvements are especially evident in oceanic regions, where ground-based radar data are unavailable (Ikuta et al., 2021b). The impact of reflectivity observations is expected to increase further as advanced ensemble-based DA techniques (e.g.,

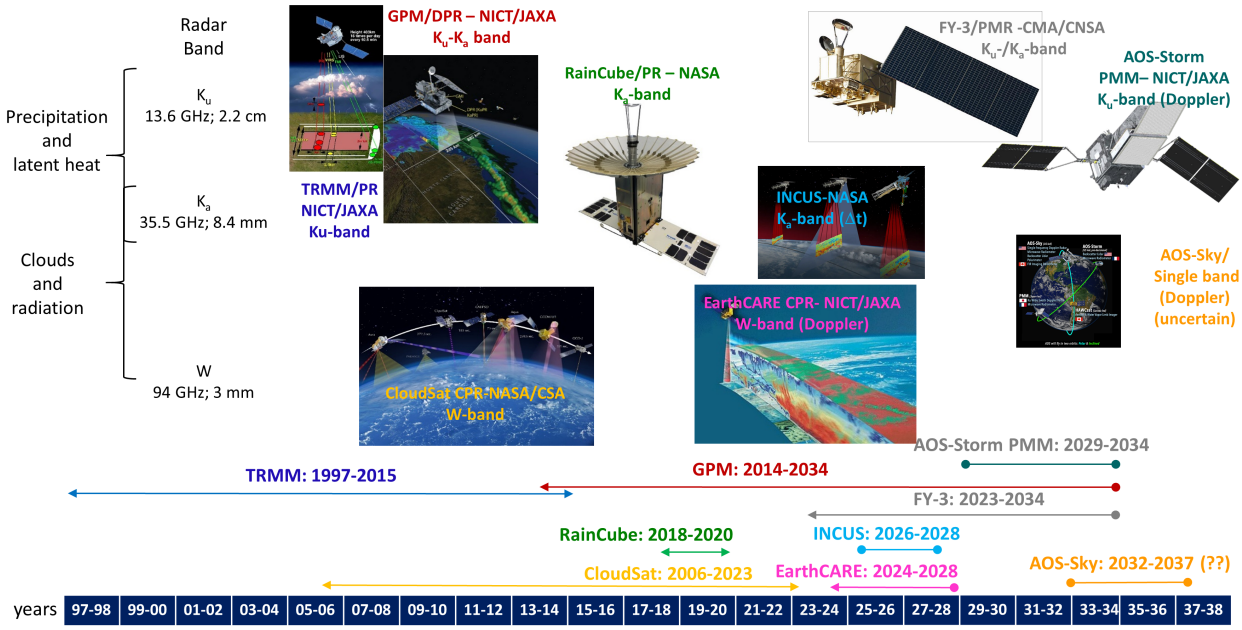

Figure 14: Mission timelines for past, present and future atmospheric radar missions with the relevance of their radar operating bands to the detection of clouds and precipitation (Battaglia et al., 2020).

4DEnVar) are implemented by 2030 to further constrain these cloudy-sensitive observations. This will optimise the extraction of cloud and precipitation information from reflectivity observations, providing greater potential for WIVERN, which will collect slanted vertical profiles across an unprecedented swath of 800 km.

Despite the importance of reflectivity measurements for reducing forecast errors, there are no plans for a space-borne atmospheric W-band radar in the next decade (Figure 14, Table 1).

Table 1: Strengths and weaknesses of past, present and future atmospheric radars shown in Figure 14.

	Band	Sensitivity [dBZ]	Swath [km]	Footprint [km]	Doppler (v_N [m s^{-1}])	Horizontal winds	Vertical winds
TRMM	Ku	17	250	5	✗	✗	✗
CloudSat	W	-28	1.4	1.4	✗	✗	✗
GPM-DPR/FY3-PMR	Ku/Ka	12/15	250	5	✗	✗	✗
INCUS	K	12	10	3	✗	✗	✓
EarthCARE	W	-35	0.75	0.75	✓(5-6)	✗	✓
AOS-Storm PMM	Ku	5	250	5	✓(35-40)	✗	✓
WIVERN	W	-23.5	>800	<0.8	✓(40)	✓	✓

In addition to active radar measurements of Doppler winds and reflectivity, passively sensed microwave frequency **Brightness Temperature (T_b) observations** are important for defining the initial conditions. T_b is sensitive to temperature, humidity, and hydrometeor contents, and indirectly affects dynamic variables through the Four-Dimensional Variational Data Assimilation (4D-Var) DA system, which adjusts the other fields (e.g., pressure, temperature, winds) and improves initial conditions (Geer et al., 2018). Studies show that T_b data improves forecast quality, especially in regions of active weather (Chambon et al., 2023; Geer et al., 2017; Duncan et al., 2021). T_b at 94 GHz, for example, can detect liquid water in clouds (Geer et al., 2017). This sensitivity is particularly important for studying tropical stratocumulus clouds over cold ocean waters, which have a significant cooling effect on Earth, but have been decreasing in the last two decades (Boukabara et al., 2020). T_b at 94 GHz is also highly sensitive to the humidity in the lowest levels of the atmosphere, and would therefore be beneficial to further constrain the analyses close to the ground in clear-sky as well as in cloudy conditions. Moreover, even if the constellation of passive microwave observation is already quite dense, recent studies have shown that there is no saturation effect of the assimilation of more satellite (Duncan et al., 2021). Therefore, the inclusion of WIVERN dual-polarisation T_b observations is expected to further enhance NWP model forecasts.

The key scientific question related to “Improving NWP Models” is: **How can enhanced global co-located in-cloud winds, and cloud and precipitation 3D structures improve the initial state representation in NWP models and lead to more accurate weather forecasts?**

3.5.2. Evaluating and Improving Earth System Models

Besides improving the initial state, observations are useful for model evaluation and improvement. In this section, our focus is on improving the next-generation of ESMs, recognising that both next-generation ESMs and NWP models share similar requirements for atmospheric parametrisations due to their similar grid spacing.

It is important to recognise that the horizontal grid spacing determines the type of processes that can be explicitly resolved by the fluid-dynamical equations. In the atmosphere, a grid spacing of 100 km can only resolve large-scale storms. Smaller-scale processes (Figure 15) must instead be represented by parametrisations, which statistically approximate their effects on larger-scale dynamics. Those parameterisations are a major source of uncertainty and well-known model biases (e.g. Fiedler et al., 2020), the most notable of which concerns the simulation of the spatial distribution of precipitation over the Indian Ocean and the Pacific warm pool (Figure 16). This issue has driven ongoing efforts to improve horizontal resolution within the constraints of available computational resources and the scientific problem being addressed.

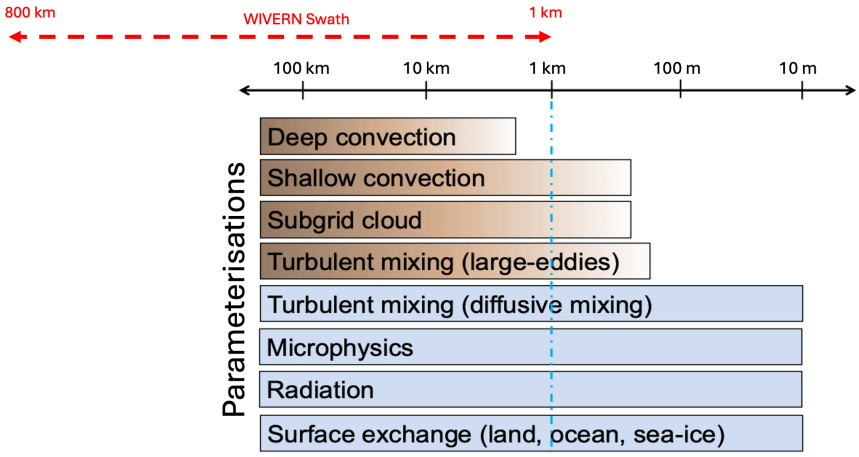

Figure 15: A list of atmospheric physical processes that require parametrisation at different model resolutions. Lighter colours mean that some models still parameterise that process, other do not. WIVERN will provide observations related to these processes across its 1 km footprint and 800 km swath.

Infobox 3.6: Parametrisation

In the climate and weather systems, many important processes, like cloud formation, happen on scales that are smaller than the grid spacing used by a numerical model (see Figure 15), meaning that such processes cannot be directly represented by solving the underlying physical equations. Instead, models rely on parametrisation, a method that uses simplified relationships to account for the effects of these processes based on the state of the model's grid-scale variables. Parametrisations are only approximate and are a source of major biases.

Currently, next-generation ESMs can already be integrated over decades with horizontal grid spacings of 5 to 10 km (Hohenegger et al., 2023; Rackow et al., 2025). Although the higher resolution allows for a more explicit representation of storms, not everything works perfectly out of the box and biases persist. This is so as some of the small-scale processes, especially turbulence and microphysics (Figure 15), have to remain parameterised.

Additionally, convective storms are often too poorly organised, with cluster sizes that are typically too small. A key feature in these next-generation models is that they are resolving (instead of parameterising) storms at the mesoscale, including the flow within them. Dedicated observations of mesoscale storm dynamics are therefore needed to improve climate simulations.

Fortunately, biases become apparent quickly and in many cases, even a single month of simulation is sufficient to reveal major model biases (Segura et al., 2025), provided that observational data are available to reconstruct the corresponding atmospheric state with enough detail, even at regional scales. Unfortunately, existing satellite systems with active sensors lack the spa-

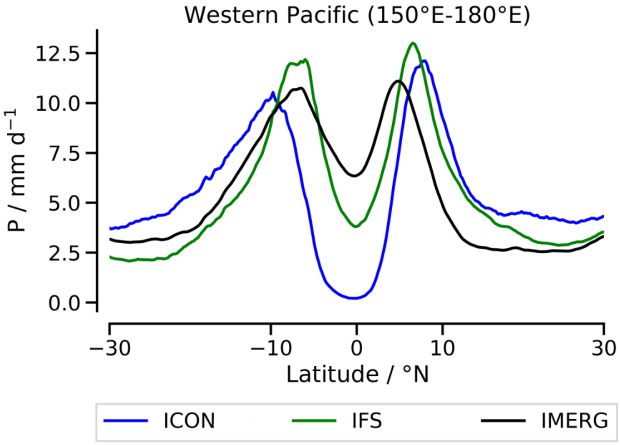

Figure 16: Latitudinal cross-section of precipitation over the Pacific warm pool (150°E–180°E) from two global kilometre-scale coupled climate models, the Icosahedral Nonhydrostatic model (ICON) model and the Integrated Forecasting System (IFS), compared with observations from the Integrated Multi-satellitE Retrievals for GPM (IMERG). Taken from Segura et al. (2025). Note especially how both models underestimate precipitation at the equator.

tial and temporal resolution required to capture rapidly evolving cloud structures, especially at regional scales. The high spatial and temporal sampling of WIVERN will overcome these limitations, offering the level of detail needed to effectively assess and improve model performance.

Moreover, an emerging frontier in model improvement is the use of observations to directly estimate uncertain model parameters. Techniques such as inverse modelling, variational methods, and machine learning are beginning to show promise in this area. For example, Kotsuki et al. (2020) demonstrated how satellite data can be used to estimate spatially varying microphysical parameters, such as the auto-conversion rate in cloud schemes. Similarly, Geer (2021) showed how retrievals can help to infer properties of frozen hydrometeors. Although still in their early stages, these approaches may become a powerful tool for improving model simulations by the time of WIVERN launch, and they could make use of the novel observations WIVERN will provide.

The key scientific question related to “Evaluating and Improving Earth System Models” is: **What are the causes for remaining biases in the representation of storms in kilometre-scale climate and weather models and can these biases be alleviated?**

3.5.3. Relevance of WIVERN for Fast-Moving AI-Based Models

As shown in Section 3.5.1, WIVERN observations will refine the initial state of the traditional physically-based NWP models. WIVERN data will be also very appealing for AI-based NWP models. AI is revolutionising weather forecasting by enhancing their accuracy and efficiency.

The incorporation of AI into the forecasting process has already demonstrated improvements in processing speed and the efficient management of vast and complex datasets, enabling the rapid delivery of forecast products without compromising accuracy (Schultz et al., 2021; Pathak et al., 2022).

AI-based weather prediction can be broadly divided into two categories. The first relies on training machine learning models using reanalysis datasets (e.g. ERA5: Fifth Generation ECMWF Reanalysis), which combine observations with NWP model outputs. These systems, such as FourCastNet (Pathak et al., 2022), Google DeepMind's GenCast (Price et al., 2025) and ECMWF AI Forecasting System (ECMWF, 2024), have demonstrated remarkable speed, up to 1,000 times more efficient than traditional physics-based models (ECMWF, 2024), but their performance is ultimately constrained by the quality of reanalyses datasets used for training.

A second, emerging class of models aims to forecast the weather by learning directly from observations alone, in a so-called Direct Observation Prediction (McNally et al., 2024) framework. These models bypass reanalyses, relying instead on large volumes of high-quality, frequent, and global observational data to learn the governing dynamics. While still in early development, they hold promise for reducing model biases and increasing robustness. The success of these approaches depends critically on the availability of high-quality observations across all key meteorological variables.

Accurate weather forecasts, whether based on traditional NWP or AI-driven systems, critically depend on the quality of the initial state of the atmosphere. The WIVERN core strength lies in its ability to refine this initial state by providing direct measurements of key variables such as wind and cloud properties. This will benefit all modelling frameworks, whether physically based or data-driven.

In the case of reanalysis-driven models, better observations lead to improved reanalysis products and thus higher-quality training datasets. Robust and frequent global observations are therefore essential to constrain and train AI models effectively, underscoring the ongoing importance of comprehensive satellite missions in the AI-driven forecasting era.

WIVERN capability to provide high-resolution, near-real-time, and simultaneous winds and cloud observations aligns seamlessly with the requirements of AI-driven forecasting systems. Its unprecedented 800 km swath and 600 m vertical resolution will deliver a significant amount of detailed three-dimensional data coverage, essential for initialising AI models that rely on accurate and timely atmospheric information. To provide context on the significance of WIVERN large observational coverage, in one week WIVERN will sample as much as CloudSat and EarthCARE do in a year.

These unique observations will address a critical gap in the existing observing system and supporting the development of robust, data-hungry AI forecasting tools. Finally, as for traditional NWP models, AI models require a GOS in which the observations complement each other in

terms of coverage (e.g. clear sky versus cloudy areas) and in terms of their sensitivity to the meteorological variables. It is particularly important for observation-only AI models to have observations in variables that users want for weather forecasts, therefore wind is crucial. It will help to map the information from more indirect observation types into wind space. As demonstrated in Sasso et al. (2025), WIVERN will perfectly meet this criteria by providing a unique set observations which is fully complementary to the other wind observations of the GOS.

The key scientific question related to "Relevance of WIVERN for Fast-Moving AI-Based Models" is: **How can high-resolution, near-real-time observations of in-cloud wind and cloud properties enhance the training, validation, and performance of both reanalysis-driven and observation-only AI-based weather prediction models?**

WIVERN contribution to Goal 3 - Improving NWP and Earth System Models

WIVERN will provide the first global dataset of co-located in-cloud winds and cloud and precipitation properties over an unprecedented swath of 800 km. It will improve NWP model analyses and Artificial Intelligence-based forecasts all over the globe. As all the meteorological variables are coupled, this improvement will not only impact the wind fields, but all the meteorological variables. WIVERN will also accelerate the issuance of weather alerts, thereby strengthening preparedness and response. Its unique dataset will also allow to better infer the links between the dynamics and the cloudy fields in the analyses.

WIVERN global, high-resolution observations of wind profiles, cloud structures, and hydrometeor distributions within storms are also critical for testing and refining the parametrisations (InfoBox 3.6). By providing detailed insights into storm dynamics and vertical transport of heat and moisture, WIVERN will help reduce uncertainties in how cloud systems and storms are represented in ESMs, ultimately leading to more physically consistent models and improved climate projections.

3.6. Unlocking Additional Science - WIVERN Secondary Science Objectives

The usefulness of the WIVERN radar pulses does not end when they pass through the atmosphere. In fact, their interaction with the Earth's surface will offer valuable insights into how the atmosphere connects with two other key parts of the climate system: the ocean and the cryosphere. These measurements, while considered secondary objectives, are closely linked to WIVERN primary objectives. For instance, observations of sea surface Doppler Frequency Shift (DFS) and Normalized Radar Cross Section (NRCS) will improve our understanding of surface ocean currents. When combined with in-cloud wind profiles and cloud properties, these observations will provide a more complete picture of air–sea coupling and how the ocean responds to changes in the atmosphere above. Similarly, collecting data over sea ice and land will support studies of polar snowfall, an important part of the water cycle in high-latitude re-

gions, and provide information on snow properties over sea ice and land, a critical factor in surface heat fluxes. Here, the focus is on the sea ice part and only slightly on snow properties on land, which nevertheless can be an important observational contribution by WIVERN. The following sections describe the current gaps in our knowledge in these areas, and how WIVERN observations can help to close them.

3.6.1. Bridging Observational Gaps in Polar Sea Ice and Snow for Climate Research

Sea ice is a crucial component of the global climate system, covering approximately 4 to 7% of the global ocean. It acts as a barrier to heat, momentum, and gas exchange, notably water vapour, between the ocean and atmosphere. Due to its high albedo compared to ice-free ocean, sea ice plays a significant role in the global radiation balance.

Due to the remoteness and inaccessibility of the polar regions, satellite remote sensing is the only means of obtaining comprehensive global data on sea ice. The strong decline in Arctic sea ice during the last decades could only be observed by the satellite climate data record, which has been available since the 1970s. This decline is one of the most striking indicators of recent climate change, yet the full dynamics and feedback mechanisms driving this loss, particularly associated with Arctic amplification, remain poorly understood, nor are they accurately represented in current climate models (Dai et al., 2019; Rantanen et al., 2022; Wendisch et al., 2023).

Several key parameters related to sea ice are essential for assessing its role in the climate system, as well as for understanding, modelling, and ultimately predicting its temporal evolution. These include sea ice coverage, sea ice thickness, sea ice structure and type, and the snow cover on top of the ice. Also, narrow, linear openings in the sea ice, called leads, contribute significantly to heat exchange between ocean and atmosphere.

Since the 1970s, daily satellite monitoring has provided global sea ice coverage estimates, with an initial spatial resolution of $\sim$50 km, improving to $\sim$5 km since 2002. However, higher spatial resolution sea ice information is urgently required, as regional climate models now operate at grid resolutions of 1 km or finer. Additionally, shipping and offshore industries depend on high-resolution ice data for navigation and operational planning. However, existing satellite observation systems with resolutions finer than 1 km face following limitations:

- SAR provides high-resolution imagery but does not provide global sea-ice coverage on a daily basis, and an automatic retrieval of sea ice concentration is very challenging.
- Infrared (IR) and visible sensors offer detailed observations but are impacted by cloud cover and the latter are limited to daylight conditions which is a serious limitation because of high cloudiness of polar seas and the lack of daylight in winter.

The least understood parameter related to sea ice is the snow layer covering the ice surface.

Snow has a significant insulating effect and thus modulates the sea ice growth below, and has a much higher albedo than the bare sea ice, and the albedo strongly depends on the snow type and grain size. Thus, snow properties are essential for determining the surface energy balance in polar regions. Additionally, accurate knowledge of snow depth is essential for estimating sea ice thickness from space and, consequently, the global sea ice volume. Unfortunately, snow depth is highly variable in both space and time, influenced by snowfall, snow drift, redistribution, and physical transformation processes (Massom et al., 2001).

Several satellite-based methods exist for retrieving snow depth on sea ice, including those based on microwave scattering properties (e.g., Rostosky et al., 2018), and dual-frequency altimetry (Guerreiro et al., 2016; Kacimi and Kwok, 2022). However, both techniques have significant uncertainties, often related to the uncertain penetration of the microwaves into the snow, and remain an active area of research and development.

To fully understand the thermodynamic impact of snow on sea ice, measuring snow depth alone is insufficient; its microphysical properties such as structure and density are also needed. Currently, no satellite method can retrieve this information, as existing microwave instruments lack the optimal combination of frequencies and polarisations. Moreover, sensors are usually either active (radar) or passive (radiometers), but not both simultaneously, limiting comprehensive snow characterisation.

Upcoming microwave missions face key limitations when it comes to snow observation. The Radar Observation System for Europe in L-band (ROSE-L) operates at long wavelengths, which are insensitive to snow. Other missions, such as Copernicus Imaging Microwave Radiometer (CIMR) and Copernicus polar Ice and Snow Topography ALtimeter (CRISTAL), include frequencies up to 37 GHz, which offer some sensitivity to snow depth but limited information on snow structure and type. Although EarthCARE uses a higher frequency (94 GHz), it is nadir-viewing only, meaning it cannot capture the difference between horizontally and vertically polarised emission or backscatter from the surface

One of the key uncertainties in Arctic Amplification is the strength of the lapse rate feedback, which is considered the dominant feedback mechanism, especially outside summer melt (Pithan and Mauritsen, 2014). This feedback is highly dependent on ice surface temperature, which in turn is strongly influenced by snow insulation properties. Additionally, the loss of sea ice removes a physical barrier to moisture exchange, potentially increasing atmospheric humidity. This could both increase the water load in polar storms and amplify warming. Yet there is no direct observational constraint on this process at relevant spatial and temporal scales.

The key scientific question related to “Bridging Observational Gaps in Polar Sea Ice and Snow for Climate Research” is: **How can the representation of polar feedback mechanisms in climate models be improved and uncertainties in polar climate projections be reduced?**

WIVERN Contribution to Polar Sea Ice and Snow Observations

WIVERN unique combination of active and passive microwave observations at 94 GHz with both vertical and horizontal polarisations at an oblique incidence angle, allows the retrieval of high-resolution sea ice concentration (approximately 1 km), detection of leads (>100 m width), and retrieval of novel snow properties.

3.6.2. Revealing What Satellite Altimetry Misses: Advancing Our Understanding of Ocean Surface Current Dynamics

The ocean is a fundamental component of the Earth system, covering more than 70% of the planet's surface. It carries approximately half of the total poleward heat flux at mid-latitudes (Czaja and Marshall, 2006) and accounts for almost 90% of the excess heat storage in the Earth system between 1960 and 2020 (von Schuckmann et al., 2023). Its interactions with the atmosphere play a crucial role in triggering and shaping tropical and extra-tropical cyclones. It is evident that a motionless ocean would perform these vital functions dramatically differently. The state of motion of ocean waters, the currents, therefore represents a critical regulating factor within the Earth system and must be systematically observed, understood, and modelled. Beyond its role as a climate regulator, the ocean is also essential to a wide range of maritime activities that serve society at multiple levels. Shipping, maritime safety, fisheries, renewable energy, pollution response, environmental management, resource exploitation, port and harbour operations, and recreation all depend on accurate knowledge of ocean currents. This underscores the need for continued monitoring and enhanced understanding of oceanic flows.

In situ monitoring of ocean currents at the global scale is currently performed in the framework of two main programs, the ARGO profiling floats array (Roemmich et al., 2019), and the Global Surface Drifter Array (Centurioni et al., 2019). Satellite monitoring is exclusively performed through radar altimetry (Fu and Cazenave, 2001; Mulet et al., 2021). While existing satellite observations provide valuable insight into ocean currents, they also have significant limitations in terms of spatial coverage, temporal resolution, and accuracy. Satellite altimetry measures sea surface height and estimates currents indirectly, assuming the ocean is in balance (hydrostatic and geostrophic) and flows in large-scale patterns. This means it cannot capture the full picture of Total Surface Current Vector (TSCV). The method is insensitive to the non-geostrophic current components, which are wind-driven or inherently transient features, such as surface Ekman drift, and Near-Inertial Oscillations (Demol et al., 2025; Penven et al., 2014). This limitation is a consequence of the observation method itself and affects even the most advanced altimetry missions, Sentinel-6 (Poseidon-4 Delay-Doppler Altimeter) (Donlon et al., 2021) and SWOT (KaRIN swath altimeter) (Fu et al., 2024).

Due to the lack of remote sensing alternatives that are sensitive to the TSCV, the only available information to quantify the issue comes from in-situ observations, which are highly labor-

intensive, remain spatially and temporally sparse, and are subject to several well-known observation biases (e.g. limited coverage during the winter period in the Southern Ocean, and the difficulty to maintain autonomous platforms in regions with divergent surface Ekman flow). This has led the WMO to state in its Global Climate Observing System (GCOS) 2022 Implementation plan that: “Currently, space-based estimates of near-surface currents are produced by combining surface geostrophic currents derived from altimetry and Ekman Current derived from ocean-surface wind stress (e.g., from scatterometers). They are more representative of mixed-layer currents than surface currents. Moreover, the geostrophic and Ekman theories break down near the equator, preventing reliable estimates of the currents from altimetry and scatterometry measurements. Direct measurements of surface currents from space are thus needed.”

Space-borne Doppler radar, as demonstrated by Romeiser et al. (2005), using Shuttle Radar Terrain Mapping (SRTM) data, or Chapron et al. (2005), using ENVISAT/ASAR data, offers an alternative observation technique which is sensitive to the TSCV. These experiments were however limited in time.Doppler radars have since been at the core of multiple proposed space missions, including three ESA Earth Explorer candidates (SKIM, HARMONY, and SEASTAR) and NASA-CNES’s Ocean DYnamics and Surface Exchange with the Atmosphere (ODYSEA) mission (with a selection decision expected in mid-2025). HARMONY has been chosen as the 10th ESA Earth Explorer mission. The development of these missions has fostered a growing community of potential scientific users and significantly advanced the maturity of Doppler-based current measurement techniques. The technical characteristics of HARMONY, particularly its sub-km scale spatial resolution, make it well-suited for providing instantaneous, high-resolution current observations of the coastal ocean or areas of specific interest, such as western boundary currents or eastern boundary upwelling systems. However, due to data downlink constraints, this high resolution coverage will only be available over 34% of the global ocean, leaving the remaining two thirds unobserved, highlighting a clear need for a complementary mission focused on the open ocean.

Opportunistically using the WIVERN ocean surface radar echo is a great step towards this objective. For the first time on a global scale, Doppler observations of WIVERN could provide insights into the dynamics of ocean current features that altimetry alone cannot capture, such as:

- Non-geostrophic currents that are climatically significant, such as Ekman drift, Near-Inertial Waves, highly energetic structures, and the ocean’s rapid response to extreme atmospheric forcing.
- Ocean currents in regions where geostrophic balance is less relevant, such as at the equator with Tropical Instability Waves, which modulate sea surface temperature variability.

The capability of WIVERN to complement the geostrophic current estimates produced operationally by the altimeter constellation with direct global measurements of the ocean TSCV will lift the long-standing observational deadlock preventing this question to be addressed, thereby bringing a decisive contribution to the field of oceanography. Beyond surface current measurements, WIVERN also presents an exciting opportunity to explore the potential of spaceborne W-band microwave radar for ocean science. In particular, WIVERN could contribute to the development of W-band surface wind scatterometry, expanding its product portfolio to include synergistic observations of air-column winds, surface winds, and ocean currents. Notably, ODYSEA, while dedicated to ocean surface wind and current measurements, lacks a concurrent air-column wind observing capability, a gap that only WIVERN can fill.

The key scientific question related to “Advancing Our Understanding of Ocean Surface Current Dynamics” is: **How do non-geostrophic processes contribute to global surface current variability, and how can improved simultaneous observations of the atmosphere and ocean enhance our understanding of air–sea interactions and ocean circulation?**

WIVERN Contribution to Ocean Current Observation

WIVERN offers new insights into the dynamics of surface currents in regions where geostrophic balance breaks down, such as the equatorial ocean, and during episodes of strong atmospheric forcing. Additionally, it provides co-located observations of air-column winds, surface winds, and ocean currents that opens new opportunities to study air–sea interactions at the global scale.

4. RESEARCH OBJECTIVES

This chapter summarises the mission scientific objectives and outlines how the identified scientific gaps and questions can be addressed through the proposed mission objectives.

4.1. Science Goals and Objectives

Following the background and science justifications provided in, the key scientific contributions of the WIVERN mission are divided into primary and secondary objectives, which are well aligned with those outlined in ESA's Living Planet Programme (ESA, 2015).The Primary Science Objectives (PSOs) address the Living Planet Challenges under the Atmosphere (A) theme, while the Secondary Science Objectives (SSOs) contribute to the Cryosphere (C) and Ocean (O) themes.

4.1.1. Primary Science Objectives (PSO)

The PSOs are structured around three key scientific goals:

- Understanding storms
- Constraining cloud and precipitation impacts on climate
- Improving Numerical Weather Prediction (NWP) and Earth System Models (ESMs)

4.1.1.1. Understanding Storms

The science objectives under this goal are:

PSO 1.1: Storm Structure and Dynamics

Improve the understanding of storm dynamics by quantifying the strength, structure, and horizontal extent of internal circulations across the full spectrum of storm types, from small convective systems just a few kilometres wide to large storms spanning up to 800 km, across Earth's wide range of climates. Particular emphasis is on the role of in-storm horizontal mesoscale circulations and vertical wind shear driving the organisation and intensification of systems such as mesoscale convective systems, tropical and extratropical cyclones, and polar lows.

PSO 1.2: Water, Heat, and Circulation

Gain insight into the coupling between water, heat and circulation by quantifying the relationship between the 3D mass structure, the 3D heat structure, and the resulting internal circulation as a function of storm type, and by characterising the relationship between storms, environmental mesoscale circulation, and large-scale circulation.

The combination of these objectives will lead to a better understanding of storms and will increase our confidence in how properties of storms (e.g. intensity, propagation, location) will change as the climate warms. Ultimately, this will help to better characterise which storms are capable of significantly modifying the large-scale circulation of the atmosphere. This will also bring clarity to the controversial discussion about the role of internal versus external dynamics controlling the storm lifecycle and on thermodynamics (moisture/heat) versus dynamics (wind) control.

These science objectives address **Living Planet Challenge Atmosphere A4** which focuses on: *interactions between changes in large-scale atmospheric circulation and regional weather and climate.*

4.1.1.2. Constraining Cloud and Precipitation Impacts on Climate

The science objectives under this goal are:

PSO 2.1: Anvil Cloud Feedback

Determine the relationship between convective mass flux in tropical convective storms and the area and depth of the high anvil clouds they generate to better constrain climate sensitivity.

PSO 2.2: Precipitating Oceanic Shallow Clouds

Improve quantitative estimates of shallow precipitation over the oceans in trade cumulus and stratocumulus regimes, and investigate how this precipitation influences the organisation of shallow clouds and affects the sign and magnitude of their climate feedbacks.

PSO 2.3: Polar Snowfall

Improve the quantification and understanding of polar snowfall processes to reduce uncertainties in snowfall accumulation, assess surface mass balance, and better represent snow-related processes in climate and weather prediction models.

These objectives address **Living Planet Challenges Atmosphere A1, A2 and A4** which focus on:

A2: *Interactions between the atmosphere and the Earth's surface involving natural and anthropogenic feedback processes for water, energy and atmospheric composition*; **A1:** *Water vapour, cloud, aerosol and radiation processes and the consequence of their effect on the radiation and the hydrological cycle*; and **A4:** as above.

Objective PSO 2.3 addresses **Living Planet Challenges Cryosphere C2 and C3** which focus on: **C2:** *Mass balance of grounded ice sheets, ice caps and glaciers, their relative contribu-*

tions to global sea-level change, their current stability and their sensitivity to climate change; and **C3:** *Seasonal snow, lake/river ice and land ice, their effects on the climate system, water resources, energy and carbon cycles; the representation of the terrestrial cryosphere in land surface, atmosphere and climate models*.

4.1.1.3. Improving Numerical Weather Prediction (NWP) and Earth System Models (ESMs)

The science objectives under this goal are:

PSO 3.1: Numerical Weather Prediction

Improve the representation of the initial state of the atmosphere in NWP models, and hence, the quality of weather forecasts.

PSO 3.2: Earth System Models

Advance the representation of cloud, precipitation, and associated dynamical processes in ESMs by providing global, high-resolution observations of in-cloud wind profiles and cloud properties.

PSO 3.3: AI-Based Models

Improve AI-based weather forecasting models by providing unique observations as training and input data.

These objectives address **Living Planet Challenges Atmosphere A1, A2 and A4** as above.

4.1.2. Secondary Science Objectives (SSO)

The SSOs are structured around two important scientific goals:

- Bridging Observational Gaps in Polar Sea Ice and Snow for Climate Research
- Revealing What Satellite Altimetry Misses: Advancing Our Understanding of Ocean Surface Current Dynamics

4.1.2.1. Bridging Observational Gaps in Polar Sea Ice and Snow for Climate Research

The science objectives under this goal are:

SSO 1.1: Sea Ice Coverage

Enhance the resolution of sea ice concentration retrievals and of the statistics of leads (linear openings in the sea ice).

SSO 1.2: Snow on Sea Ice

Characterise properties of snow on sea ice, i.e. distinguish new, fresh-fallen snow from older, multi-layered snow, and estimate the depth of new snow.

These objectives address **Living Planet Challenges Cryosphere C1 and C4** which focus on:

C1: *Regional and seasonal distribution of sea-ice mass and the coupling between sea ice, climate, marine ecosystems and biogeochemical cycling in the ocean*; and **C4:** *Effects of changes in the cryosphere on the global oceanic and atmospheric circulation*.

4.1.2.2. Revealing What Satellite Altimetry Misses: Advancing Our Understanding of Ocean Surface Current Dynamics

The science objectives under this goal are:

SSO 2.1: Non-Geostrophic Ocean Currents

Characterise the spatial and temporal evolution of non-geostrophic ocean currents, and quantify their components that remain undetected by satellite altimetry (e.g., Ekman drift, Near-Inertial Oscillations, Equatorial currents, and tidal currents).

SSO 2.2: Air-Sea Interaction

Explore the potential of WIVERN concurrent measurements of surface currents and wind profiles to improve modelling and understanding of air-sea exchange processes.

These objectives address **Living Planet Challenges Ocean O2, O3 and O4**, which focus on:

O2: *Mesoscale and sub-mesoscale circulation and the role of the vertical ocean pump and its impact on energy transport and biogeochemical cycles*; **O3:** *Response of the marine ecosystem and associated ecosystem services to natural and anthropogenic changes*; **O4:** *Physical and biogeochemical air–sea interaction processes on different spatiotemporal scales and their fundamental role in weather and climate*.

4.2. Mission Objectives

In response to the PSOs outlined above, the following Primary Mission Objective is proposed:

WIVERN Primary Mission Objective

To provide near-real-time measurements of the following geophysical parameters: a) Horizontal Line of Sight (HLoS) winds, b) Vertical winds, c) Liquid Water Path (LWP), c) Ice Water Content (IWC), d) Snowfall Rate (SR), and e) Rain Rate (RR). These quantities are observed over an 800 km swath at a horizontal and vertical resolutions of 1 km and 600 m, with a quasi-daily revisit for each $20 \times 20\,\mathrm{km}^2$ region up to $\pm 80^\circ$ latitude.

WIVERN Primary Science Goals		
Goal-1: Understanding Storms	**Goal-2:** Constraining Cloud and Precipitation Impacts on Climate	**Goal-3:** Improving Numerical Weather Prediction and Earth System Models
WIVERN Primary Science Objectives (PSOs)		
PSO 1.1: Storm Structure and Dynamics **PSO 1.2: Water, Heat, and Circulation**	**PSO 2.1: Anvil Cloud Feedback** **PSO 2.2: Shallow Clouds** **PSO 2.3: Polar Snowfall**	**PSO 3.1: Numerical Weather Prediction** **PSO 3.2: Earth System Models** **PSO 3.3: AI-based Models**
WIVERN Primary Mission Objectives (PMOs)		
To provide near-real-time measurements of the following geophysical parameters:		
Wind Products: - Horizontal Line of Sight (HLoS) winds - Vertical winds		**Cloud Products:** - Liquid Water Path (LWP) - Ice Water Content (IWC) - Snowfall Rate (SR) - Rain Rate (RR)
Mission Requirements		
To provide measurements of the following instrument parameters: ○ Profile of Doppler Velocity (V_D) ○ Profile of Reflectivity (Z), and Polarimetric Variables (e.g. Z_{DR}, Φ_{DP} and ρ_{HV}) ○ Brightness Temperature (T_b) ○ Polarimetric Normalised Radar Cross Section (NRCS) (σ_0)		
These features are observed using a conically scanning polarimetric cloud radar, with a novel radiometric mode, over an 800 km swath, at a horizontal and vertical resolutions of 1 km and 600 m, with a quasi-daily revisit for each 20 × 20 km² region up to ±80° latitude.		

Figure 17: Traceability between WIVERN Primary Science Goals, Objectives, Mission Objective, and Requirements.

The mission objectives for the primary science goals and objectives, along with the mission objectives and requirements, are presented in Figure 17.

The primary geophysical products measured by WIVERN are briefly defined below:

HLoS Wind (V_{HLoS}): Horizontal wind along the horizontally-projected Line of sight (LoS) direction [$\mathrm{m\,s^{-1}}$];
Vertical Wind (w): Upward or downward motion of air in the atmosphere [$\mathrm{m\,s^{-1}}$];

Liquid Water Path (LWP): Total amount of liquid water contained in the atmospheric column [$g\,m^{-2}$];
Rain Rate (RR): Precipitation rate from liquid hydrometeors (rain, drizzle) [$mm\,h^{-1}$];
Ice Water Content (IWC): Mass of frozen hydrometeors (ice and snow) per unit volume of atmospheric air [$g\,m^{-3}$];
Snowfall Rate (SR): Water-equivalent precipitation rate from frozen hydrometeors (snow, ice) [$mm\,h^{-1}$].

In response to the SSOs outlined above, the following Secondary Mission Objectives are proposed:

WIVERN Secondary Mission Objective - Sea Ice and Snow

To provide: a) high-resolution (1 km) sea ice concentration, b) snow type (discrimination of new, fresh-fallen and old, multi-layered snow), and c) snow depth of the new snow (approximate saturation at 10 cm).

WIVERN Secondary Mission Objective - Ocean Current

To provide: a) Line-of-Sight surface current velocity, and b) 10 m scatterometric surface winds.

The mission objectives for the secondary science goals and objectives, along with the mission objectives and requirements, are presented in Figure 18. The secondary science goals are identical to those for the PSOs, as the secondary data products do not drive the mission requirements.

WIVERN Secondary Science Goals	
Bridging Observational Gaps in Polar Sea Ice and Snow for Climate Research	Advancing Understanding of Non-Geostrophic Ocean Currents and Air-Sea Interaction
WIVERN Secondary Science Objectives (SSOs)	
SSO 1.1: Sea Ice Coverage **SSO 1.2: Snow Properties on Sea Ice**	**SSO 2.1: Non-Geostrophic Ocean Currents and Their Components.** **SSO 2.1: The Potential of WIVERN's Concurrent Measurements of Surface Currents and Wind Profiles to Better Understand of Air-Aea Interaction.**
WIVERN Secondary Mission Objectives (SMOs)	
To provide measurements of:	
- Sea Ice Concentration - Surface Snow Type (discrimination of new snow and multi-layer (old) snow) - Snow Depth of the New Snow	- Line-of-Sight Surface Current Velocity - 10 m Scatterometric Surface Wind
Note: These objectives can be achieved under cloud-free or thin-cloud conditions.	
Mission Requirements	
Mission requirements are identical to those defined for the primary mission objectives, as given in Figure 3.1.	

Figure 18: Traceability between WIVERN Secondary Science Goals, Objectives, Mission Objective, and Requirements.

5. DATA PRODUCTS

The WIVERN data products are summarized in Figure DAT-174 and detailed in table DAT-104.

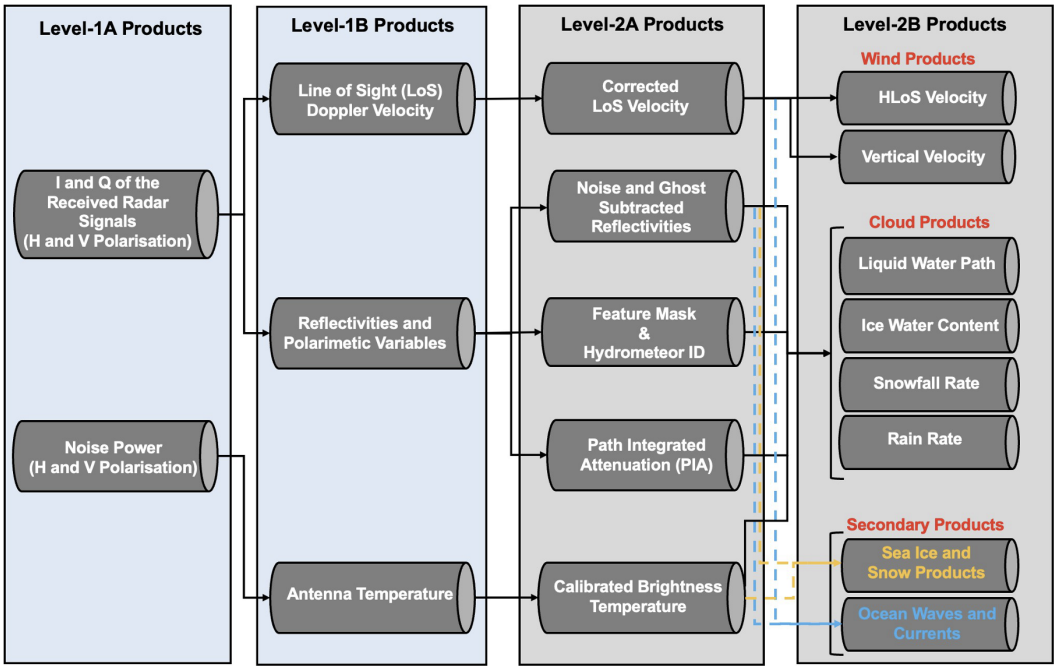

Figure **DAT-174**: WIVERN Level-0 to Level-2B products

WIVERN Level-0 to Level-2 products description

Level-0	Measurement data Instrument source packet (ISP) data with: • Unprocessed (raw) I and Q data per pulse (H and V) per range gate • Noise power measurement (H & V) for the radiometer mode • Instrument housekeeping data • Platform housekeeping/AOCS data

continued on next page...

...continued from previous page

Level-1A	Measurement data • Unprocessed (raw) I and Q data per pulse (H and V) per range gate • Noise power measurement (H & V) for the radiometer mode • Auxiliary data, including instrument and platform house-keeping/AOCS data, geolocation and radiometric calibration data, are appended but not applied, and when needed, are processed, e.g., up-sampled to PRF. All data are time-referenced.

continued on next page...

...continued from previous page

Level-1B	Measurement data • Internally calibrated reflectivities (H & V channels, co-polar and cross polar components) • Internally calibrated polarimetric variables (ZDR, ρHV) and LDR (when measured) • Internally calibrated mean (e.g., 1 km-averaged) LoS Doppler speed, corrected for satellite velocity and mis-pointing, using the Level-1b Doppler calibration techniques described in section 5.4.1.3 of the RfA. • Calibrated brightness temperatures in H and V over both an ITU protected frequency band within 100MHz (94.0-94.1GHz) and a partially unprotected frequency band of 500MHz (that includes the protected band of 100MHz). The calibration consists in using the internal calibration data related to the radiometric mode (receiver gain and offset correction with two point calibration). The calibration also includes antenna pattern correction in order to derive the brightness temperature of the observed scene from the overall antenna temperature (correction of the brightness temperature contribution integrated over the antenna sidelobes). Each measured brightness temperature over protected or partially unprotected bands have time/frequency flag wrt presence of RFIs. RFIs are detected via 3rd and 4th Stokes parameters (via the detection of an anomalous amplitude) as a minimum, and any simple and easy detection method TBD to implement (TBC). • Calibrated 3rd and 4th Stokes parameters over both an ITU protected frequency band within 100MHz (94.0-94.1GHz) and a partially unprotected frequency band of 500MHz(that includes the protected band of 100MHz). Detection of RFI is performed via the detection of an anomalous amplitude of the Stokes parameters wrt a threshold. Gridding, geolocation and formatting are performed at this stage on the measurement data.

continued on next page...

...continued from previous page

Level-2A	Measurement data • Externally calibrated reflectivities (ZHH and ZVV) after ghost and gas attenuation correction • Externally calibrated polarimetric variables (ZDR, PhiDP, rhoHV • Externally calibrated mean LoS Doppler speed using the Level-2A Doppler calibration techniques described in section 5.4.1.3 of the RfA. • Externally calibrated brightness temperature using ECMWF model • Gas attenuation profile • Feature mask • Hydrometeor Identification from reflectivities and polarimetric information
Level-2B Wind	Measurement data • Calibrated LoS winds at measurement scale • Calibrated HLoS winds at measurements scale corrected for vertical air motion (determined from hydrometeor phase, ice temperature and calibrated reflectivity) • Calibrated HLoS winds at observation scale (1, 5 and 20 km horizontal averages) • Convective classification, stratiform vs. Convective precipitation identifier • Up and downdraft motion identifier
Level-2B Cloud and precipitation	Measurement data • IWC from reflectivity, temperature and brightness temperature • LWP, from brightness temperatures at H and V and surface reference technique path integrated attenuation • Rain/Snowfall rates from attenuation of surface return and reflectivity profile • Attenuation correction profile

continued on next page...

...continued from previous page

Secondary Level-2B Sea Ice and Snow	• Sea ice Concentration • Surface Snow Type (discrimination of new snow and multi-layer (old) snow) • Snow Depth of the new Snow
Secondary Level-2B Ocean	• Line-of-Sight Surface Current Velocity • 10 m Scatterometric Surface Wind

6. MISSION REQUIREMENTS

6.1. Observation (Level 2) Requirements

6.1.1. Level 2B Wind Products

Doppler velocities should be estimated using the “pulse pair” technique by measuring the phase shift between the returns from successive transmitted pulses. From space at 94GHz (3.2mm), the phase shift reaches 180º for a target movement of 800 µm. So, to achieve a folding velocity of ± 40 m/s, a pulse separation of 20 µs (or 3 km slant range) is needed. To achieve this, the “polarisation diversity pulse pair” (PDPP) technique could be implemented whereby the two pulses (separated by a default 20 µs (TBC)) are labelled H and V. Provided that the H and V pulses are transmitted, backscattered and received independently, the phase shift from the two pulses can be measured (Wolde et al., 2019).

Two distinct WIVERN Doppler products are envisaged:

a) HLoS winds (the horizontal component of the Line of Sight (LoS) winds) that are representative of the large-scale flow over horizontal distances of 20km or more and are therefore candidates for data assimilation.

b) Transient convective motions which are detected by changes in the LoS Doppler shift on the scale of 1 km. The aim is to identify convective regions by the level of these changes at the km scale as opposed to stratiform regions where the km-to-km LoS Doppler changes are much lower. For convective regions, these km-to-km LoS changes will be expressed in terms of the statistics of the frequency, and magnitude of convective motions. These statistics can then be used to validate the new generation of climate and NWP models that now explicitly represent convection. So far, the convective motions have not been resolved in climate and NWP models, but the effect of convection has been parameterised.

6.1.1.1. HLoS winds corrected for mis-pointing at the observation scale (Level 2B)

In “stratiform” regions, (i.e. areas without vertical motions exceeding 1 m/s), in-cloud LoS wind measurements are directly related to the HLoS wind, i.e. the horizontal wind along the horizontally projected
LoS direction, which is representative of the large scale horizontal winds that are assimilated in NWPs. To ensure the accuracy and representativeness of these HLoS winds for DA, a horizontal averaging scale of 20 km has been selected. This scale is consistent with the resolution of global NWP models and allows sufficient signal averaging to reduce retrieval uncertainty.

OBS-36 Random error L2B HLoS winds

The random error of the Level-2B HLoS velocity estimates shall be less than 2.6 m/s over a 20km integration distance for radar targets with reflectivities higher than -15dBZ (Threshold) / -21dBZ (Goal).

Note: *integration distance of 20 km implies that a sufficient number of pulse pairs are transmitted over this integration length as function of peak power and PRF.*

Confidence Level : 1-sigma
Satisfied by : OBS-142
Satisfies : Primary Mission Objectives

OBS-37 Systematic error L2B HLoS winds

The systematic error of the Level-2B HLoS velocity estimates shall be less than 1 m/s (Threshold) an ideally below 0.5 m/s (Goal).

Confidence Level : 1-sigma
Satisfied by : OBS-143
Satisfies : Primary Mission Objectives

6.1.1.2. Vertical winds

WIVERN will measure winds at a native horizontal resolution of 1 km. At high SNR (SNR > 10 dB), the noise in WIVERN Doppler measurements will be substantially reduced even at 1 km integration distance (see 6.3). This enables the detection of vertical motions associated with strong convection, which induce LoS velocity changes over kilometre-scale distances that are distinguishable from larger-scale wind variability. Accordingly, the vertical wind requirement is defined as follows:

OBS-193 Random error L2B vertical winds

The random error of Level-2B vertical wind estimates shall be less than 5 m/s (Threshold) / 3 m/s (Goal) over a 1 km integration length, for echoes with reflectivities greater than -10 dBZ.

Confidence Level : 1-sigma
Satisfies : Primary Mission Objectives

OBS-194 Systematic error L2B vertical winds

The systematic error of Level-2B vertical wind estimates shall be less than 1 m/s (Threshold) and ideally below 0.5 m/s (Goal).

Confidence Level : 1-sigma
Satisfies : Primary Mission Objectives

6.1.2. Level 2B Cloud and precipitation products

6.1.2.1. Ice water content (IWC)

For IWC, the WMO has defined observational requirements for uncertainties of 20% (Goal), and 100% (Threshold), over horizontal resolutions of 5, 15, and 50 km, and time intervals of 1, 3, and 12 hours, respectively (World Meteorological Organization, 2016).

Extensive aircraft imagery of ice particles (Hogan and Illingworth, 2006) and theoretical studies carried out in support of the EarthCARE mission (Mason et al., 2023) have demonstrated that IWC retrieved from W-band radar reflectivities has a root mean square (RMS) error of approximately +110%/-70%. The uncertainty varies with IWC magnitude, with the lowest errors occurring for IWC values around 0.1 g/m^3(Protat et al., 2007).

Due to the WIVERN sensitivity, only ice clouds with IWC greater than 10^{-2} g/m^3 are expected to be detected.
These clouds represent the vast majority (> 95%) of the total ice mass present in the atmosphere. WIVERN measurements will be noisy at 1 km, thus averaging will be needed to reduce the noise; a 5 km integration is set as a baseline for the IWC requirement.

OBS-10 Random error L2B IWC

At a horizontal scale of 5 km, the random error of the Level-2B IWC, shall be lower than a factor of 2 (+100%, -50%) (Threshold) / 1.5 (+50%, -33%) (Goal) for IWC exceeding 10^{-2} g/m^3.

Satisfied by : OBS-149
OBS-154

Satisfies : Primary Mission Objectives

OBS-11 Systematic error L2B IWC

At a horizontal scale of 5 km, the systematic error of the Level-2B IWC, shall be lower than 30% (Threshold) / 15% (Goal) for IWC exceeding 10^{-2} g/m^3.

Satisfied by : OBS-149
OBS-154

Satisfies : Primary Mission Objectives

6.1.2.2. Liquid water path (LWP)

The WMO has defined observational requirements for LWP uncertainties of 10 g/m^2 (Goal), and 50 g/m^2
(Threshold), over horizontal resolutions of 5, 15, and 50 km, and time intervals of 1, 3, and 12 hours,
respectively.

OBS-15 Random error L2B LWP

At a horizontal scale of 2 km, the random error of the Level-2B LWP over ocean shall be less than 40 g/m^2 or 40% (Threshold) / 20 g/m^2 (Goal), whichever is larger.

Satisfied by : OBS-149
OBS-154

Satisfies : Primary Mission Objectives

OBS-16 Systematic error L2B LWP

At a horizontal scale of 2 km, the systematic error of the Level-2B shall be lower than 40 g/m^2 (Threshold) / 20 g/m^2 (Goal).

Satisfied by : OBS-149
OBS-154

Satisfies : Primary Mission Objectives

6.1.2.3. Precipitation rates

Regarding surface **Rain Rate**, the WMO global NWP requirements are very ambitious with respect to
the current space-borne observing capabilities, with threshold/breakthrough/goal values of 1, 0.2, and
0.1 mm/h rates, at horizontal scales of 50, 15, and 5 km, and temporal resolutions of 12, 3, and 1 hours,
respectively (World Meteorological Organization, 2016)

Experience from previous missions (e.g., CloudSat and GPM) has demonstrated that, due to the spatial and temporal variability of cloud and precipitation fields, improvements in the GCOS precipitation records can only be achieved through a multi-source, synergistic approach. This approach combines GEO, LEO, and ground-based observations, each contributing to specific precipitation regimes (Hayden and Liu, 2018). The recipitation product from the Integrated Multi-satellitE Retrievals for GPM (IMERG) represents a compelling example of how to exploit the GCOS, producing global precipitation at 0.1° x 0.1° with 30-minute resolution (Huffman et al., 2020).

The envisaged role for WIVERN is to:

(a) Provide a reference for cross-calibrating other observing systems (e.g., passive MicroWave (MW) radiometers, infrared radiometers), using the WIVERN Level-2B products;

(b) Produce cloud and (light to medium) precipitation datasets for verification of NWP models through the exploitation of Level-3 products.

Regarding **Snow Rate**, the CloudSat CPR was commonly considered the best calibrator of

snowfall within the passive MW radiometer constellation (Mroz et al., 2023), with the EarthCARE CPR now extending the CloudSat heritage. Similarly, the GPM Dual-frequency Precipitation Radar (DPR) is the accepted benchmark for the entire GPM constellation for rainfall rates between 0.5 and 10 mm/h (Skofronick-Jackson et al., 2018). WIVERN will generate snowfall products of comparable quality to CloudSat CPR and serve as a reference for light-to-moderate oceanic rainfall rates ranging from 0.02 to 2 mm/h (Berget al., 2010).

The only viable method for establishing verifiable criteria for instantaneous precipitation products is to rely
on ground-based radar networks (e.g., the OPERA European network) as the reference for evaluating coincident satellite and ground-based observations. To account for potential geolocation discrepancies and temporal variations, the requirements are defined for spatially averaged quantities. Accordingly, the precipitation products requirements are defined as follows:

OBS-20 Random error L2B rain rates

Averaged over 5 x 5 km^2, the random error of the Level-2B rain rates shall increase from 50% (Threshold) / 30% (Goal) at light rain (0.02 mm/h) to 100% (Threshold) / 50% (Goal) for moderate rain (2 mm/h).

Satisfied by : OBS-149
OBS-154

Satisfies : Primary Mission Objectives

OBS-21 Systematic error L2B rain rates

Averaged over 5 x 5 km^2, the systematic error of the Level-2B rain rates shall be less than 30% (Threshold) / 15% (Goal).

Satisfied by : OBS-149
OBS-154

Satisfies : Primary Mission Objectives

OBS-179 Random error L2B snow rates

Averaged over 5 x 5 km^2, the random error of the Level-2B snow rates shall be lower than a factor of 2 (Threshold) / 1.5 (Goal), for rates exceeding 0.1 mm/h (melted equivalent).

Satisfied by : OBS-149
OBS-154

Satisfies : Primary Mission Objectives

OBS-180 Systematic error L2B snow rates

Averaged over 5 x 5 km^2, the systematic error of the Level-2B snow rates shall be lower than 30% (Treshold) / 15% (Goal), for rates exceeding 0.1 mm/h (melted equivalent).

Satisfied by : OBS-149
OBS-154
Satisfies : Primary Mission Objectives

6.1.3. Secondary Data Products Observation Requirements

The secondary data products observation requirements do not drive the mission requirements. Instead, they rely on the requirements already established for the primary products. WIVERN will provide two sets of secondary products. Although secondary, these products are expected to achieve an accuracy closely following the requirements outlined by the WMO.

6.1.3.1. Sea Ice and Snow Products Requirements

The WMO GCOS requirements for Sea Ice Concentration (SIC) and snow depth on sea ice are summarised in Table Table OBS-227 and Table OBS-252 respectively. Note that the snow type is not an Essential Climate Variable yet, as it has never been a retrieved variable till now. Also, note that WIVERN is mainly sensitive to snow depth of new, fresh-fallen snow while the GCOS requirements are for snow depth independent of snow type.

OBS-204 Sea Ice Concentration

WMO GCOS requirements for Sea Ice Concentration (SIC) are shown in table OBS-227 below (WMO et al., 2022).

Table **OBS-227**: Requirements for SIC

	SIC Uncertainty	**Horizontal Resolution**	**Temporal Resolution**
Goal	5%	1 km	< 1 day
Breakthrough	N/A	5-25 km	1-7 days
Threshold	10%	1 km	30 days

OBS-228 Snow Depth

WMO GCOS requirements for Snow Depth are shown in table OBS-252 below (WMO et al., 2022).

Table **OBS-252**: Requirements for Snow Depth

	Snow Depth Uncertainty	**Horizontal Resolution**	**Temporal Resolution**
Goal	1 cm	1 km	1 day
Breakthrough	5 cm	25 km	7-30 days
Threshold	10 cm	1 km	30 days

6.1.3.2. Ocean Surface Current Products Requirements

The WMO GCOS requirements for ocean surface current observations, as specified in Requirement #508 of the OSCAR, are summarised in Table OBS-256, along with the requirements for WIVERN HLoS current velocity, in three different pointing knowledge scenarios.

There are currently no requirements set for the scatterometric 10 m wind product, as considerable work remains before any firm commitments can be made. Establishing these requirements will necessitate a sufficiently large dataset encompassing a variety of environmental conditions. This assessment will need to be conducted prior to launch.

OBS-350

WMO requirements for TSCV are shown in Table OBS-256 below.

Table **OBS-256**: WMO requirements for ocean Total Surface Current Vector (TSCV), based on World Meteorological Organization (2016), Requirement #508.

	HLoS Current Velocity Uncertainty	**Horizontal Resolution**	**Temporal Resolution**
Goal	10 cm/s	50 km	24 h
Threshold	50 cm/s	1000 km	6 days

6.1.4. Level 2A products

6.1.4.1. Hydrometer ID and feature mask

Methods of distinguishing clouds and other hydrometeors from radar noise and surface clutter shall be based on the algorithms developed by Marchand et al., 2017 for CloudSat and by Kollias et al., 2023 for EarthCARE.
For WIVERN, the additional doppler velocity information should be used to distinguish rain from ice-cloud and to identify whether the ice is in the form of small crystal, or larger aggregates.

6.1.4.2. LoS Doppler at the measurement scale (Level 2A)

LoS Doppler at measurement scale of 1km in the LoS direction (TBC), is corrected using satellite pointing information for any mis-pointing due to, for example, TED. This shall be provided in the Level 2A Doppler product, which will be used to characterise HLoS winds and transient convective motions mentioned above.

In areas identified as stratiform, the calibrated LoS wind will be horizontally projected (HLoS) and corrected for the vertical motion contribution determined from the hydrometeor phase (solid, melting, liquid) and dependent on the temperature and calibrated reflectivity.

In areas identified as convective, the calibrated LoS winds will be used to characterise convective motions under the assumption that the HLoS winds change smoothly from the adjacent stratiform areas.

Proper procedures to identify stratiform and convective regions need to be defined during the SciReC studies.

OBS-142 Random error L2A LoS winds

The random error of the Level 2A LoS winds shall be less than 2.4 m/s times the sine of the LoS incidence angle for an integration distance of 20km for a radar target averaging -15dBZ (Threshold) / -18dBZ (Breakthrough) / -21dBZ (Goal) assuming no atmospheric attenuation and assuming a dielectric factor $\|K_w\|^2$ for the radar targets of 0.75 (water at 10 °C at 94 GHz) (Tanelli et al., 2008).

Note 1: *pointing contributions with frequency content at satellite level higher than the split frequency of 1e-5Hz (i.e. corresponding to 1 day period) are to be considered as part of the random contribution.*

Confidence Level : 1-sigma
Satisfied by : MSR-14
Satisfies : OBS-36

OBS-143 Systematic error L2A LoS winds

The systematic error of the Level 2A LoS winds shall be less than 0.5 m/s (Goal) / 1 m/s (Threshold) times the sine of the LoS incidence angle for an integration distance of 20km.

Note 1: *this assumes that non-geophysical contributions to the systematic error are corrected with external geophysical calibration techniques.*

Note 2: *pointing contributions with frequency content at satellite level lower than the split frequency of 1e-5Hz (i.e. corresponding to 1 day period) are to be considered as part of the systematic contribution.*

Confidence Level : 1-sigma
Satisfied by : MSR-15
Satisfies :
OBS-37

6.1.4.3. Calibrated reflectivities (Level 2A)

ECWMF have shown that for CloudSat comparisons of observed reflectivity profiles over several orbits with the forward modelled values of reflectivity from the IFS can provide relative calibration better than 1dB. This approach also has the advantage that any malfunction of the radar can be detected with a few hours of its occurrence and the cause investigated.

Absolute calibration is more challenging. CloudSat and EarthCARE use the cross section of the Ocean surface at incidence angle of about 10 degrees, but these are not available for WIVERN. Real time comparisons with climatology and intercalibration with non-scanning or cross-track scanning W-band systems envisaged for the WIVERN era will be considered. This is being currently investigated by SciReC (Battaglia et al., 2022)).

OBS-149 L2A Reflectivity accuracy

Reflectivities after absolute calibration shall be known with an accuracy less than 1dB.

Satisfied by : MSR-6
MSR-99
Satisfies : OBS-10
OBS-11
OBS-15
OBS-16
OBS-20
OBS-21
OBS-179
OBS-180
MSR-2

6.1.4.4. Calibrated polarimetric variables (Level 2A)

Calibrated polarimetric variables per channel are as reported in the Level 1B product, Z_{DR}, Φ_{DP}, ρ_{HV} and LDR if this variable is implemented. The accuracy of these variables is independent of the absolute calibration and will depend upon the SNR and the number of samples.

OBS-146 Z_{DR} accuracy

Z_{DR} after absolute calibration shall be known with an accuracy less than 0.5dB.

Satisfies :

6.1.4.5. Calibrated brightness temperatures (Level 2A)

OBS-154 Brightness temperature accuracy

The brightness temperature shall be calibrated using ECMWF operational forecast model for cloud free scenes over the ocean with an accuracy less than 2K (G) / 5K (T).

Justification :	The protected ITU band is 94.0-94.1GHz. Goal accuracy is justified by the use of 500MHz bandwidth, depending on presence of RFI sources. The impact of RFI sources on the radiometer functionality has been assessed with the conclusion that it is limited to local effects.
Satisfied by :	MSR-52 MSR-53
Satisfies :	OBS-10 OBS-11 OBS-15 OBS-16 OBS-20 OBS-21 OBS-179 OBS-180

6.1.4.6. Gas Attenuation Profile

The gas attenuation profile at 94GHz will be derived with an accuracy of 0.5dB from the profiles or temperature, pressure and humidity held in the ECMWF operational analysis. This is well established from CloudSat and EarthCARE heritage (Kollias et al., 2023).

6.1.5. Dynamic and measurement range

An analysis of Aeolus winds (Mike Rennie ECMWF) indicates that to cover the range of wind speeds encountered in the troposphere, WIVERN shall be capable of delivering HLoS wind speeds over the range 0 to ± 150 m/s. (TBC) equivalent to ± 100m/s LoS.

The Doppler radar should be able to provide unambiguous LoS winds up to at least ± 40 m/s. In case of folding above 40 m/s, a maximum of one-fold would be expected for a range of ± 120 m/s LoS. There are several decades of experience in unfolding single folds from ground-based scanning radars and the algorithms are well established and reliable. LoS Doppler unfolding could be easy to recognise as sudden jumps in LoS Doppler, e.g. a 100 m/s wind with Nyquist ± 40 m/s, would read as + 20 m/s, which is a 80 m/s jump from one range gate to the next one. This will be studied in Phase 0 by the science teams.

OBS-42 Reflectivity measurement range

Reflectivities shall be retrieved between -30dBZ and +30dBZ.

Satisfied by : MSR-101

OBS-43 HLoS winds dynamic range

The dynamic range of the Level 2B HLoS wind product shall be $\pm$ 150m/s.

Satisfied by : MSR-103

OBS-44 Brightness temperature dynamic range

The brightness temperature T_b shall be retrieved between 40K to 340K.

Satisfied by : MSR-102
Satisfies :

6.1.6. Spatial Error Correlation

No spatially correlated errors either in the vertical or horizontal arising from the instrument design are anticipated at this stage. They may become apparent after launch. For data assimilation in NWP, correlated observation errors are detrimental (if not accounted) for in the data assimilation observation error covariance matrix. The following requirement is based on the current definition for Aeolus-2.

OBS-49 HLoS winds spatial correlation

The HLoS wind error spatial correlation shall have an absolute value < 0.1 for a distance of 100km horizontally and 1km vertically (TBC).

Justification : Following the approach of DWL/Aeolus-2 EURD requirement

6.1.7. Probability of gross errors

Based on experience of using 94GHz radar data from CloudSat for 14 years, and many years of operational ground-based Doppler weather radars and wind profilers, spurious signals giving gross errors in reflectivity and Doppler estimates are very rare. Individual gates can be affected by aircraft or flocks of birds. Such echoes occur can be removed by speckle filters. More widespread low level Z echoes can be caused by insects.

OBS-138 Probability of gross errors

The probability of gross errors shall be less than 5% within a wind speed range of 6 times the random error requirement. Outside this wind speed range the gross error shall be 0% (TBC).

Note: *Gross errors are usually localised and due to returns from aircraft or migrating birds, a flexible "speckle" filter can be used to reject them at Level 2B.*

Justification : Following the approach of DWL/Aeolus-2 EURD requirement

6.2. Geometry and Temporal Requirements

In this section the geometry and temporal mission requirements are described, including the target observables, the required spatial and temporal sampling, spatial and temporal coverage, observational dataset length, data timeliness, and geolocation knowledge accuracy.

In order to obtain in-cloud horizontal wind components, the optimal WIVERN instrument view angle, satellite altitude and observation concept shall be studied and optimized to ensure that the mission meet the geographical coverage, vertical and horizontal sampling, revisit and Level 2 observation requirements which are discussed in the sections and chapters below.

6.2.1. Measurement technique

MIS-6	Measurement technique
The measurement technique shall allow the instrument to deliver range resolved Doppler and reflectivity profiles with H and V polarisation channels, and the receiver background noise level.	

6.2.2. Viewing geometry

In order to provide NWP models with wind information characterizing both zonal and meridional parts of the wind component, different parts of the in-cloud wind velocity component should be sampled. Simultaneous multi-angle sampling is not needed for this, and hence a conically scanning line-of-sight observing system would be a suitable option. Such an option would also address the need for global observations with frequent revisit time.

MIS-10	Conically scanning geometry
The observation concept shall allow sampling of range resolved in-cloud Doppler radar reflectivity and brightness temperature from different viewing angles from a conically scanning radar antenna with respect to the Earth geodetic reference frame WGS 84.	

An illustration of the WIVERN view geometry concept described in Illingworth et al. (2018) is shown in Figure MIS-85.

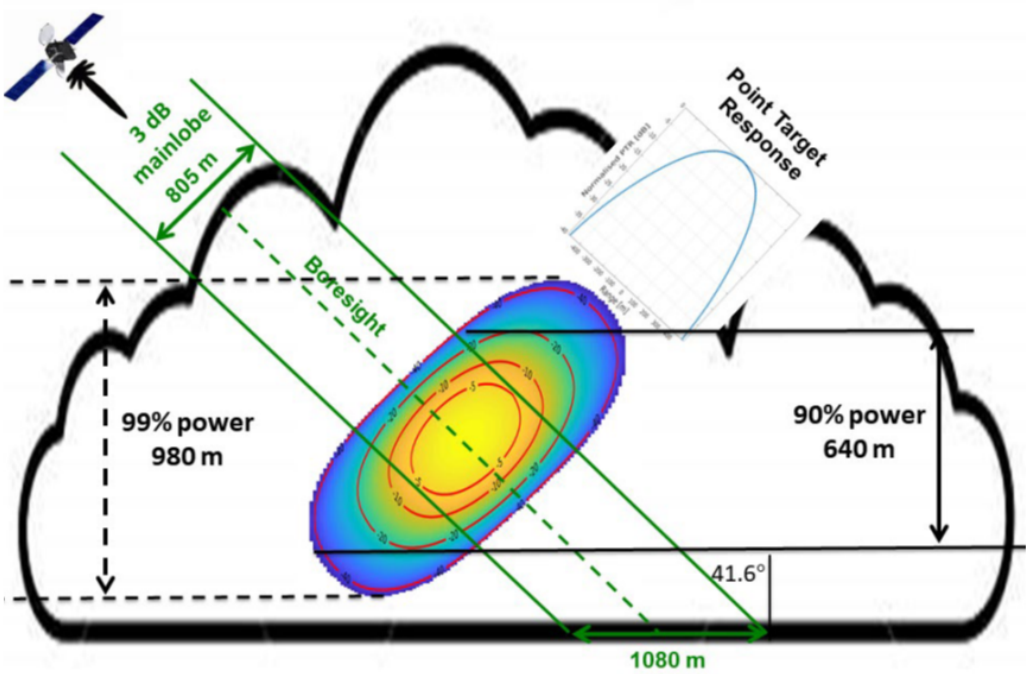

Figure **MIS-85**: WIVERN viewing geometry, antenna pattern, and schematic for a 3.3 μs (500m line of sight resolution) pulse, from Battaglia et al. (2022).

Note that accurate pointing knowledge of the radar boresight in azimuth and elevation will be needed to compensate for the Doppler shift introduced by the satellite motion sensed by the rotating antenna. This correction is vital for accurate Doppler observations. Monitoring of the range to the sea surface as the antenna rotates could be useful for monitoring any changes in elevation pointing. Simultaneous multi-angle observations, providing vector wind information for each measurement, are not needed

Note that from space the conventional Pulse Pair Doppler technique will have limited applicability because of the rapid decorrelation of the targets, so alternative methods should be sought after, such as “Polarisation Diversity Pulse Pair” with two closely spaced pulses polarised H and V (Pazmany et al., 1999).

Further note that the radar should be able to transmit pulse pairs with either H-V or V-H polarisation and to transmit single pulses polarised either H or V with reception in both H and V. This would enable to measure and characterize the strength of the depolarization ratio for the different targets (hydrometeors, surface), which is critical in the generation of ghost echoes.

Note that the use of circular polarisation has been considered. It could potentially lead to a simplification of the payload (i.e. use of circulizer and re-use of an existing rotary joint). However, it has significant scientific drawbacks among which an increased level of ghosts in the data as well as a poor performance on the secondary priority products (LWP, Rain rates, etc.).

The viewing geometry in Fig MIS-85 shows that the vertical resolution (640m) is dominated by the beamwidth of the radar pulse, so increasing the resolution along the slant path of the radar pulse per se has a minimal effect in improving the vertical resolution. However, if more independent samples of radar reflectivity (Z) were available then both the sensitivity of the reflectivity estimate and its precision of the fluctuating signal would both be improved. This could be achieved either by transmitting a longer chirped pulse and compressing it, or transmitting several pulses but hopped in frequency.

MIS-107 Use of pulse compression

The use of pulse compression or pulses hopped in frequency to obtain more independent samples of reflectivity shall be examined.

6.2.3. Horizontal and vertical coverage and sampling

6.2.3.1. Horizontal domain and coverage

The satellite instrument shall be able to sample the whole globe, and the coverage in the polar areas should be maximized as far as possible up to at least 85 degrees (threshold, TBC). Due to the small field of view (FOV) of the Doppler radar (~1 km footprint on-ground), this quasi global coverage would for example be achievable within 1 to 2 days with a conically scanning concept. An assessment suggests that an observation swath width of at least 800 km would be needed, and as reported in World Meteorological Organization (2016).

It was also shown in Ikuta et al. (2021a) that the assimilation of dual frequency precipitation radar reflectivity profiles leads to positive impact with a swath width of 245 km (GPM). Therefore, a larger impact is expected from a sample swath width of 800 km.

MIS-16 Horizonthal domain

The horizontal domain to be covered by the measurements shall be global, with a threshold requirement to cover the Earth up to at least 85 degrees latitude (TBC).

Note: 800km sample swath is the baseline, but a study of the optimal swath width from the NWP point of view should be undertaken and should consider the number and precision of the winds obtainable when there are changes in the orbit height and the elevation angle of the conically scanning antenna. These changes will affect the radar beamwidth and the permitted range of the radar pulse repetition rate which will in turn affect the vertical resolution and the signal-to-noise ratio at the greater ranges.

6.2.3.2. Horizontal product resolution

The horizontal product resolutions refer to the horizontal size of the Level 2 observations, as referenced to WGS84. The observation resolution requirements are as specified below.

MIS-115 L2A horizonthal resolution

The horizontal Level 2A cloud microphysical and brightness temperature products resolution shall be not greater than 1 km along the track of the radar footprint.

Requirement previously called OBS-184

MIS-116 L2B along track resolution

The along track resolution of the Level 2B HLOS wind speed product shall be not greater than 1 km.

Requirement previously called OBS-185

Note that the product list and definition are provided in Section 5.

6.2.3.3. Instrument horizontal sampling of target reflectivities

The instrument horizontal sampling shall be the smallest horizontal sampling of the Earth's clouds possible with the instrument, and hence should be on the scale of each pulse pair for the WIVERN instrument concept. In order to ensure maximum flexibility of the on-ground data processing, the I and Q data shall hence be available on-ground per pulse pair.

The minimum number of I and Q samples at the horizonthal sampling is not directly constrained but it shall be derived from the performance requirements (e.g. noise in doppler wind estimate).

6.2.3.4. Vertical domain

The vertical domain shall include the vertical atmospheric extent from the ground, including the atmospheric targets that shall be sampled to provide the Level 1 and Level 2 products. WIVERN aims at providing in-cloud winds from ice and liquid hydrometeors in the troposphere. The Earth troposphere ranges from the ground up to about 10 km in polar winter conditions and up to 20 km in the tropics (Stephens et al., 2018). The upper limit of 20 km covers cirrus (Heymsfield et al., 2017) and deep convection clouds in the tropics (Gettelman et al., 2002). Both will be detectable by 94 GHz radar. The WIVERN mission shall provide products in this vertical domain.

MIS-34 Vertical atmospheric domain

The vertical atmospheric domain to be sampled with the radar shall be from -5 km (i.e. below the Earth surface (geoid) to sample subsurface ghosts) and • up to 20 km altitude above the Earth surface (geoid) for the latitude range between 50deg South and 50deg North and • up to 10 km altitude above the Earth surface (geoid) for the latitude range above 50deg North and below 50deg South.

Note 1: *To accommodate deep tropical clouds the design should include the possibility of using lower PRFs.*

Note 2: *For CloudSat and EarthCARE, the surface clutter is close to the surface which affects data quality up to ~1km altitude. WIVERN points off-nadir, so the surface clutter is expected to be significantly reduced and the depth of the blind zone close to the surface reduced. Studies are underway in SciRec to address this issue.*

6.2.3.5. Vertical product resolution

The vertical product resolutions refer to the vertical separation of the Level 2 observations, as referenced to the Earth-centric coordination system at the Earth surface. The observation resolution requirements are as specified below

The mean tropospheric vertical wind shear is ~5 m/s per km and higher in regions of disturbed weather (Houchi et al., 2010). To resolve such shear, the vertical resolution must be better than 1 km. HLOS wind shear in the ECMWF operational Integrated Forecasting System (IFS) model is frequently 20-30 m/s per km in and around frontal systems. In 2030, the vertical model grid resolution will be around 200-300 m, and higher in the 2030s. Therefore, a vertical resolution down to 100 m would be desirable for the WIVERN L2 HLOS product. WIVERN points off-nadir, so, it is more convenient to specify the slant path resolution, which can then be converted to a vertical resolution. If the slant path range resolution is refined, it may be possible to better resolve the detail of the wind profile when there is a high shear.

MIS-119 L2 slant range resolution

The slant path range resolution of the Level 2 geophysical products shall be not greater than 750 m (threshold), 500 m (breakthrough), 100 m (goal).

6.2.3.6. Slant Path Instrument Sampling

In order to ensure the data quality, the slant path profiles shall be oversampled in range by a factor of three.

MIS-94 Oversampling slant range

Along the slant path the signal shall be oversampled by a factor of three.

6.2.4. Temporal Coverage and Sampling

6.2.4.1. Number of global observations per day

Analysis of the cloud climatology from CloudSat in the EE11 proposal [RD-1] showed that if accurate Doppler can be obtained for 20km horizontal averaging along the instrument measurement track for targets > -15 dBZ, then over one million in-cloud winds per day should be retrieved. Further analysis is required to assess the characteristic, amount and typical errors at the different heights in the different latitudinal bands.

WIVERN aims at measuring atmospheric winds at a scale of 1 to 20 km. As a scientific expectation, WIVERN will provide more than 1,000,000 in-cloud wind observations per day at 20km scale.

6.2.4.2. Geographical revisit time

The global revisit time is the time between two measurements by the instrument at the exact same atmospheric geolocation. An exact geographical revisit on a short time scale can only be achieved by geostationary systems or by polar orbiting platforms with a wide instrument swath, with a faster revisit at high latitudes. For polar orbiting platforms, a certain swath is also needed to fully cover the poles. It is noted that for global NWP model applications, the total number of geographically well distributed observations (across the globe) per day is more important than an exact revisit over a specific geographical location. To achieve this, a polar orbiting satellites with a suitable swath width is required.

For winds derived from clouds and precipitation by satellite remote sensing, NWP users' needs are expressed in a temporal and geographical coverage in terms of observation density per unit time and do not require instrument revisit at the exact location within a certain number of hours or days. Thus, any revisit required for WIVERN is not a requirement for exactly the same ground location. Also, there is no requirement for the satellite ground track to overfly a specific ground station as the global coverage ensures opportunities for vicarious calibration and validation.

MIS-81 Mean revisit time

The mean revisit time for a sample box of 20 X 20 km^2 at an altitude of 12km in the [-85º, -50°] and [50º, 85°] latitude bands shall be less than or equal to 1.1 days, and between [-50º,50] latitude shall be less than or equal to 1.6 days.

Note 1: *mean revisit refers to the longitude-averaged time-averaged values*
Note 2: *average in time shall be done at least over one orbit repeat cycle*

Justification : This is estimated to fulfil the NWP coverage needs.

MIS-99 Maximum revisit time

The maximum revisit time for a sample box of 20 X 20 km^2 at an altitude of 12km shall be globally less than or equal to 6 days.

Note 1: *maximum revisit refers to the longitude-maximum time-maximum values*

MIS-100 Swath sampling

The maximum closest distance between any random point within the swath and the cycloid track of the radar footprint shall be smaller than 20km.

Note: *This requirement drives the radar antenna rotation speed such that the sampling on ground within the swath is dense enough to ensure a sufficient number of wind measurements.*

MIS-109 Cycloidal track stability

The track of the radar footprint shall not deviate, at any point over the orbit, by more than 10km (TBC) with respect to the reference cycloid track.

Note 1: *the frozen orbit condition and no pointing errors shall be considered to compute the reference cycloid track.*

Justification : This requirement is introduced to control the ”wobble” of the radar footprint with respect to the reference and shall take into account both orbit and attitude control.

6.2.4.3. Orbit prediction and control accuracy

The ground track shall be predicted on a daily basis by the satellite Flight Observation Segment (FOS). The predictions will be used to plan correlated CAL/VAL observations, and possibly also for instrument calibration using auxiliary data (TBC).

MIS-59 Orbit prediction accuracy

The accuracy of the orbit prediction shall be $\pm$ TBC km in the across-track direction over a time period of TBC.

MIS-108 Orbit altitude control accuracy

The orbital altitude shall be controlled within a range of ± 5 km (TBC) with respect to the reference altitude at each latitude.

Note 1: *the frozen orbit condition shall be considered to compute the reference altitude at each latitude.*

Justification : The deadband on the altitude is needed to keep stable the instrument sensitivity as well as to limit the frequency of the orbit control manoeuvres (ideally to be on the order of one per month). Preferably, the orbit control manoeuvres should be done over regions ”empty” part of the Pacific.

6.2.4.4. Equatorial crossing time

The choice of the equatorial crossing time is crucial to the success of the WIVERN mission and involves many competing and at times incompatible criteria.
Concerning wind observations, the current lack of direct in-cloud wind observations globally means that sampling during any time of the day will be useful. The distribution of clouds is, however, not equal during the day, with more stratiform cloud distribution especially at lower layers during night and morning hours, and more convective clouds in the late morning until the late afternoon. For the observation of unambiguous winds within stratiform clouds, a dawn-dusk orbit would be preferred. For the capturing of cloud convection, an afternoon orbit (e.g.14:00h) may be preferred but at the penalty of potentially too strong attenuation of the radar signal inside of strongly convective clouds. Analysis of the GMI 166GHz channel suggests maximum ice cloud in the tropics occurs at ~ 04:00h over the ocean and 17:00h over land .

Concerning possible collocated observations with other relevant satellite missions in the 2030 timeframe, it is noted that the polar orbiting meteorological satellites such as MetOp-SG fly in the late morning and at around 800 km altitude, whereas aerosol and cloud missions fly typically in the afternoon (also usually between 700 and 800 km altitude). MetOp and the Ice Cloud Imager (ICI) fly at 09:30h, but the ICI channels are mostly above 90 GHz so it detects thin high cloud that may be undetectable by WIVERN. Also, the 30 km footprint is much larger than the 1km WIVERN footprint. Synergy with the Copernicus imaging microwave radiometer (CIMR) at a higher orbit with a large antenna operating up to 36.5 GHz for clouds and precipitation products, and for near-surface winds has been considered. The number of coincident looks is high, especially at higher latitudes, but the footprint size again is larger than the 1km WIVERN footprint.

The candidate Doppler Wind Lidars (DWL)/Aeolus-2 meteorological mission would fly at 18:00h LTAN. The clear air winds from DWL/Aeolus-2 complement the WIVERN in-cloud winds for improving NWPs. This orbit also has the advantage that it should minimise Thermo Elastic Deformation (TED) stresses on the WIVERN antenna and thus reduce any problems with pointing

accuracy degrading the precision of the WIVERN in-cloud winds. So, at present, this is the preferred compromise. It would be important for WIVERN to fly during a local time which maximizes product quality and at the same time fill gaps in current satellite wind coverage.

MIS-65 Local time of ascending node

The WIVERN local time of the ascending node (LTAN) shall be 18:00h.

Note: *Further studies of the optimum equator time are needed in the frame of SciReC, particularly to consider the combination of Aeolus-2 and WIVERN for the impact on NWP when compared with the timing of other satellites that are having a positive impact on NWP.*

6.2.5. Data latency

The WIVERN Level 2 data products are envisaged to be used in global operational NWP models. In the 2031 timeframe, NWP models, both on regional and global scale, will have the ability to continuously ingest observations independent of the observation cycles, which currently are typically 3 hours in global NWP. To enable operational NWP centres to assimilate the WIVERN data, it is crucial that the data be made available in near real time (i.e. <3 hours). Furthermore, this allows for fast feedback regarding data quality issues detected by the NWP centres who will be monitoring the radar performance by comparisons with NWP predicted values. Therefore, the measurements shall be made continuously. No special modes of operation are required for calibration.

MIS-103 End-to-end latency of L1 data

The end-to-end latency (from the time of sensing to the availability to users) of the Level 1 data shall be less than 150 min for 95% of the data products.

MIS-104 End-to-end latency of L2 data

The end-to-end latency (from the time of sensing to the availability to users) of the Level 2 data shall be less than 180 min for 95% of the data products.

MIS-71 Measurement duty cycle

The scientific measurements shall be made continuously.

Note: Temporary interruptions for external calibration and Orbit Control Manoeuvres / Collision Avoidance Manoeuvres are allowed as long as these are compliant with the availability requirement.

6.2.6. Length of observational dataset

The required mission lifetime shall be at least 5 years to provide measurements covering different seasons and inter-annual variability. A goal requirement is to operate WIVERN for 7 years,

which will allow for multi-year operational use in NWP. This will ensure partial coverage of at least one El Nino Southern Oscillation (ENSO) cycle. It will also provide experimental evidence of Doppler wind measurement capability of clouds and their utility for operational numerical weather prediction. In order to contribute to long-term cloud climate records, multi-annual observations are needed.

MIS-75 Mission lifetime

The WIVERN mission duration shall be at least 5 years (threshold) / 7 years (goal).

MIS-82 Mission extended lifetime

The satellite shall include consumables allowing a lifetime extension of at least an additional 5 years after the nominal operational lifetime.

6.2.7. Geolocation knowledge

The geolocation of the WIVERN Level 1 and Level 2 products (horizontally and vertically) shall be of a high accuracy to ensure correct use of the data in the intended scientific application and for CAL/VAL purposes. Also, an accuracy of 100 m ($\pm$50 m, TBC) in the vertical is expected to be needed, if the surface is used for monitoring the instrument LOS pointing.

MIS-79 Geolocation accuracy

The WIVERN measurement geolocation shall be known to better than • Horizontal: 250 m for the geolocation of the centre of the Level 1 measurements; and • Vertical: 50m for the geolocation of the centre of the Level 1 measurements.

Confidence Level : 1-sigma

6.3. Measurements (Level 1) Requirements

6.3.1. LoS Doppler velocity (Level 1B)

The LoS winds are corrected for the satellite velocity using on-board housekeeping data, including pointing and range correction of rotating antenna. Calibration with instrument external information (e.g. using EMCWF data) is done at Level 2A. The calibration techniques that can be implemented to reduce the mis-pointing errors are summarized in Table MSR-60.
These LoS winds are produced at 1km resolution and are intended for use in convective clouds where the values of Z are typically above 0dBZ (rather than the -15dBZ level specified for the LoS winds in the level 2B product). Below are the specifications given for 20km integration.

Table **MSR-60**: Calibration techniques for mis-pointing correction

Identifier	Name	Description
1	Re-tracking	Elevation 'altimeter processing' using re-tracking (ocean and maybe land): a 15 m error in sea surface height produces a look angle estimation error of less than 30 μrad (20 cm/s). Since coarse range estimation is required (few tens of meters) the ground return model can be simple, and no specific radar mode will be required.
2	Zero-Doppler returs	Zero doppler returns, especially for land and maybe for ocean, using corrections for waves and currents (Chapron et al., 2005).
3	Active transponder	Transponder based azimuth/elevation mis-pointing from received signal peak (elevation perhaps utilizing a stopped antenna at an along track position).
4	Full rotation signal Doppler signature	Azimuth calibration from expected Doppler return in full rotation not pre-compensating Doppler due to antenna rotation
5	Antenna thermistors	Calibration based on antenna backside thermistors using satellite house-keeping data
6	ECMWF model	Calibration based on ECMWF semi-real-time wind data. Including idea to compare ascending and descending tracks to compare the same winds at similar locations

MSR-14 Non-geophysical random error L1B LoS Doppler velocity

The non-geophysical contribution to the random error of the Level 1B LoS Doppler velocity shall be less than 1.9 m/s times the sine of the LoS incidence angle at one sigma, for an integration distance of 20km for a radar target averaging -15dBZ (Threshold) / -18dBZ (Breakthrough) / -21dBZ (Goal) assuming no atmospheric attenuation and assuming a dielectric factor $|K_w|^2$ for the radar targets of 0.75 (water at 10 °C at 94 GHz) (Tanelli et al., 2008).

Note 1: *industry is responsible for the flow down of the non-geophysical contribution to pointing and non-pointing contributions (e.g including the pulse-pair estimation error).*

Note 2*: this assumes that non-geophysical contributions to the random error are corrected with system-internal calibration techniques.*

Note 3*: pointing contributions with frequency content at satellite level higher than the split frequency of 1e-5Hz (i.e. corresponding to 1 day period) are to be considered as part of the random contribution.*

Note 4: *industry shall include the spectral broadening solely due to the platform motion as a parameter of the Doppler spectrum that affect the performance of mean velocity estimators at Level 1B. Spectral broadening due the spread of terminal fall velocities of hydrometeors of different size, broadening due to air turbulence and broadening due to wind shear shall be included at Level 2A as part of the geo-physical contribution.*

Satisfies : OBS-142

MSR-15 Non-geophysical systematic error L1B LoS Doppler velocity

The non-geophysical contribution to the systematic error of the Level 1B LoS Doppler velocity shall be less than 2.5 m/s times the sine of the LoS incidence angle for an integration distance of 20km.

Note 1: *industry is responsible for the flow down of the non-geophysical contribution to pointing and non-pointing contributions.*

Note 2: *this assumes that non-geophysical contributions to the systematic error are corrected with system-internal calibration techniques.*

Note 3: *pointing contributions with frequency content at satellite level lower than the split frequency of 1e-5Hz (i.e. corresponding to 1 day period) are to be considered as part of the systematic contribution.*

Confidence Level : 1-sigma

Satisfies : OBS-143

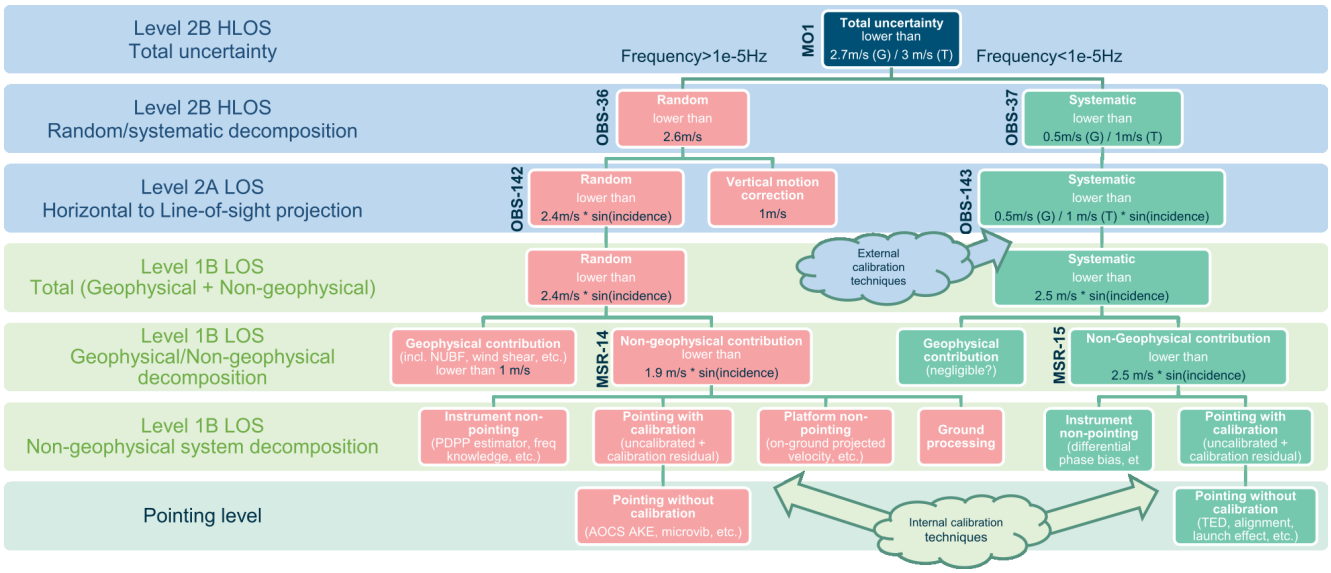

Figure **MSR-106**: HLoS Doppler wind velocity uncertainty error - requirements flow down chart.

6.3.2. Reflectivities (Level 1B)

The power of each transmitted H and V pulse shall be monitored and recorded.

MSR-42 Peak power accuracy

The power of each transmitted H and V pulse shall be monitored and recorded to an accuracy of 0.1dB (2.3%) (TBC).

MSR-6 Radar Sensitivity

The single-pulse detection threshold Za0dB shall be less than -15 dBZ with a 3 dB margin (TBC).

Note: *At level zero, the I and Q values shall be available from each pulse at each gate and the corrections applied to the LoS velocity via the pointing knowledge for the satellite velocity component.*

Satisfies : OBS-149

MSR-99 L1B Reflectivity random error

The random error of the reflectivity estimate at 1km integration shall be lower than 1.5dB (T) / 1.2dB (G) at 20dB SNR or greater.

Confidence Level : 1-sigma

Justification : Goal requirement is introduced to assess the possibility to improve the reflectivity precision by using frequency diversity and/or pulse compression. Number of pulses and peak power should be traded while keeping limited the impact on the system design and performance.

Satisfies : OBS-149

MSR-110 L1B Reflectivity systematic error

The systematic error of the reflectivity estimate without atmospheric contribution at 1km integration shall be lower than 0.5 dB.

6.3.3. Polarimetric variables (Level 1B)

Z_{DR}, Φ_{DP}, ρ_{HV} shall be calculated from the individual values of I and Q of the V and H channel. LDR shall be calculated if an LDR mode is implemented.x

6.3.4. Brightness temperature measurements (Level 1B)

CloudSat derives a brightness temperature T_b from the increase in the background receiver noise when the radar pulse is in the stratosphere, so, there is no radar return from hydrometeors. Any increase in noise is due to more upwelling radiation at 94 GHz from the surface and the atmosphere. The transmitted pulse is 3.3 μs (500 m) long, so, the amplifier has a bandwidth of 300 kHz. An alternative arrangement should be examined for WIVERN, whereby the front-end amplifier has a bandwidth of 100 MHz, equal to the protected bandwidth at 94 GHz.

The amplifier output is then digitised at 100MHz, and a subsequent digital filter separates the more slowly varying signal from the hydrometeor targets as they reshuffle in space, from the more rapidly varying noise.

The default specification for WIVERN is a radar footprint moving at 500 km/s, or 1km in 2ms, during which time it will obtain about 200,000 independent estimates of the noise. The background noise in the front-end amplifier is about 1000 K. So that implies that for every 1 km in the horizontal any changes in T_b could be estimated to within 2 K. T_b would be available at H and V polarisations.

Calibration of the T_b values on WIVERN using hot and cold reference targets would add complexity to the mission, but the requirement is to measure only changes in T_b relative to clear sky conditions. The extra emission associated with an increase in liquid cloud water leads to a

rise in T_b, whereas large ice particles scatter radiation that lead to a fall in T_b. ECMWF scientists are able to forward model values of T_b from the IFS analysis and can, for example, track operationally T_b calibration changes of about 1.5K from the Special Sensor Microwave Imager (SSMI) satellites (Bell et al. 2008) as they orbit and are confident to calibrate the observed T_b changes in WIVERN (Alan Geer, ECMWF, Pers.Comm.) to a similar accuracy.

Note: for the Doppler observations, the RF frequency of the Doppler returns will be modulated by the additional shift from the sinusoidally varying component of the satellite motion as the antenna rotates. Corrections must be made for this shift.

MSR-52 L1B NEDT

The radiometric resolution of the internally calibrated brightness temperature for both H and V polarizations shall be less than 1.5K (G) / 4K (T) along the footprint track of 1km in the horizontal direction.

Satisfies : OBS-154

MSR-53 L1B brightness temperature mid-term stability

The mid term bias stability of the brightness temperature at the input of the instrument after internal calibration shall be less than 1K for every 1000 km along the radar footprint track. The brightness temperature at the input of the instrument shall be derived from the output noise power measured by the instrument. The mid-term bias stability of the brightness temperature at the input of the instrument shall assume a uniform brightness temperature of the observed scene on the Earth leading to worst case stability estimation.

Justification : Long term stability is calibrated against ECMWF data at level 2.
Satisfies : OBS-154

MSR-107 TB94 (H&V), 3rd and 4th Stokes parameters of brightness temperature

The brightness temperature in H and V polarizations, as well as in the third and fourth Stokes parameters shall be measured.

6.3.5. Dynamic range (Level 1B)

MSR-101 L1B reflectivity dynamic range

The dynamic range of the Level 1B internally calibrated reflectivity product shall be at least 60 dB.

Satisfies : OBS-42

MSR-103 L1B LoS wind dynamic range

The dynamic range of the Level 1B internally calibrated LoS wind product product shall be at least from $-\lambda/4T_{HV}$ to $+\lambda/4T_{HV}$

Satisfies : OBS-43

MSR-102 L1B brightness temperature dynamic range

The dynamic range of the Level 1B internally calibrated brightness temperature product shall be from 40K and 340K.

Satisfies : OBS-44

6.3.6. RF Pulse frequency (Level 1B)

The pulse frequency shall be reported in the L1 product which is used to determine the LoS winds in the L1 and L2 products.

MSR-54 Doppler shift knowledge

The frequency of the Doppler shifted return pulse shall be known and recorded in the data products.

Note: *the knowledge error of the frequency of the Doppler shifted return pulse is a contribution to the random error of the LoS Doppler velocity (MSR-14).*

MSR-111 Center frequency knowledge

The center frequency of the transmitted pulse shall be known with an accuracy of TBD Hz.

6.3.7. Level 1A measurement requirements

No specific requirements are defined at Level 1A since the I&Q data are not processed further from L0. Geolocation and radiometric correction data are calculated for each image pixel without application. Instrument and platform housekeeping data as well as radiometric calibraton data shall be up-sampled to the PRF value whenever their sampling frequency is lower.

7. DATA PROCESSING

7.1. Level-0 to Level-1 Processing

Figure DAT-129 shows the successive processing steps to go from the I and Q radar time series to estimates of reflectivity, polarimetric variables, Doppler velocity, and relative changes of noise power.

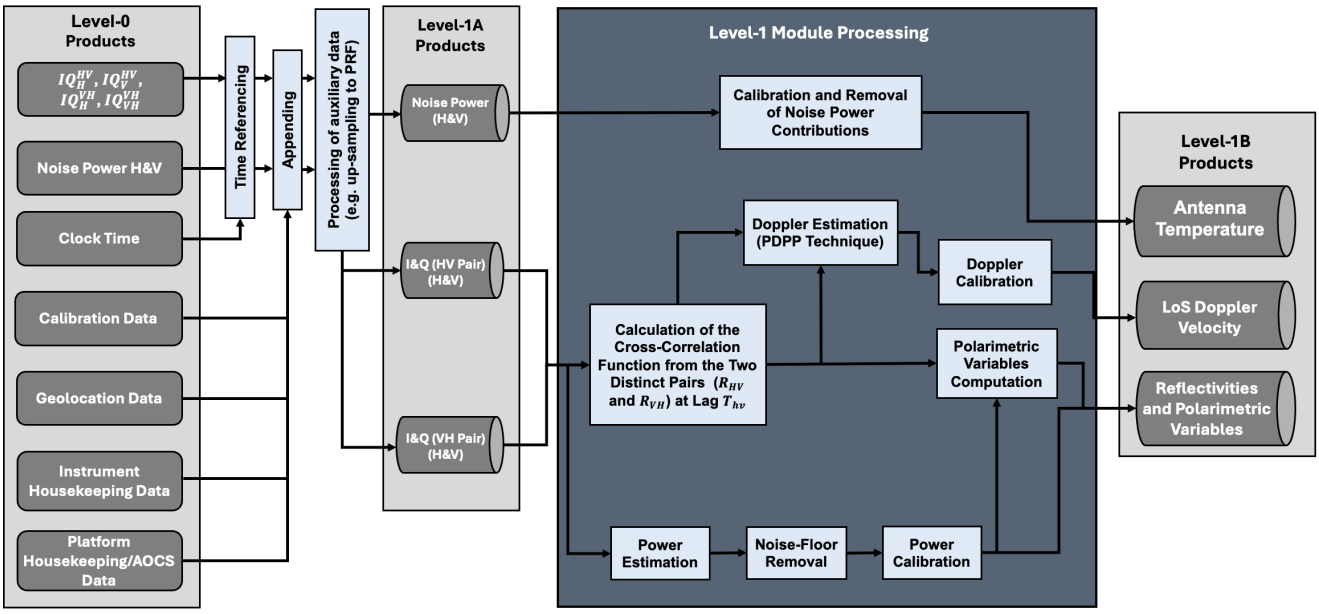

Figure **DAT-129**: Flowchart of Level-0 to Level-1 processing.

More details about the Level-0 to Level-1 processing can be found in Chapter 5 of [RD-54].

7.2. Level-1 to Level-2 Processing

Figure DAT-134 illustrates the sequential processing steps involved in extracting cloud and wind products from reflectivity, polarimetric variables, Doppler velocity, and relative changes in noise power. The following is a brief overview of these processing steps, with more explanations provided in Chapter 7 of the RfA.
The first step is to derive unbiased Level-1B products. This process involves:

- Calibrating winds with two methodologies:
  - Firstly, LoS velocities will be compared statistically with NWP forecasts (Scarsi et al., 2023). This is a common strategy. For example, the Aeolus mission has shown the value of comparisons of its Level-2B winds with those of the ECMWF operational model. The ECMWF global mean winds are accurate to better than 1 m/s, and have proved invaluable for identifying various subtle biases introduced by LoS mis-pointing

induced by temperature distortion in the mirror (Rennie et al., 2021). Mis-pointing of the boresight radar, due thermo-elastic distortion stress in the antenna might also introduce biases into the WIVERN wind field. So, a real time comparison of the mean winds in the operational NWP model could become essential in identifying and monitoring such biases.

  - Secondly, LoS velocity will be corrected from biases induced by reflectivity inhomogeneity combined with velocity shear (in particular the apparent wind shear across the backscattering volume which is due to the fast-moving satellite).

- Calibrating brightness temperatures by converting brightness temperatures using conversion coefficients. This will be calculated via radiative transfer computations applied to ECMWF profiles via a surface emissivity model and a gas attenuation model.
- Removing ghosts from reflectivities (Rizik et al., 2023), separating hydrometeor and clutter return and estimating auxiliary products like atmospheric gas attenuation profiles and path integrated attenuation (PIA) via the surface reference technique.

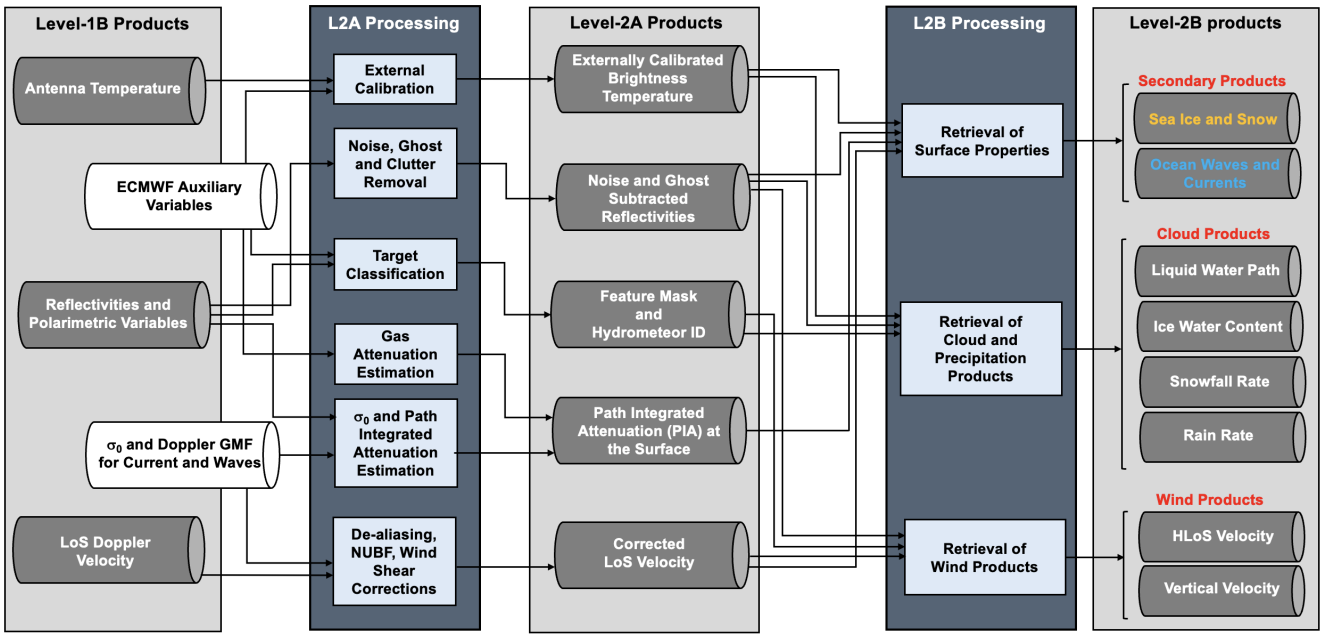

Figure **DAT-134**: Flowchart of Level-1 to Level-2 data processing chain.

The second step is to exploit the Level-2A products for retrieving geophysical parameters such as HLoS velocity, ice water content, rain/snow rate, liquid water path, and convective classification and vertical motion. At this stage, the processing chain splits into two categories for the cloud and wind products:

- The derivation of the HLoS velocity relies on the identification of convective and stratiform areas based on the variability of the LoS wind. If the cloud can be considered stratiform

(low LoS variability), the HLoS wind is obtained after estimating the Doppler terminal velocity of the hydrometeors according to the temperature and calibrated reflectivity.

- For the retrieval of IWC, rain/snow rate and liquid water path, depending on the type of hydrometeor sampled, specific retrievals are applied using radar-only or combined radar-radiometer observations. Some of these retrievals will be fairly straightforward (e.g., the IWC can be derived from calibrated reflectivity and temperature) while other will rely on more sophisticated techniques (rain rate retrieval will require an estimate of the reflectivity gradient or a dedicated artificial intelligence algorithm).

More details about the Level-1 to Level-2 processing can be found in Chapter 6 of [RD-54].

Requirements Index

The following index lists all requirements contained in the present document.

APPENDIX A. ACRONYMS AND ABBREVIATIONS

AD Applicable Documents.

ADC Analog to Digital Converter.

ADR Active Debris Removal.

AHL Active Hot Load.

AI Artificial Intelligence.

AIT Assembly Integration and Testing.

AIV Assembly, Integration and Verification.

AKE Absolute Knowledge Error.

AMSR2 Advanced Microwave Scanning Radiometer 2.

AMV Atmospheric Motion Vector.

AOC Attitude and Orbit Control.

AOCS Attitude and Orbit Control Subsystem.

AOS Atmosphere Observing System.

APE Absolute Pointing Error.

ARA Absolute Radiometric Accuracy.

ARC Active Radar Calibrator.

ARPEGE Action de Recherche Petite Echelle Grande Echelle.

ATBD Algorithm Theoretical Basis Document.

AWS Arctic Weather Satellite.

BCH Bose-Chaudhari-Hocquenghem.

BoL Beginning Of Life.

C/S Convective/Stratiform.

CAIRT Changing-Atmosphere Infra-Red Tomography Explorer.

CCSDS Consultative Committee for Space Data Systems.

CEU Central Electronics Unit.

CFAD Contour Frequency Altitude Display.

CFRP Carbon Fiber Reinforced Polymer.

CIMR Copernicus Imaging Microwave Radiometer.

COM Commissioning.

CPR Cloud Profiling Radar.

CRISTAL Copernicus polar Ice and Snow Topography ALtimeter.

CSC Copernicus Space Component.

CWP Cloud Water Path.

DA Data Assimilation.

DBE Digital Back End.

DCC Deep Convecive Cores.

DDV Design, Development & Verification.

DFS Doppler Frequency Shift.

DHS Data Handling Subsystem.

DPR Dual-frequency Precipitation Radar.

DWL Doppler Wind Lidar.

E2ES End-to-End Simulator.

EBB Elegant Bread Board.

EC European Commission.

ECEF Earth-Centered Earth-Fixed.

ECMWF European Centre for Medium-range Weather Forecasts.

EDA Ensemble of Data Assimilation.

EEE Electric, Electronic and Electromechanical.

EGSE Electrical Ground Support Equipment.

EIK Extended Interaction Klystron.

EM Engineering Model.

ENSO El Nino Southern Oscillation.

EO Earth Observation.

EPC Electronic Power Conditioner.

ESA European Space Agency.

ESCAPE "Experiment of Sea Breeze Convection, Aerosols, Precipitation, and Environment".

ESM Earth System Model.

ESOC European Space Operations Centre.

ESTEC European Space Research and Technology Centre.

FAR Flight Acceptance Review.

FDIR Fault Detection, Isolation, and Recovery.

FEM Finite Element Modelling.

FIFO First In, First Out.

FIR Finite Impulse Response.

FMECA Failure Mode, Effects, and Criticality Analysis.

FOC Flight Operations Center.

FOS Flight Operations Segment.

FOV Field of View.

FPGA Field Programmable Gate Array.

FSOI Forecast to Sensitivity Observations Impact.

FSS Fractions Skill Score.

GCM General Circulation Model.

GCOS Global Climate Observing System.

GEO Geostationary.

GMES Global Monitoring for Environment and Security.

GMF Geophysical Model Function.

GNSS Global Navigation Satellite System.

GOS Global Observing System.

GPM Global Precipitation Measuring mission.

GPP Gross Processor Prototype.

GS Ground Segment.

GSE Ground Support Equipment.

HDRM Hold-Down and Release Mechanisms.

HKTM HouseKeeping TeleMetry.

HLoS Horizontal Line of Sight.

HP Heat Pipe.

HPA High-Power Amplifier.

ICESat-2 Ice, Cloud, and Land Elevation Satellite-2.

ICI Ice Cloud Imager.

ICON Icosahedral Nonhydrostatic model.

IF Intermediate Frequency.

IFOV Instrument Field of View.

IFS Integrated Forecasting System.

INCUS Investigation of Convective Updrafts.

IOCR In-Orbit Commissioning Review.

IPCC Intergovernmental Panel on Climate Change.

IR InfraRed.

IRD Interface Requirements Document.

ISRR Intermediate System Requirements Review.

ITU International Telecommunications Union.

IWC Ice Water Content.

IWP Ice Water Path.

IWV Integrated Water Vapor.

LAR Launcher Adapter Ring.

LEO Low Earth Orbit.

LEOP Launch and Early Operations Phase.

LGO LEO to Ground - Optical.

LGOT LEO to Ground Optical Terminal.

LNA Low Noise Amplifier.

LOD Launch Offloading Device.

LoS Line of sight.

LPC Living Planet Challenge.

LWC Liquid Water Content.

LWP Liquid Water Path.

MAG Mission Advisory Group.

MATER Mission Assumptions and Technical Requirements (Document).

MCS Mesoscale Convective Systems.

MGSE Mechanical Ground Support Equipment.

MIL MIL-STD-1553 Serial Data Bus.

ML Machine Learning.

MLI Multi-Layer Insulation.

MRCP Mid Term Check Point.

MW MicroWave.

NEDT Noise-Equivalent ΔT_B.

NRCS Normalized Radar Cross Section.

NRMSE Normalised Root Mean Square Error.

NUBF Non Uniform Beam Filling.

NWP Numerical Weather Prediction.

OBC On-Board Computer.

OBCP On-Board Operation Control Procedures.

OBSW On-Board Software.

OCP Optical Communication Payload.

ODYSEA Ocean DYnamics and Surface Exchange with the Atmosphere.

OGSE Optical Ground Support Equipment.

OPS Operational Phase.

OSCAR Observing Systems Capability Analysis and Review Tool.

OSE Observing System Experiment.

OSSE Observing Simulated System Experiment.

OTS Off-the-Shelf.

PA Product Assurance.

PCDU Power Conditioning and Distribution Unit.

PCR Preliminary Concept Review.

PD Polarization Diversity.

PDF Probability Density Function.

PDGS Payload Data Ground Segment.

PDHT Payload Data Handling and Transmission.

PDPP Polarization Diversity Pulse Pair.

PFM Proto-Flight Model.

PIA Path Integrated Attenuation.

PMM Precipitation Measuring Mission.

PMP Parts, materials and processes.

PMR Precipitation Measuring Radar.

PP Pulse Pair.

PRF Pulse Repetition Frequency.

PRI Pulse Repetition Interval.

PRR Preliminary Requirement Review.

PSO Primary Science Objective.

QON Quasi-Optic Network.

RA Radio Astronomy.

RCE Radar Central Electronics.

RD Reference Document.

RF Radio Frequency.

RFC Radio Frequency Compatibility.

RFI Radio-Frequency Inteference.

RHI Range Height Indicator.

RICO Rain in Cumulus over the Ocean.

RID Review Item Disposition.

RMS Root Mean-Square.

ROM Rough Order of Magnitude.

RPM Revolutions Per Minute.

RR Rain Rate.

RWC Rain Water Content.

RWP Rain Water Path.

Rx Receive.

SAM System for Atmospheric Modeling.

SAR Synthethic Aperture Radar.

SC Spacecraft.

SCM Scan Mechanism.

SCR Signal to Clutter Ratio.

SD Standard Deviation.

SDM Space Debris Mitigation.

SEE Single Event Effect.

SEGR Single Event Gate Rupture.

SEL Single Event Latch-up.

SEU Single Event Upset.

SGR Signal to Ghost Ratio.

SIC Sea Ice Concentration.

SIE System Integrated Energy.

SIOV Satellite Initial In-Orbit Verification.

SLE Space Link Extension.

SM Structural Model.

SMRT Snow Microwave Radiative Transfer model.

SNR Signal to Noise Ratio.

SPF Single Point Failure.

SR Snow Rate.

SRL Scientific Readiness Level.

SSA Spatial Sampling Angle.

SSD Spatial Sampling Distance.

SSI Spectral Sampling Interval.

SSM Secondary-Surface Mirror.

SSMI Special Sensor Microware Imager.

SSO Secondary Science Objective.

SSP Sub Satellite Point.

SSRD Satellite System Requirements Document.

SST Sea Surface Temperature.

SSVT Satellite System Validation Test.

SV Satellite/Spacecraft Vehicle.

SVT System Validation Test.

SWB Scientific Work-Bench.

SWEEP WIVERN End-to-End Performance Simulator.

SZA Sun Zenith Angle.

T_b Brightness Temperature.

TB/TV Thermal Balance/Thermal Vacuum.

TBC To Be Confirmed (by the Agency).

TBD To Be Defined (by the Agency).

TBS To Be Specified (by the Agency).

TC Tropical Cyclone.

TCS Thermal Control Subsystem.

TED Thermo-Elastic Distortion.

TN Technical Note.

TRL Technological Readiness Level.

TRMM Tropical Rainfall Measuring Mission.

TSCV Total Surface Current Vector.

TT&C Telemetry, Tracking & Command.

TTC/TT&C Telemetry Tracking Command.

TVAC Thermal Vacuum.

Tx Transmit.

UCM User Consultation Meeting.

UPM Universal Processing Module.

UTC Coordinated Universal Time.

VEGA Vettore Europeo di Generazione Avanzata.

Vt Terminal Velocity.

WCRP World Climate Research Programme.

WIVERN Wind Velocity Radar Nephoscope.

WMO World Meteorological Organisation.

WP Work Package.

WRF Weather Research and Forecast.

WS Wind Shear.

Z Radar Reflectivity Factor.

APPENDIX B. WIVERN SCIENTIFIC BIBLIOGRAPHY

Alexander, S. P., Protat, A., Berne, A., and Ackermann, L.: Radar-Derived Snowfall Microphysical Properties at Davis, Antarctica, J. Geophys. Res. Atm., 128, e2022JD038 389, https://doi.org/https://doi.org/10.1029/2022JD038389, e2022JD038389 2022JD038389, 2023.

Bailey, H. and Hubbard, A.: Snow Mass Recharge of the Greenland Ice Sheet Fueled by Intense Atmospheric River, Geophysical Research Letters, 52, e2024GL110 121, https://doi.org/10/g9hjmb, 2025.

Baker, W. E., Atlas, R., Cardinali, C., Clement, A., Emmitt, G. D., Gentry, B. M., Hardesty, R. M., Källén, E., Kavaya, M. J., Langland, R., Ma, Z., Masutani, M., McCarty, W., Pierce, R. B., Pu, Z., Riishojgaard, L. P., Ryan, J., Tucker, S., Weissmann, M., and Yoe, J. G.: Lidar-Measured Wind Profiles: The Missing Link in the Global Observing System:, Bulletin of the American Meteorological Society, 95, 543 – 564, https://doi.org/10.1175/BAMS-D-12-00164.1, 2014.

Battaglia, A. and Panegrossi, G.: What Can We Learn from the CloudSat Radiometric Mode Observations of Snowfall over the Ice-Free Ocean?, Remote Sensing, 12, https://doi.org/10.3390/rs12203285, 2020.

Battaglia, A., Kollias, P., Dhillon, R., Roy, R., Tanelli, S., Lamer, K., Grecu, M., Lebsock, M., Watters, D., Mroz, K., Heymsfield, G., Li, L., and Furukawa, K.: Spaceborne Cloud and Precipitation Radars: Status, Challenges, and Ways Forward, Reviews of Geophysics, 58, https://doi.org/10.1029/2019RG000686, 2020.

Battaglia, A., Martire, P., Caubet, E., Phalippou, L., Stesina, F., Kollias, P., and Illingworth, A.: Observation error analysis for the WInd VElocity Radar Nephoscope W-band Doppler conically scanning spaceborne radar via end-to-end simulations, Atmospheric Measurement Techniques, 15, https://doi.org/10.5194/amt-15-3011-2022, 2022.

Bennartz, R., Fell, F., Pettersen, C., Shupe, M. D., and Schuettemeyer, D.: Spatial and temporal variability of snowfall over Greenland from CloudSat observations, Atmospheric Chemistry and Physics, 19, 8101–8121, https://doi.org/10.5194/acp-19-8101-2019, 2019.

Birner, T., Dörnbrack, A., and Schumann, U.: How sharp is the tropopause at midlatitudes?, Geophysical Research Letters, 33, https://doi.org/10.1029/2005GL025099, 2006.

Bischoff, T. and Schneider, T.: The Equatorial Energy Balance, ITCZ Position, and Double-ITCZ Bifurcations, Journal of Climate, 29, 2997 – 3013, https://doi.org/10.1175/JCLI-D-15-0328.1, 2016.

Boening, C., Lebsock, M., Landerer, F., and Stephens, G.: Snowfall-driven mass change on the

East Antarctic ice sheet, Geophysical Research Letters, 39, https://doi.org/https://doi.org/10.1029/2012GL053316, 2012.

Bony, S. and Stevens, B.: Measuring Area-Averaged Vertical Motions with Dropsondes, Journal of the Atmospheric Sciences, 76, 767 – 783, https://doi.org/10.1175/JAS-D-18-0141.1, 2019.

Bony, S., Dufresne, J.-L., and Le Treut, H.: Tropical cloud response to climate change: a critical review of the science, Nature Geoscience, 9, 767–776, https://doi.org/10.1038/ngeo2825, 2016.

Bony, S., Schulz, H., Vial, J., and Stevens, B.: Sugar, Gravel, Fish, and Flowers: Dependence of Mesoscale Patterns of Trade-Wind Clouds on Environmental Conditions, Geophysical Research Letters, 47, e2019GL085 988, https://doi.org/https://doi.org/10.1029/2019GL085988, e2019GL085988 10.1029/2019GL085988, 2020.

Bormann, N., Fouilloux, A., and Dragani, R.: Evaluation of satellite infrared and microwave sounder bias correction changes, Quarterly Journal of the Royal Meteorological Society, 145, 292–304, https://doi.org/10.1002/qj.3380, 2019.

Boukabara, S.-A., Jones, E., Geer, A., Kazumori, M., Garrett, K., and Maddy, E.: Assimilation of Precipitation Observations from Space into Numerical Weather Prediction (NWP), in: Satellite Precipitation Measurement: Volume 2, edited by Levizzani, V., Kidd, C., Kirschbaum, D. B., Kummerow, C. D., Nakamura, K., and Turk, F. J., pp. 941–982, Springer International Publishing, Cham, https://doi.org/10.1007/978-3-030-35798-6_24, 2020.

Bouyssel, F., Berre, L., Bénichou, H., Chambon, P., Girardot, N., Guidard, V., Loo, C., Mahfouf, J.-F., Moll, P., Payan, C., and Raspaud, D.: The 2020 Global Operational NWP Data Assimilation System at Météo-France, pp. 645–664, Springer International Publishing, Cham, https://doi.org/10.1007/978-3-030-77722-7_25, 2022.

Byrne, M. P. and Schneider, T.: Energetic Constraints on the Width of the Intertropical Convergence Zone, Journal of Climate, 29, 4709 – 4721, https://doi.org/10.1175/JCLI-D-15-0767.1, 2016.

Camplani, A., Sanò, P., Casella, D., Panegrossi, G., and Battaglia, A.: Arctic Weather Satellite Sensitivity to Supercooled Liquid Water in Snowfall Conditions, Remote Sensing, 16, https://doi.org/10.3390/rs16224164, 2024.

Cardinali, C.: Monitoring the observation impact on the short-range forecast, Quarterly Journal of the Royal Meteorological Society, 135, https://doi.org/10.1002/qj.366, 2009.

Caumont, O., Ducroq, V., Wattrelot, E., Jaubert, G., and Pradier-Vabre, S.: 1D+3DVar assimilation of radar reflectivity data: a proof of concept, Tellus A, 62, 173–187, https://doi.org/https://doi.org/10.1111/j.1600-0870.2009.00430.x, 2010.

Centurioni, L. R., Turton, J., Lumpkin, R., Braasch, L., Brassington, G., Chao, Y., Charpen-

tier, E., Chen, Z., Corlett, G., Dohan, K., Donlon, C., Gallage, C., Hormann, V., Ignatov, A., Ingleby, B., Jensen, R., Kelly-Gerreyn, B. A., Koszalka, I. M., Lin, X., Lindstrom, E., Maximenko, N., Merchant, C. J., Minnett, P., O'Carroll, A., Paluszkiewicz, T., Poli, P., Poulain, P.-M., Reverdin, G., Sun, X., Swail, V., Thurston, S., Wu, L., Yu, L., Wang, B., and Zhang, D.: Global in situ Observations of Essential Climate and Ocean Variables at the Air–Sea Interface, Frontiers in Marine Science, 6, https://doi.org/10.3389/fmars.2019.00419, 2019.

Chambon, P., Mahfouf, J. F., Audouin, O., Birman, C., Fourrié, N., Loo, C., Martet, M., Moll, P., Payan, C., Pourret, V., and Raspaud, D.: Global Observing System Experiments within the Météo-France 4D-Var Data Assimilation System, Monthly Weather Review, 151, https://doi.org/10.1175/MWR-D-22-0087.1, 2023.

Chapron, B., Collard, F., and Ardhuin, F.: Direct measurements of ocean surface velocity from space: Interpretation and validation, Journal of Geophysical Research: Oceans, 110, https://doi.org/10.1029/2004JC002809, 2005.

Coniglio, M. C., Stensrud, D. J., and Wicker, L. J.: Effects of upper-level shear on the structure and maintenance of strong quasi-linear mesoscale convective systems, Journal of the Atmospheric Sciences, 63, 1231–1252, https://doi.org/10.1175/JAS3681.1, 2006.

Copernicus Climate Change Service (C3S): Copernicus: 2024 is the first year to exceed 1.5°C above pre-industrial level, https://climate.copernicus.eu/copernicus-2024-first-year-exceed-15degc-above-pre-industrial-level, published: 2025-01-10, Accessed: 2025-05-12, 2025.

Coronel, B., Ricard, D., Rivière, G., and Arbogast, P.: Role of Moist Processes in the Tracks of Idealized Midlatitude Surface Cyclones, Journal of the Atmospheric Sciences, 72, 2979 – 2996, https://doi.org/10.1175/JAS-D-14-0337.1, 2015.

Czaja, A. and Marshall, J.: The Partitioning of Poleward Heat Transport between the Atmosphere and Ocean, Journal of the Atmospheric Sciences, 63, 1498 – 1511, https://doi.org/10.1175/JAS3695.1, 2006.

Dai, A., Luo, D., Song, M., and Liu, J.: Arctic amplification is caused by sea-ice loss under increasing CO2, Nature Communications, 10, https://doi.org/10.1038/s41467-018-07954-9, 2019.

Davison, B. J., Hogg, A. E., Rigby, R., Veldhuijsen, S., van Wessem, J. M., van den Broeke, M. R., Holland, P. R., Selley, H. L., and Dutrieux, P.: Sea Level Rise from West Antarctic Mass Loss Significantly Modified by Large Snowfall Anomalies, Nature Communications, 14, 1479, https://doi.org/10/grx8rc, 2023.

Demol, M., Ponte, A. L., Garreau, P., Piollé, J.-F., Ubelmann, C., and Rascle, N.: Diagnosis of Ocean Near-Surface Horizontal Momentum Balance from pre-SWOT altimetric data,

drifter trajectories, and wind reanalysis, ESS Open Archive, https://doi.org/10.22541/essoar.173687380.01053119/v1, 2025.

Donlon, C. J., Cullen, R., Giulicchi, L., Vuilleumier, P., Francis, C. R., Kuschnerus, M., Simpson, W., Bouridah, A., Caleno, M., Bertoni, R., Rancaño, J., Pourier, E., Hyslop, A., Mulcahy, J., Knockaert, R., Hunter, C., Webb, A., Fornari, M., Vaze, P., Brown, S., Willis, J., Desai, S., Desjonqueres, J.-D., Scharroo, R., Martin-Puig, C., Leuliette, E., Egido, A., Smith, W. H., Bonnefond, P., Le Gac, S., Picot, N., and Tavernier, G.: The Copernicus Sentinel-6 mission: Enhanced continuity of satellite sea level measurements from space, Remote Sensing of Environment, 258, 112 395, https://doi.org/10.1016/j.rse.2021.112395, 2021.

Duncan, D. I., Bormann, N., and Hólm, E. V.: On the addition of microwave sounders and numerical weather prediction skill, Quarterly Journal of the Royal Meteorological Society, 147, https://doi.org/10.1002/qj.4149, 2021.

Eby, G. N.: Atmosphere III, https://faculty.uml.edu/nelson_eby/87.202/Lectures/Atmosphere%20III.pdf, lecture notes, University of Massachusetts Lowell, 2010.

ECMWF: Artificial Intelligence Forecasting System (AIFS), https://www.ecmwf.int/en/about/media-centre/news/2024/aifs-ai-based-forecasting-system-ready-testing, 2024.

Elsaesser, G., Tselioudis, A. R. H. W. H. G., He, P. C. W., and Zelinka, M. D.: The role of deep convective clouds in climate change: Insights from observations and models, Nature Communications, 8, 1–10, https://doi.org/10.1038/s41467-017-01418-x, 2017.

Emanuel, K., Wing, A. A., and Vincent, E. M.: Radiative-convective instability, Journal of Advances in Modeling Earth Systems, 6, 75–90, https://doi.org/https://doi.org/10.1002/2013MS000270, 2014.

ESA: Living Planet Programme: Scientific Achievements and Future Challenges – Scientific Context of the Earth Observation Science Strategy for ESA, Tech. Rep. ESA SP-1329/2, European Space Agency, [ESA EO Scienece Strategy, 2015], 2015.

Eyre, J.: Observation impact metrics in NWP: A theoretical study. Part I: Optimal systems, Quarterly Journal of the Royal Meteorological Society, 147, 3180–3200, 2021.

Fan, J., Han, B., Varble, A., Morrison, H., North, K., Kollias, P., Chen, B., Dong, X., Giangrande, S. E., Khain, A., Lin, Y., Mansell, E., Milbrandt, J. A., Stenz, R., Thompson, G., and Wang, Y.: Cloud-resolving model intercomparison of an MC3E squall line case: Part I—Convective updrafts, Journal of Geophysical Research: Atmospheres, 122, 9351–9378, https://doi.org/https://doi.org/10.1002/2017JD026622, 2017.

Fiddes, S. L., Protat, A., Mallet, M. D., Alexander, S. P., and Woodhouse, M. T.: Southern Ocean Cloud and Shortwave Radiation Biases in a Nudged Climate Model Simulation:

Does the Model Ever Get It Right?, Atmospheric Chemistry and Physics, 22, 14 603–14 630, https://doi.org/10/g9fh28, 2022.

Fiedler, S., Crueger, T., D'Agostino, R., Peters, K., Becker, T., Leutwyler, D., Paccini, L., Burdanowitz, J., Buehler, S. A., Cortes, A. U., Dauhut, T., Dommenget, D., Fraedrich, K., Jungandreas, L., Maher, N., Naumann, A. K., Rugenstein, M., Sakradzija, M., Schmidt, H., and Stevens, B.: Simulated tropical precipitation assessed across three major phases of the coupled model intercomparison project (CMIP), Monthly Weather Review, 148, https://doi.org/10.1175/MWRD-19-0404.1, 2020.

Field, P. R. and Heymsfield, A. J.: Importance of snow to global precipitation, Geophysical Research Letters, 42, 9512–9520, https://doi.org/https://doi.org/10.1002/2015GL065497, 2015.

Fu, L.-L. and Cazenave, A.: Satellite altimetry and earth sciences: a handbook of techniques and applications, Academic Press, 2001.

Fu, L.-L., Pavelsky, T., Cretaux, J.-F., Morrow, R., Farrar, J. T., Vaze, P., Sengenes, P., Vinogradova-Shiffer, N., Sylvestre-Baron, A., Picot, N., and Dibarboure, G.: The Surface Water and Ocean Topography Mission: A Breakthrough in Radar Remote Sensing of the Ocean and Land Surface Water, Geophysical Research Letters, 51, e2023GL107 652, https://doi.org/https://doi.org/10.1029/2023GL107652, e2023GL107652 2023GL107652, 2024.

Galarneau, T. J., Zeng, X., Dixon, R. D., Ouyed, A., Su, H., and Cui, W.: Tropical mesoscale convective system formation environments, Atmospheric Science Letters, 24, https://doi.org/https://doi.org/10.1002/asl.1152, 2023.

Gasparini, R. et al.: The role of cloud radiative processes and latent heating in the evolution of anvil clouds: insights from idealized simulations, Journal of Climate, 32, 7129–7150, https://doi.org/10.1175/JCLI-D-19-0201.1, 2019.

Geer, A. J.: Physical characteristics of frozen hydrometeors inferred with parameter estimation, Atmospheric Measurement Techniques, 14, 5369–5395, https://doi.org/10.5194/amt-14-5369-2021, 2021.

Geer, A. J., Baordo, F., Bormann, N., Chambon, P., English, S. J., Kazumori, M., Lawrence, H., Lean, P., Lonitza, K., and Lupu, C.: The growing impact of satellite observations sensitive to humidity, cloud and precipitation, Quarterly Journal of the Royal Meteorological Society, 143, https://doi.org/10.1002/qj.3172, 2017.

Geer, A. J., Lonitz, K., Weston, P., Kazumori, M., Okamoto, K., Zhu, Y., Liu, E. H., Collard, A., Bell, W., Migliorini, S., Chambon, P., Fourrié, N., Kim, M.-J., Köpken-Watts, C., and Schraff, C.: All-sky satellite data assimilation at operational weather forecasting centres, Quarterly Journal of the Royal Meteorological Society, 144, 1191–1217, https://doi.org/https://doi.org/10.1002/qj.3202, 2018.

Gettelman, A., Salby, M. L., and Sassi, F.: Distribution and influence of convection in the tropical tropopause region, Journal of Geophysical Research: Atmospheres, 107, ACL 6–1–ACL 6–12, https://doi.org/https://doi.org/10.1029/2001JD001048, 2002.

Greenwald, T., Marchand, T. A., and Zelinka, M. D.: Cloud radiative feedbacks and their dependence on cloud type and region, Journal of Climate, 31, 9845–9865, https://doi.org/10.1175/JCLI-D-18-0114.1, 2018.

Griesche, H. J., Ohneiser, K., Seifert, P., Radenz, M., Engelmann, R., and Ansmann, A.: Contrasting ice formation in Arctic clouds: surface-coupled vs. surface-decoupled clouds, Atmospheric Chemistry and Physics, 21, 10 357–10 374, https://doi.org/10.5194/acp-21-10357-2021, 2021.

Guerreiro, K., Fleury, S., Zakharova, E., Rémy, F., and Kouraev, A.: Potential for estimation of snow depth on Arctic sea ice from CryoSat-2 and SARAL/AltiKa missions, Remote Sens. Env., 186, 339–349, https://doi.org/10.1016/j.rse.2016.07.013, 2016.

Hall, A.: The Role of Surface Albedo Feedback in Climate, Journal of Climate, 17, 1550 – 1568, https://doi.org/10.1175/1520-0442(2004)017<1550:TROSAF>2.0.CO;2, 2004.

Hartmann, D. L. and Michelsen, M. L.: NO EVIDENCE FOR IRIS, Bulletin of the American Meteorological Society, 83, 249 – 254, https://doi.org/10.1175/1520-0477(2002)083<0249:NEFI>2.3.CO;2, 2002.

Haualand, K. and Spengler, T.: Tropopause sharpness and baroclinic development, Weather and Climate Dynamics, 2, 97–114, https://doi.org/10.5194/wcd-2-97-2021, 2021.

Hayden, L. and Liu, C.: A multiyear analysis of global precipitation combining CloudSat and GPM precipitation retrievals, Journal of Hydrometeorology, 19, https://doi.org/10.1175/JHM-D-18-0053.1, 2018.

Heitmann, K., Sprenger, M., Binder, H., Wernli, H., and Joos, H.: Warm conveyor belt characteristics and impacts along the life cycle of extratropical cyclones: case studies and climatological analysis based on ERA5, Weather and Climate Dynamics, 5, 537–557, https://doi.org/10.5194/wcd-5-537-2024, 2024.

Heymsfield, A. J., Krämer, M., Luebke, A., Brown, P., Cziczo, D. J., Franklin, C., Lawson, P., Lohmann, U., McFarquhar, G., Ulanowski, Z., and Tricht, K. V.: Cirrus Clouds, Meteorological Monographs, 58, 2.1 – 2.26, https://doi.org/10.1175/AMSMONOGRAPHS-D-16-0010.1, 2017.

Hogan, R. J. and Illingworth, A. J.: The Retrieval of Ice Water Content from Radar Reflectivity Factor and Temperature and Its Use in Evaluating a Mesoscale Model, Journal of Applied Meteorology and Climatology, 45, 301–317, https://doi.org/10.1175/JAM2340.1, 2006.

Hohenegger, C. and Stevens, B.: Preconditioning Deep Convection with Cumulus Congestus,

Journal of the Atmospheric Sciences, 70, 448 – 464, https://doi.org/10.1175/JAS-D-12-089.1, 2013.

Hohenegger, C., Korn, P., Linardakis, L., Redler, R., Schnur, R., Adamidis, P., Bao, J., Bastin, S., Behravesh, M., Bergemann, M., Biercamp, J., Bockelmann, H., Brokopf, R., Brüggemann, N., Casaroli, L., Chegini, F., Datseris, G., Esch, M., George, G., Giorgetta, M., Gutjahr, O., Haak, H., Hanke, M., Ilyina, T., Jahns, T., Jungclaus, J., Kern, M., Klocke, D., Kluft, L., Kölling, T., Kornblueh, L., Kosukhin, S., Kroll, C., Lee, J., Mauritsen, T., Mehlmann, C., Mieslinger, T., Naumann, A. K., Paccini, L., Peinado, A., Praturi, D. S., Putrasahan, D., Rast, S., Riddick, T., Roeber, N., Schmidt, H., Schulzweida, U., Schütte, F., Segura, H., Shevchenko, R., Singh, V., Specht, M., Stephan, C. C., von Storch, J.-S., Vogel, R., Wengel, C., Winkler, M., Ziemen, F., Marotzke, J., and Stevens, B.: ICON-Sapphire: simulating the components of the Earth system and their interactions at kilometer and subkilometer scales, Geosci. Model Dev., 16, 779–811, https://doi.org/10.5194/gmd-16-779-2023, 2023.

Horányi, A., Cardinali, C., Rennie, M., and Isaksen, L.: The assimilation of horizontal line-of-sight wind information into the ECMWF data assimilation and forecasting system. Part I: The assessment of wind impact, Quarterly Journal of the Royal Meteorological Society, 141, https://doi.org/10.1002/qj.2430, 2015.

Houchi, K., Stoffelen, A., Marseille, G. J., and De Kloe, J.: Comparison of wind and wind shear climatologies derived from high-resolution radiosondes and the ECMWF model, Journal of Geophysical Research Atmospheres, 115, https://doi.org/10.1029/2009JD013196, 2010.

Houze, R.: Mesoscale convective systems, Reviews of Geophysics, 42, https://doi.org/10.1029/2004RG000150, 2004.

Houze, R. A.: Clouds in Tropical Cyclones, Monthly Weather Review, 138, 293 – 344, https://doi.org/10.1175/2009MWR2989.1, 2010.

Huffman, G. J., Bolvin, D. T., Braithwaite, D., Hsu, K. L., Joyce, R. J., Kidd, C., Nelkin, E. J., Sorooshian, S., Stocker, E. F., Tan, J., Wolff, D. B., and Xie, P.: Integrated Multi-satellite Retrievals for the Global Precipitation Measurement (GPM) Mission (IMERG), in: Satellite Precipitation Measurement: Volume 1, edited by Levizzani, V., Kidd, C., Kirschbaum, D. B., Kummerow, C. D., Nakamura, K., and Turk, F. J., pp. 343–353, Springer International Publishing, Cham, https://doi.org/10.1007/978-3-030-24568-9_19, 2020.

Ikuta, Y., Okamoto, K., and Kubota, T.: One-dimensional maximum-likelihood estimation for spaceborne precipitation radar data assimilation, Quarterly Journal of the Royal Meteorological Society, 147, https://doi.org/10.1002/qj.3950, 2021a.

Ikuta, Y., Satoh, M., Sawada, M., Kusabiraki, H., and Kubota, T.: Improvement of the Cloud Microphysics Scheme of the Mesoscale Model at the Japan Meteorological Agency Using Spaceborne Radar and Microwave Imager of the Global Precipitation Measurement as Refer-

ence, Monthly Weather Review, 149, 3803 – 3819, https://doi.org/10.1175/MWR-D-21-0066.1, 2021b.

Illingworth, A. J., Battaglia, A., Bradford, J., Forsythe, M., Joe, P., Kollias, P., Lean, K., Lori, M., Mahfouf, J.-F., Melo, S., Midthassel, R., Munro, Y., Nicol, J., Potthast, R., Rennie, M., Stein, T. H. M., Tanelli, S., Tridon, F., Walden, C. J., and Wolde, M.: WIVERN: A New Satellite Concept to Provide Global In-Cloud Winds, Precipitation, and Cloud Properties, Bulletin of the American Meteorological Society, 99, 1669–1687, https://doi.org/10.1175/BAMS-D-16-0047.1, 2018.

Intergovernmental Panel on Climate Change (IPCC): Climate Change 2021: The Physical Science Basis, URL https://www.ipcc.ch/report/ar6/wg1/, accessed: 2025-03-09, 2021.

Janisková, M. and Fielding, M. D.: Direct 4D-Var assimilation of space-borne cloud radar and lidar observations. Part II: Impact on analysis and subsequent forecast, Quarterly Journal of the Royal Meteorological Society, 146, https://doi.org/10.1002/qj.3879, 2020.

Jiang, X., Adames, A. F., Kim, D., Maloney, E. D., Lin, H., Kim, H., Zhang, C., DeMott, C. A., and Klingaman, N. P.: Fifty Years of Research on the Madden-Julian Oscillation: Recent Progress, Challenges, and Perspectives, Journal of Geophysical Research: Atmospheres, 125, e2019JD030 911, https://doi.org/https://doi.org/10.1029/2019JD030911, 2020.

Johnson, R. H., Rickenbach, T. M., Rutledge, S. A., Ciesielski, P. E., and Schubert, W. H.: Trimodal Characteristics of Tropical Convection, Journal of Climate, 12, 2397 – 2418, https://doi.org/10.1175/1520-0442(1999)012<2397:TCOTC>2.0.CO;2, 1999.

Kacimi, S. and Kwok, R.: Arctic Snow Depth, Ice Thickness, and Volume From ICESat-2 and CryoSat-2: 2018–2021, Geophys. Res. Lett., 49, https://doi.org/10.1029/2021gl097448, 2022.

Kazil, J., Narenpitak, P., Yamaguchi, T., and Feingold, G.: On Climate Change and Trade Cumulus Organization, Journal of Advances in Modeling Earth Systems, 16, e2023MS004 057, https://doi.org/https://doi.org/10.1029/2023MS004057, e2023MS004057 2023MS004057, 2024.

Kidd, C., Huffman, G., Maggioni, V., Chambon, P., and Oki, R.: The global satellite precipitation constellation current status and future requirements, Bulletin of the American Meteorological Society, 102, https://doi.org/10.1175/BAMS-D-20-0299.1, 2021.

Kossin, J. P.: A global slowdown of tropical-cyclone translation speed, Nature, 558, 104–107, https://doi.org/10.1038/s41586-018-0158-3, 2018.

Kotsuki, S., Sato, Y., and Miyoshi, T.: Data Assimilation for Climate Research: Model Parameter Estimation of Large-Scale Condensation Scheme, Journal of Geophysical Research: Atmospheres, 125, https://doi.org/10.1029/2019JD031304, 2020.

Kubar, T. L. and Waliser, D. E.: Cloud albedo variability and feedbacks in satellite observations and climate models, Journal of Geophysical Research: Atmospheres, 124, 8776–8790, https://doi.org/10.1029/2019JD030321, 2019.

Kulie, M. S. and Milani, L.: Seasonal variability of shallow cumuliform snowfall: A CloudSat perspective, Quarterly Journal of the Royal Meteorological Society, 144, 329–343, https://doi.org/https://doi.org/10.1002/qj.3222, 2018.

Kulie, M. S., Milani, L., Wood, N. B., and L'Ecuyer, T. S.: Global Snowfall Detection and Measurement, in: Satellite Precipitation Measurement: Volume 2, edited by Levizzani, V., Kidd, C., Kirschbaum, D. B., Kummerow, C. D., Nakamura, K., and Turk, F. J., pp. 699–716, Springer International Publishing, Cham, https://doi.org/10.1007/978-3-030-35798-6_12, 2020.

Lean, K., Bormann, N., and Healy, S.: Task 1.1 Evaluation of initial future EPS-Sterna constellations with 50 and 183 GHz, EUMETSAT Contract Report, 2023.

Li, H., Möhler, O., Petäjä, T., and Moisseev, D.: Two-year statistics of columnar-ice production in stratiform clouds over Hyytiälä, Finland: environmental conditions and the relevance to secondary ice production, Atmos. Chem. Phys., 21, 14 671–14 686, https://doi.org/10.5194/acp-21-14671-2021, 2021.

Lindzen, R. S., Chou, M.-D., and Hou, A. Y.: Does the Earth Have an Adaptive Infrared Iris?, Bulletin of the American Meteorological Society, 82, 417–432, https://doi.org/10.1175/1520-0477(2001)082<0417:DTEHAA>2.3.CO;2, 2001.

Liu, C., Zipser, E. J., Cecil, D. J., Nesbitt, S. W., and Sherwood, S.: A Cloud and Precipitation Feature Database from Nine Years of TRMM Observations, Journal of Applied Meteorology and Climatology, 47, 2712–2728, 2008.

Lopez-Cantu, T., Prein, A. F., and Samaras, C.: Uncertainties in Future U.S. Extreme Precipitation From Downscaled Climate Projections, Geophysical Research Letters, 47, e2019GL086 797, https://doi.org/https://doi.org/10.1029/2019GL086797, e2019GL086797 10.1029/2019GL086797, 2020.

Maahn, M., Burgard, C., Crewell, S., Gorodetskaya, I. V., Kneifel, S., Lhermitte, S., Van Tricht, K., and van Lipzig, N. P. M.: How does the spaceborne radar blind zone affect derived surface snowfall statistics in polar regions?, Journal of Geophysical Research: Atmospheres, 119, 13,604–13,620, https://doi.org/10.1002/2014JD022079, 2014.

Marseille, B. et al.: Historical overview of the impact of Aeolus wind data on operational weather forecasting models, Journal of Atmospheric Science and Technology, 33, 205–220, https://doi.org/10.1002/jats.4573, 2023.

Martin, G. et al.: Assessing the contribution of Aeolus wind observations to ECMWF sea sur-

face wind forecasts, Quarterly Journal of the Royal Meteorological Society, 149, 301–319, https://doi.org/10.1002/qj.4567, 2023.

Mason, S. L., Hogan, R. J., Bozzo, A., and Pounder, N. L.: A unified synergistic retrieval of clouds, aerosols, and precipitation from EarthCARE: the ACM-CAP product, Atmospheric Measurement Techniques, 16, 3459–3486, https://doi.org/10.5194/amt-16-3459-2023, 2023.

Massom, R. A., Fraser, A. B., and Lieser, K.: Snow on Antarctic Sea Ice, Reviews of Geophysics, 39, 413–445, https://doi.org/10.1029/2000RG000085, 2001.

Matrosov, S. Y., Shupe, M. D., and Uttal, T.: High temporal resolution estimates of Arctic snowfall rates emphasizing gauge and radar-based retrievals from the MOSAiC expedition, Elementa: Science of the Anthropocene, 10, 00 101, https://doi.org/10.1525/elementa.2021.00101, 2022.

McCoy, I. L., McCoy, D. T., Wood, R., Zuidema, P., and Bender, F. A.-M.: The Role of Mesoscale Cloud Morphology in the Shortwave Cloud Feedback, Geophysical Research Letters, 50, e2022GL101 042, https://doi.org/https://doi.org/10.1029/2022GL101042, e2022GL101042 2022GL101042, 2023.

McKim, B., Bony, S., and Dufresne, J.-L.: Weak anvil cloud area feedback suggested by physical and observational constraints, Nature Geoscience, 17, 392–397, https://doi.org/10.1038/s41561-024-01414-4, 2024.

McNally, T., Lessig, C., Lean, P., Chantry, M., Alexe, M., and Lang, S.: Red sky at night... producing weather forecasts directly from observations, https://doi.org/10.21957/tmc81jo4c7, 2024.

Milani, L. and Kidd, C.: The State of Precipitation Measurements at Mid-to-High Latitudes, Atmosphere, 14, https://doi.org/10.3390/atmos14111677, 2023.

Milani, L., Kulie, M. S., Casella, D., Dietrich, S., L'Ecuyer, T. S., Panegrossi, G., Porcù, F., Sanò, P., and Wood, N. B.: CloudSat snowfall estimates over Antarctica and the Southern Ocean: An assessment of independent retrieval methodologies and multi-year snowfall analysis, Atmospheric Research, 213, 121–135, https://doi.org/https://doi.org/10.1016/j.atmosres.2018.05.015, 2018.

Moreno-Ibáñez, M., Laprise, R., and and, P. G.: Recent advances in polar low research: current knowledge, challenges and future perspectives, Tellus A: Dynamic Meteorology and Oceanography, 73, 1–31, https://doi.org/10.1080/16000870.2021.1890412, 2021.

Morrison, H., de Boer, G., Feingold, G., Harrington, J., Shupe, M. D., and Sulia, K.: Resilience of persistent Arctic mixed-phase clouds, Nature Geoscience, 5, 11–17, https://doi.org/doi.org/10.1038/ngeo1332, 2012.

Mroz, K., Montopoli, M., Battaglia, A., Panegrossi, G., Kirstetter, P., and Baldini, L.:

Cross Validation of Active and Passive Microwave Snowfall Products over the Continental United States, Journal of Hydrometeorology, 22, 1297 – 1315, https://doi.org/10.1175/JHM-D-20-0222.1, 2021.

Mroz, K., Treserras, B. P., Battaglia, A., Kollias, P., Tatarevic, A., and Tridon, F.: Cloud and Precipitation Microphysical Retrievals from the EarthCARE Cloud Profiling Radar: the C-CLD product, EGUsphere, 2023, 1–33, https://doi.org/10.5194/egusphere-2023-56, 2023.

Mulet, S., Rio, M.-H., Etienne, H., Artana, C., Cancet, M., Dibarboure, G., Feng, H., Husson, R., Picot, N., Provost, C., and Strub, P. T.: The new CNES-CLS18 global mean dynamic topography, Ocean Science, 17, 789–808, https://doi.org/10.5194/os-17-789-2021, 2021.

Mulholland, J. P., Peters, J. M., and Morrison, H.: How Does Vertical Wind Shear Influence Entrainment in Squall Lines?, Journal of the Atmospheric Sciences, 78, 1931 – 1946, https://doi.org/10.1175/JAS-D-20-0299.1, 2021.

Mülmenstädt, J., Sourdeval, O., Delanoë, J., and Quaas, J.: Frequency of occurrence of rain from liquid-, mixed-, and ice-phase clouds derived from A-Train satellite retrievals, Geophysical Research Letters, 42, 6502–6509, https://doi.org/https://doi.org/10.1002/2015GL064604, 2015.

Neal, E., Huang, C. S. Y., and Nakamura, N.: The 2021 Pacific Northwest Heat Wave and Associated Blocking: Meteorology and the Role of an Upstream Cyclone as a Diabatic Source of Wave Activity, Geophysical Research Letters, 49, e2021GL097 699, https://doi.org/https://doi.org/10.1029/2021GL097699, 2022.

Nolan, D. S., Fischer, M. S., and O'Neill, M. E.: Reconsideration of the Mass and Condensate Sources for the Tropical Cyclone Outflow, Bulletin of the American Meteorological Society, pp. BAMS–D–24–0284.1, https://doi.org/10.1175/BAMS-D-24-0284.1, 2025.

Nuijens, L. and Siebesma, A. P.: Boundary Layer Clouds and Convection over Subtropical Oceans in our Current and in a Warmer Climate, Current Climate Change Reports, 5, 80–94, https://doi.org/10.1007/s40641-019-00126-x, 2019.

Palerme, C., Kay, J. E., Genthon, C., L'Ecuyer, T., Wood, N. B., and Claud, C.: How much snow falls on the Antarctic ice sheet?, The Cryosphere, 8, 1577–1587, https://doi.org/10.5194/tc-8-1577-2014, 2014.

Palerme, C., Genthon, C., Claud, C., Kay, J. E., Wood, N. B., and L'Ecuyer, T.: Evaluation of current and projected Antarctic precipitation in CMIP5 models, Climate Dynamics, 48, 225–239, https://doi.org/10.1007/s00382-016-3071-1, 2017.

Panegrossi, G., Casella, D., Sanò, P., Camplani, A., and Battaglia, A.: Chapter 12 - Recent advances and challenges in satellite-based snowfall detection and estimation, in: Pre-

cipitation Science, edited by Michaelides, S., pp. 333–376, Elsevier, https://doi.org/https://doi.org/10.1016/B978-0-12-822973-6.00015-9, 2022.

Pathak, J., Subramanian, S., Harrington, P., Raja, S., Chattopadhyay, A., Mardani, M., Kurth, T., Hall, D., Li, Z., Azizzadenesheli, K., et al.: Fourcastnet: A global data-driven high-resolution weather model using adaptive fourier neural operators, arXiv preprint arXiv:2202.11214, 2022.

Pazmany, A. L., Galloway, J. C., Mead, J. B., Popstefanija, I., McIntosh, R. E., and Bluestein, H. W.: Polarization Diversity Pulse-Pair technique for millimeter-wave Doppler radar measurements of severe storm features, Journal of Atmospheric and Oceanic Technology, 16, https://doi.org/10.1175/1520-0426(1999)016<1900:PDPPTF>2.0.CO;2, 1999.

Penven, P., Halo, I., Pous, S., and Marié, L.: Cyclogeostrophic balance in the Mozambique Channel, Journal of Geophysical Research: Oceans, 119, 1054–1067, https://doi.org/https://doi.org/10.1002/2013JC009528, 2014.

Perovich, D., Polashenski, C., Arntsen, A., and Stwertka, C.: Anatomy of a late spring snowfall on sea ice, Geophysical Research Letters, 44, 2802–2809, https://doi.org/https://doi.org/10.1002/2016GL071470, 2017.

Pithan, F. and Mauritsen, T.: Arctic amplification dominated by temperature feedbacks in contemporary climate models, Nature Geoscience, 7, 181–184, https://doi.org/10.1038/ngeo2071, 2014.

Pourret, V., Šavli, M., Mahfouf, J. F., Raspaud, D., Doerenbecher, A., Bénichou, H., and Payan, C.: Operational assimilation of Aeolus winds in the Météo-France global NWP model ARPEGE, Quarterly Journal of the Royal Meteorological Society, 148, https://doi.org/10.1002/qj.4329, 2022.

Price, I., Sanchez-Gonzalez, A., Alet, F., et al.: Probabilistic weather forecasting with machine learning, Nature, 637, 84–90, https://doi.org/10.1038/s41586-024-08252-9, 2025.

Protat, A., Delanoë, J., Bouniol, D., Heymsfield, A. J., Bansemer, A., and Brown, P.: Evaluation of ice water content retrievals from cloud radar reflectivity and temperature using a large airborne in situ microphysical database, Journal of Applied Meteorology and Climatology, 46, https://doi.org/10.1175/JAM2488.1, 2007.

Quante, L., Willner, S. N., Middelanis, R., and Levermann, A.: Regions of intensification of extreme snowfall under future warming, Scientific Reports, 11, https://doi.org/doi.org/10.1038/s41598-021-95979-4, 2021.

Rackow, T., Pedruzo-Bagazgoitia, X., Becker, T., Milinski, S., Sandu, I., Aguridan, R., Bechtold, P., Beyer, S., Bidlot, J., Boussetta, S., Deconinck, W., Diamantakis, M., Dueben, P., Dutra, E., Forbes, R., Ghosh, R., Goessling, H. F., Hadade, I., Hegewald, J., Jung, T., Keeley, S., Kluft,

L., Koldunov, N., Koldunov, A., Kölling, T., Kousal, J., Kühnlein, C., Maciel, P., Mogensen, K., Quintino, T., Polichtchouk, I., Reuter, B., Sármány, D., Scholz, P., Sidorenko, D., Streffing, J., Sützl, B., Takasuka, D., Tietsche, S., Valentini, M., Vannière, B., Wedi, N., Zampieri, L., and Ziemen, F.: Multi-year simulations at kilometre scale with the Integrated Forecasting System coupled to FESOM2.5 and NEMOv3.4, Geoscientific Model Development, 18, 33–69, https://doi.org/10.5194/gmd-18-33-2025, 2025.

Ralph, F. M., Dettinger, M. D., Cairns, M. M., Galarneau, T. J., and Neiman, P. J.: Hydrometeorological Characteristics of Flash-Flood-Producing Storm Systems in the Western United States, Weather and Forecasting, 26, 944–965, https://doi.org/10.1175/WAF-D-10-05030.1, 2011.

Rantanen, M., Karpechko, A. Y., Lipponen, A., Nordling, K., Hyvärinen, O., Ruosteenoja, K., Vihma, T., and Laaksonen, A.: The Arctic has warmed nearly four times faster than the globe since 1979, Nature Communications Earth & Environment, 3, https://doi.org/10.1038/s43247-022-00498-3, 2022.

Reitebuch, O.: Preparations for the Atmospheric Dynamics Mission Aeolus and the Aeolus Doppler Wind Lidar, Journal of Atmospheric and Oceanic Technology, 29, 1469–1491, https://doi.org/10.1175/JTECH-D-12-00078.1, 2012.

Renfrew, I. A.: Polar Lows, in: Encyclopedia of Atmospheric Sciences, vol. 3, pp. 1761–1768, Academic Press, https://doi.org/10.1016/B0-12-227090-8/00370-9, 2003.

Rennie, M. P., Isaksen, L., Weiler, F., de Kloe, J., Kanitz, T., and Reitebuch, O.: The impact of Aeolus wind retrievals on ECMWF global weather forecasts, Quarterly Journal of the Royal Meteorological Society, 147, https://doi.org/10.1002/qj.4142, 2021.

Rizik, A., Battaglia, A., Tridon, F., Scarsi, F. E., Kötsche, A., Kalesse-Los, H., Maahn, M., and Illingworth, A.: Impact of Crosstalk on Reflectivity and Doppler Measurements for the WIVERN Polarization Diversity Doppler Radar, IEEE Transactions on Geoscience and Remote Sensing, 61, 1–14, https://doi.org/10.1109/TGRS.2023.3320287, 2023.

Rodwell, M. J., Magnusson, L., Bauer, P., Bechtold, P., Bonavita, M., Cardinali, C., Diamantakis, M., Earnshaw, P., Garcia-Mendez, A., Isaksen, L., Källén, E., Klocke, D., Lopez, P., McNally, T., Persson, A., Prates, F., and Wedi, N.: Characteristics of Occasional Poor Medium-Range Weather Forecasts for Europe, Bulletin of the American Meteorological Society, 94, 1393 – 1405, https://doi.org/10.1175/BAMS-D-12-00099.1, 2013.

Rodwell, M. J., Hewson, T. D., Pappenberger, F., Richardson, D. S., and Zsótér, E.: Why model climate variability matters for weather prediction, Journal of Geophysical Research: Atmospheres, 123, 9320–9332, https://doi.org/10.1029/2018JD028727, 2018.

Roemmich, D., Alford, M. H., Claustre, H., Johnson, K., King, B., Moum, J., Oke, P., Owens, W. B., Pouliquen, S., Purkey, S., Scanderbeg, M., Suga, T., Wijffels, S., Zilberman, N., Bakker,

D., Baringer, M., Belbeoch, M., Bittig, H. C., Boss, E., Calil, P., Carse, F., Carval, T., Chai, F., Conchubhair, D. O., d'Ortenzio, F., Dall'Olmo, G., Desbruyeres, D., Fennel, K., Fer, I., Ferrari, R., Forget, G., Freeland, H., Fujiki, T., Gehlen, M., Greenan, B., Hallberg, R., Hibiya, T., Hosoda, S., Jayne, S., Jochum, M., Johnson, G. C., Kang, K., Kolodziejczyk, N., Körtzinger, A., Traon, P.-Y. L., Lenn, Y.-D., Maze, G., Mork, K. A., Morris, T., Nagai, T., Nash, J., Garabato, A. N., Olsen, A., Pattabhi, R. R., Prakash, S., Riser, S., Schmechtig, C., Schmid, C., Shroyer, E., Sterl, A., Sutton, P., Talley, L., Tanhua, T., Thierry, V., Thomalla, S., Toole, J., Troisi, A., Trull, T. W., Turton, J., Velez-Belchi, P. J., Walczowski, W., Wang, H., Wanninkhof, R., Waterhouse, A. F., Waterman, S., Watson, A., Wilson, C., Wong, A. P. S., Xu, J., and Yasuda, I.: On the Future of Argo: A Global, Full-Depth, Multi-Disciplinary Array, Frontiers in Marine Science, 6, https://doi.org/10.3389/fmars.2019.00439, 2019.

Romeiser, R., Breit, H., Eineder, M., Runge, H., Flament, P., de Jong, K., and Vogelzang, J.: Current measurements by SAR along-track interferometry from a Space Shuttle, IEEE Transactions on Geoscience and Remote Sensing, 43, 2315–2324, https://doi.org/https://doi.org/10.1109/TGRS.2005.856116, 2005.

Rostosky, P., Spreen, G., Farrell, S. L., Frost, T., Heygster, G., and Melsheimer, C.: Snow Depth Retrieval on Arctic Sea Ice From Passive Microwave Radiometers—Improvements and Extensions to Multiyear Ice Using Lower Frequencies, J. Geophys. Res. Oc., 123, 7120–7138, https://doi.org/10.1029/2018jc014028, 2018.

Röthlisberger, M. and Papritz, L.: Quantifying the physical processes leading to atmospheric hot extremes at a global scale, Nature Geoscience, 16, 210–216, https://doi.org/10.1038/s41561-023-01126-1, 2023.

Ruppert, J. H. and Johnson, R. H.: Diurnally Modulated Cumulus Moistening in the Preonset Stage of the Madden–Julian Oscillation during DYNAMO, Journal of the Atmospheric Sciences, 72, 1622 – 1647, https://doi.org/10.1175/JAS-D-14-0218.1, 2015.

Salonen, K., Cotton, J., Bormann, N., and Forsythe, M.: Characterizing AMV height-assignment error by comparing best-fit pressure statistics from the met office and ECMWF data assimilation systems, Journal of Applied Meteorology and Climatology, 54, https://doi.org/10.1175/JAMCD-14-0025.1, 2015.

Sasso, N., Borderies, M., Chambon, P., Berre, L., Girardot, N., Moll, P., Payan, C., Pourret, V., Battaglia, A., Illingworth, A., Rennie, M., and Pourshamsi, M.: Impact of WIVERN Wind Observations on ARPEGE Numerical Weather Prediction Model Forecasts Using an Ensemble of Data Assimilation Method, Quarterly Journal of the Royal Meteorological Society, n/a, e4991, https://doi.org/https://doi.org/10.1002/qj.4991, 2025.

Scarsi, F. E., Battaglia, A., Tridon, F., Martire, P., Dhillon, R., and Illingworth, A.: Mispointing correction methods for the conically scanning WIVERN Doppler radar, Atmospheric Measurement Techniques Discussions, pp. 1–26, https://doi.org/10.5194/amt-2023-117, 2023.

Schoger, S. Y., Moisseev, D., von Lerber, A., Crewell, S., and Ebell, K.: Snowfall-Rate Retrieval for K- and W-Band Radar Measurements Designed in Hyytiälä, Finland, and Tested at Ny-Ålesund, Svalbard, Norway, Journal of Applied Meteorology and Climatology, 60, 273 – 289, https://doi.org/10.1175/JAMC-D-20-0095.1, 2021.

Schultz, D. M. and Browning, K. A.: What is a sting jet?, Weather, 72, 63–66, https://doi.org/https://doi.org/10.1002/wea.2795, 2017.

Schultz, M. G., Betancourt, C., Gong, B., Kleinert, F., Langguth, M., Leufen, L. H., Mozaffari, A., and Stadtler, S.: Can deep learning beat numerical weather prediction?, Philosophical Transactions of the Royal Society A: Mathematical, Physical and Engineering Sciences, 379, 20200 097, https://doi.org/10.1098/rsta.2020.0097, 2021.

Schäfler, A., Craig, G., Wernli, H., Arbogast, P., Doyle, J. D., McTaggart-Cowan, R., Methven, J., Rivière, G., Ament, F., Boettcher, M., Bramberger, M., Cazenave, Q., Cotton, R., Crewell, S., Delanoë, J., Dörnbrack, A., Ehrlich, A., Ewald, F., Fix, A., Grams, C. M., Gray, S. L., Grob, H., Groß, S., Hagen, M., Harvey, B., Hirsch, L., Jacob, M., Kölling, T., Konow, H., Lemmerz, C., Lux, O., Magnusson, L., Mayer, B., Mech, M., Moore, R., Pelon, J., Quinting, J., Rahm, S., Rapp, M., Rautenhaus, M., Reitebuch, O., Reynolds, C. A., Sodemann, H., Spengler, T., Vaughan, G., Wendisch, M., Wirth, M., Witschas, B., Wolf, K., and Zinner, T.: The North Atlantic Waveguide and Downstream Impact Experiment, Bulletin of the American Meteorological Society, 99, 1607 – 1637, https://doi.org/10.1175/BAMS-D-17-0003.1, 2018.

Schäfler, A., Harvey, B., Doyle, J. D., Rasp, S., Craig, G. C., and Wernli, H.: Diabatic influence on forecast errors: A case study of a rapidly intensifying cyclone, Monthly Weather Review, 148, 1037–1057, https://doi.org/10.1175/MWR-D-19-0180.1, 2020.

Seeley, J. et al.: Formation of tropical anvil clouds through slow evaporation and mass detrainment: Insights from km-scale simulations, Geophysical Research Letters, 46, 7422–7431, https://doi.org/10.1029/2019GL083573, 2019.

Segura, H., Pedruzo-Bagazgoitia, X., Weiss, P., Müller, S. K., Rackow, T., Lee, J., Dolores-Tesillos, E., Benedict, I., Aengenheyster, M., Aguridan, R., Arduini, G., Baker, A. J., Bao, J., Bastin, S., Baulenas, E., Becker, T., Beyer, S., Bockelmann, H., Brüggemann, N., Brunner, L., Cheedela, S. K., Das, S., Denissen, J., Dragaud, I., Dziekan, P., Ekblom, M., Engels, J. F., Esch, M., Forbes, R., Frauen, C., Freischem, L., García-Maroto, D., Geier, P., Gierz, P., González-Cervera, A., Grayson, K., Griffith, M., Gutjahr, O., Haak, H., Hadade, I., Haslehner, K., ul Hasson, S., Hegewald, J., Kluft, L., Koldunov, A., Koldunov, N., Kölling, T., Koseki, S., Kosukhin, S., Kousal, J., Kuma, P., Kumar, A. U., Li, R., Maury, N., Meindl, M., Milinski, S., Mogensen, K., Niraula, B., Nowak, J., Praturi, D. S., Proske, U., Putrasahan, D., Redler, R., Santuy, D., Sármány, D., Schnur, R., Scholz, P., Sidorenko, D., Spät, D., Sützl, B., Takasuka, D., Tompkins, A., Uribe, A., Valentini, M., Veerman, M., Voigt, A., Warnau, S., Wachsmann, F., Wacławczyk, M., Wedi, N., Wieners, K.-H., Wille, J., Winkler, M., Wu, Y., Ziemen, F.,

Zimmermann, J., Bender, F. A.-M., Bojovic, D., Bony, S., Bordoni, S., Brehmer, P., Dengler, M., Dutra, E., Faye, S., Fischer, E., van Heerwaarden, C., Hohenegger, C., Järvinen, H., Jochum, M., Jung, T., Jungclaus, J. H., Keenlyside, N. S., Klocke, D., Konow, H., Klose, M., Malinowski, S., Martius, O., Mauritsen, T., Mellado, J. P., Mieslinger, T., Mohino, E., Pawłowska, H., Peters-von Gehlen, K., Sarré, A., Sobhani, P., Stier, P., Tuppi, L., Vidale, P. L., Sandu, I., and Stevens, B.: nextGEMS: entering the era of kilometer-scale Earth system modeling, EGUsphere, 2025, 1–39, https://doi.org/10.5194/egusphere-2025-509, 2025.

Selz, T., Riemer, M., and Craig, G. C.: The Transition from Practical to Intrinsic Predictability of Midlatitude Weather, Journal of the Atmospheric Sciences, 79, 2013–2030, https://doi.org/10.1175/JAS-D-21-0271.1, 2022.

Shaw, T. A. and Stevens, B.: The other climate crisis, Nature, 639, 877–887, https://doi.org/10.1038/s41586-025-08680-1, 2025.

Shaw, T. A., Arias, P. A., Collins, M., Coumou, D., Diedhiou, A., Garfinkel, C. I., Jain, S., Roxy, M. K., Kretschmer, M., Leung, L. R., Narsey, S., Martius, O., Seager, R., Shepherd, T. G., Sörensson, A. A., Stephenson, T., Taylor, M., and Wang, L.: Regional climate change: consensus, discrepancies, and ways forward, Frontiers in Climate, 6, https://doi.org/10.3389/fclim.2024.1391634, 2024.

Sherwood, S. C., Webb, M. J., Annan, J. D., Armour, K. C., Forster, P. M., Hargreaves, J. C., Hegerl, G. C., Klein, S. A., Marvel, K. D., Rohling, E. J., Watanabe, M., Andrews, T., Braconnot, P., Bretherton, C. S., Foster, G. L., Hausfather, Z., von der Heydt, A. S., Knutti, R., Mauritsen, T., Norris, J. R., Proistosescu, C., Rugenstein, M., Schmidt, G. A., Tokarska, K. B., and Zelinka, M. D.: An assessment of Earth's climate sensitivity using multiple lines of evidence, Reviews of Geophysics, 58, e2019RG000678, https://doi.org/10.1029/2019RG000678, 2020.

Simonin, D., Pierce, C., Roberts, N., Ballard, S. P., and Li, Z.: Performance of Met Office hourly cycling NWP-based nowcasting for precipitation forecasts, Quarterly Journal of the Royal Meteorological Society, 143, 2862–2873, https://doi.org/https://doi.org/10.1002/qj.3136, 2017.

Simpson, I. R., Shaw, T. A., Ceppi, P., Clement, A. C., Fischer, E., Grise, K. M., Pendergrass, A. G., Screen, J. A., Wills, R. C. J., Woollings, T., Blackport, R., Kang, J. M., and Po-Chedley, S.: Confronting Earth System Model trends with observations, Science Advances, 11, eadt8035, https://doi.org/10.1126/sciadv.adt8035, 2025.

Skofronick-Jackson, G. and Johnson, B. T.: Surface and atmospheric contributions to passive microwave brightness temperatures for falling snow events, Journal of Geophysical Research: Atmospheres, 116, https://doi.org/https://doi.org/10.1029/2010JD014438, 2011.

Skofronick-Jackson, G., Kim, M.-J., Weinman, J., and Chang, D.-E.: A physical model to de-

termine snowfall over land by microwave radiometry, IEEE Transactions on Geoscience and Remote Sensing, 42, 1047–1058, https://doi.org/10.1109/TGRS.2004.825585, 2004.

Skofronick-Jackson, G., Kirschbaum, D., Petersen, W., Huffman, G., Kidd, C., Stocker, E., and Kakar, R.: The Global Precipitation Measurement (GPM) mission's scientific achievements and societal contributions: reviewing four years of advanced rain and snow observations, Quarterly Journal of the Royal Meteorological Society, 144, 27–48, https://doi.org/10.1002/qj.3313, 2018.

Slatyer, R. A., Umbers, K. D. L., and Arnold, P. A.: Ecological responses to variation in seasonal snow cover, Conservation Biology, 36, e13 727, https://doi.org/https://doi.org/10.1111/cobi.13727, 2022.

Souverijns, N., Gossart, A., Gorodetskaya, I. V., Lhermitte, S., Mangold, A., Laffineur, Q., Delcloo, A., and van Lipzig, N. P. M.: How does the ice sheet surface mass balance relate to snowfall? Insights from a ground-based precipitation radar in East Antarctica, The Cryosphere, 12, 1987–2003, https://doi.org/10.5194/tc-12-1987-2018, 2018a.

Souverijns, N., Gossart, A., Lhermitte, S., Gorodetskaya, I. V., Grazioli, J., Berne, A., Duran-Alarcon, C., Boudevillain, B., Genthon, C., Scarchilli, C., and van Lipzig, N. P. M.: Evaluation of the CloudSat surface snowfall product over Antarctica using ground-based precipitation radars, The Cryosphere, 12, 3775–3789, https://doi.org/10.5194/tc-12-3775-2018, 2018b.

Steiger, R., Scott, D., Abegg, B., Pons, M., and Aall, C.: A critical review of climate change risk for ski tourism, Current Issues in Tourism, 22, 1343–1379, https://doi.org/10.1080/13683500.2017.1410110, 2019.

Stephens, G., Winker, D., Pelon, J., Trepte, C., Vane, D., Yuhas, C., L'Ecuyer, T., and Lebsock, M.: CloudSat and CALIPSO within the A-Train: Ten Years of Actively Observing the Earth System, Bulletin of the American Meteorological Society, 99, 569 – 581, https://doi.org/10.1175/BAMS-D-16-0324.1, 2018.

Stephens, G. L., Shiro, K. A., Hakuba, M. Z., Takahashi, H., Pilewskie, J. A., Andrews, T., Stubenrauch, C. J., and Wu, L.: Tropical Deep Convection, Cloud Feedbacks and Climate Sensitivity, Surveys in Geophysics, 45, 1903–1931, https://doi.org/10.1007/s10712-024-09831-1, 2024.

Stevens, B., Vali, G., Comstock, K., Wood, R., van Zanten, M. C., Austin, P. H., Bretherton, C. S., and Lenschow, D. H.: POCKETS OF OPEN CELLS AND DRIZZLE IN MARINE STRATOCUMULUS, Bulletin of the American Meteorological Society, 86, 51 – 58, https://doi.org/10.1175/BAMS-86-1-51, 2005.

Stevens, B., Satoh, M., Auger, L., Biercamp, J., Bretherton, C. S., Chen, X., Düben, P., Judt, F., Khairoutdinov, M., Klocke, D., Kodama, C., Kornblueh, L., Lin, S. J., Neumann, P., Putman, W. M., Röber, N., Shibuya, R., Vanniere, B., Vidale, P. L., and Zhou, L.: DYAMOND:

the DYnamics of the Atmospheric general circulation Modeled On Non-hydrostatic Domains, Progress in Earth and Planetary Science, 6, https://doi.org/10.1186/s40645-019-0304-z, 2019.

Stevens, B., Bony, S., Farrell, D., Ament, F., Blyth, A., Fairall, C., Karstensen, J., Quinn, P. K., Speich, S., Acquistapace, C., Aemisegger, F., Albright, A. L., Bellenger, H., Bodenschatz, E., Caesar, K.-A., Chewitt-Lucas, R., de Boer, G., Delanoë, J., Denby, L., Ewald, F., Fildier, B., Forde, M., George, G., Gross, S., Hagen, M., Hausold, A., Heywood, K. J., Hirsch, L., Jacob, M., Jansen, F., Kinne, S., Klocke, D., Kölling, T., Konow, H., Lothon, M., Mohr, W., Naumann, A. K., Nuijens, L., Olivier, L., Pincus, R., Pöhlker, M., Reverdin, G., Roberts, G., Schnitt, S., Schulz, H., Siebesma, A. P., Stephan, C. C., Sullivan, P., Touzé-Peiffer, L., Vial, J., Vogel, R., Zuidema, P., Alexander, N., Alves, L., Arixi, S., Asmath, H., Bagheri, G., Baier, K., Bailey, A., Baranowski, D., Baron, A., Barrau, S., Barrett, P. A., Batier, F., Behrendt, A., Bendinger, A., Beucher, F., Bigorre, S., Blades, E., Blossey, P., Bock, O., Böing, S., Bosser, P., Bourras, D., Bouruet-Aubertot, P., Bower, K., Branellec, P., Branger, H., Brennek, M., Brewer, A., Brilouet, P.-E., Brügmann, B., Buehler, S. A., Burke, E., Burton, R., Calmer, R., Canonici, J.-C., Carton, X., Cato Jr., G., Charles, J. A., Chazette, P., Chen, Y., Chilinski, M. T., Choularton, T., Chuang, P., Clarke, S., Coe, H., Cornet, C., Coutris, P., Couvreux, F., Crewell, S., Cronin, T., Cui, Z., Cuypers, Y., Daley, A., Damerell, G. M., Dauhut, T., Deneke, H., Desbios, J.-P., Dörner, S., Donner, S., Douet, V., Drushka, K., Dütsch, M., Ehrlich, A., Emanuel, K., Emmanouilidis, A., Etienne, J.-C., Etienne-Leblanc, S., Faure, G., Feingold, G., Ferrero, L., Fix, A., Flamant, C., Flatau, P. J., Foltz, G. R., Forster, L., Furtuna, I., Gadian, A., Galewsky, J., Gallagher, M., Gallimore, P., Gaston, C., Gentemann, C., Geyskens, N., Giez, A., Gollop, J., Gouirand, I., Gourbeyre, C., de Graaf, D., de Groot, G. E., Grosz, R., Güttler, J., Gutleben, M., Hall, K., Harris, G., Helfer, K. C., Henze, D., Herbert, C., Holanda, B., Ibanez-Landeta, A., Intrieri, J., Iyer, S., Julien, F., Kalesse, H., Kazil, J., Kellman, A., Kidane, A. T., Kirchner, U., Klingebiel, M., Körner, M., Kremper, L. A., Kretzschmar, J., Krüger, O., Kumala, W., Kurz, A., L'Hégaret, P., Labaste, M., Lachlan-Cope, T., Laing, A., Landschützer, P., Lang, T., Lange, D., Lange, I., Laplace, C., Lavik, G., Laxenaire, R., Le Bihan, C., Leandro, M., Lefevre, N., Lena, M., Lenschow, D., Li, Q., Lloyd, G., Los, S., Losi, N., Lovell, O., Luneau, C., Makuch, P., Malinowski, S., Manta, G., Marinou, E., Marsden, N., Masson, S., Maury, N., Mayer, B., Mayers-Als, M., Mazel, C., McGeary, W., McWilliams, J. C., Mech, M., Mehlmann, M., Meroni, A. N., Mieslinger, T., Minikin, A., Minnett, P., Möller, G., Morfa Avalos, Y., Muller, C., Musat, I., Napoli, A., Neuberger, A., Noisel, C., Noone, D., Nordsiek, F., Nowak, J. L., Oswald, L., Parker, D. J., Peck, C., Person, R., Philippi, M., Plueddemann, A., Pöhlker, C., Pörtge, V., Pöschl, U., Pologne, L., Posyniak, M., Prange, M., Quiñones Meléndez, E., Radtke, J., Ramage, K., Reimann, J., Renault, L., Reus, K., Reyes, A., Ribbe, J., Ringel, M., Ritschel, M., Rocha, C. B., Rochetin, N., Röttenbacher, J., Rollo, C., Royer, H., Sadoulet, P., Saffin, L., Sandiford, S., Sandu, I., Schäfer, M., Schemann, V., Schirmacher, I., Schlenczek, O., Schmidt, J., Schröder, M., Schwarzenboeck, A., Sealy, A., Senff, C. J., Serikov, I., Shohan,

S., Siddle, E., Smirnov, A., Späth, F., Spooner, B., Stolla, M. K., Szkółka, W., de Szoeke, S. P., Tarot, S., Tetoni, E., Thompson, E., Thomson, J., Tomassini, L., Totems, J., Ubele, A. A., Villiger, L., von Arx, J., Wagner, T., Walther, A., Webber, B., Wendisch, M., Whitehall, S., Wiltshire, A., Wing, A. A., Wirth, M., Wiskandt, J., Wolf, K., Worbes, L., Wright, E., Wulfmeyer, V., Young, S., Zhang, C., Zhang, D., Ziemen, F., Zinner, T., and Zöger, M.: EUREC^{4}A, Earth System Science Data, 13, 4067–4119, https://doi.org/10.5194/essd-13-4067-2021, 2021.

Stoll, J., Spengler, T., and Sodemann, H.: Polar lows in the North Atlantic: Climatology and development characteristics from ERA5 and cyclone tracking, Weather and Climate Dynamics, 3, 1–22, https://doi.org/10.5194/wcd-3-1-2022, 2022.

Strong, C. K., Ye, Z., and Shi, X.: Safety Effects of Winter Weather: The State of Knowledge and Remaining Challenges, Transport Reviews, 30, 677–699, https://doi.org/10.1080/01441640903414470, 2010.

Tamarin-Brodsky, T. and Kaspi, Y.: Enhanced poleward propagation of storms under climate change, Nature Geoscience, 10, 908–913, https://doi.org/10.1038/s41561-017-0001-8, 2017.

Tanelli, S., Durden, S. L., Im, E., Pak, K. S., Reinke, D. G., Partain, P., Haynes, J. M., and Marchand, R. T.: CloudSat's cloud profiling radar after two years in orbit: Performance, calibration, and processing, IEEE Transactions on Geoscience and Remote Sensing, 46, https://doi.org/10.1109/TGRS.2008.2002030, 2008.

Tao, W.-K., Takayabu, Y. N., Lang, S., Shige, S., Olson, W., Hou, A., Skofronick-Jackson, G., Jiang, X., Zhang, C., Lau, W., Krishnamurti, T., Waliser, D., Grecu, M., Ciesielski, P. E., Johnson, R. H., Houze, R., Kakar, R., Nakamura, K., Braun, S., Hagos, S., Oki, R., and Bhardwaj, A.: TRMM Latent Heating Retrieval: Applications and Comparisons with Field Campaigns and Large-Scale Analyses, Meteorological Monographs, 56, 2.1–2.34, https://doi.org/10.1175/AMSMONOGRAPHS-D-15-0013.1, 2016.

Terpstra, A., Spengler, T., and Moore, R. W.: Idealized simulations of polar low development under strong baroclinicity, Quarterly Journal of the Royal Meteorological Society, 141, 1987–1996, https://doi.org/10.1002/qj.2490, 2015.

Terpstra, A., Michel, C., and Spengler, T.: Polar low tracks from 44 years of satellite observations, Geophysical Research Letters, 48, e2021GL093 698, https://doi.org/10.1029/2021GL093698, 2021.

Tridon, F., Silber, I., Battaglia, A., Kneifel, S., Fridlind, A., Kalogeras, P., and Dhillon, R.: Highly supercooled riming and unusual triple-frequency radar signatures over McMurdo Station, Antarctica, Atmos. Chem. Phys., 22, 12 467–12 491, https://doi.org/10.5194/acp-22-12467-2022, 2022.

Varble, A., Fridlind, A. M., Zipser, E. J., Ackerman, A. S., Chaboureau, J. P., Fan, J., Hill, A.,

McFarlane, S. A., Pinty, J. P., and Shipway, B.: Evaluation of cloud-resolving model intercomparison simulations using TWP-ICE observations: Precipitation and cloud structure, Journal of Geophysical Research Atmospheres, 116, 1–22, https://doi.org/10.1029/2010JD015180, 2011.

Varble, A., Morrison, H., and Zipser, E.: Effects of Under-Resolved Convective Dynamics on the Evolution of a Squall Line, Monthly Weather Review, 148, 289 – 311, https://doi.org/10.1175/MWR-D-19-0187.1, 2020.

Vial, J., Bony, S., Stevens, B., and Vogel, R.: Mechanisms and Model Diversity of Trade-Wind Shallow Cumulus Cloud Feedbacks: A Review, Surveys in Geophysics, 38, 1331–1353, https://doi.org/10.1007/s10712-017-9418-2, 2017.

Vogel, R., Albright, A. L., Vial, J., George, G., Stevens, B., and Bony, S.: Strong cloud–circulation coupling explains weak trade cumulus feedback, Nature, 612, 696–700, https://doi.org/10.1038/s41586-022-05364-y, 2022.

von Schuckmann, K., Minière, A., Gues, F., Cuesta-Valero, F. J., Kirchengast, G., Adusumilli, S., Straneo, F., Ablain, M., Allan, R. P., Barker, P. M., Beltrami, H., Blazquez, A., Boyer, T., Cheng, L., Church, J., Desbruyeres, D., Dolman, H., Domingues, C. M., García-García, A., Giglio, D., Gilson, J. E., Gorfer, M., Haimberger, L., Hakuba, M. Z., Hendricks, S., Hosoda, S., Johnson, G. C., Killick, R., King, B., Kolodziejczyk, N., Korosov, A., Krinner, G., Kuusela, M., Landerer, F. W., Langer, M., Lavergne, T., Lawrence, I., Li, Y., Lyman, J., Marti, F., Marzeion, B., Mayer, M., MacDougall, A. H., McDougall, T., Monselesan, D. P., Nitzbon, J., Otosaka, I., Peng, J., Purkey, S., Roemmich, D., Sato, K., Sato, K., Savita, A., Schweiger, A., Shepherd, A., Seneviratne, S. I., Simons, L., Slater, D. A., Slater, T., Steiner, A. K., Suga, T., Szekely, T., Thiery, W., Timmermans, M.-L., Vanderkelen, I., Wjiffels, S. E., Wu, T., and Zemp, M.: Heat stored in the Earth system 1960–2020: where does the energy go?, Earth System Science Data, 15, 1675–1709, https://doi.org/10.5194/essd-15-1675-2023, 2023.

Waite, M. L. and Khouider, B.: The Deepening of Tropical Convection by Congestus Preconditioning, Journal of the Atmospheric Sciences, 67, 2601 – 2615, https://doi.org/10.1175/2010JAS3357.1, 2010.

Wandel, J., Quinting, J. F., and Grams, C. M.: Toward a Systematic Evaluation of Warm Conveyor Belts in Numerical Weather Prediction and Climate Models. Part II: Verification of Operational Reforecasts, Journal of the Atmospheric Sciences, 78, 1487–1507, https://doi.org/10.1175/JAS-D-20-0385.1, 2021.

Wasti, A., Ray, P., Wi, S., Folch, C., Ubierna, M., and Karki, P.: Climate change and the hydropower sector: A global review, WIREs Climate Change, 13, e757, https://doi.org/https://doi.org/10.1002/wcc.757, 2022.

Wattrelot, E., Caumont, O., and Mahfouf, J.-F.: Operational Implementation of the 1D+3D-

Var Assimilation Method of Radar Reflectivity Data in the AROME Model, Monthly Weather Review, 142, 1852 – 1873, https://doi.org/10.1175/MWR-D-13-00230.1, 2014.

Wehr, T., Kubota, T., Tzeremes, G., Wallace, K., Nakatsuka, H., Ohno, Y., Koopman, R., Rusli, S., Kikuchi, M., Eisinger, M., Tanaka, T., Taga, M., Deghaye, P., Tomita, E., and Bernaerts, D.: The EarthCARE mission – science and system overview, Atmospheric Measurement Techniques, 16, 3581–3608, https://doi.org/10.5194/amt-16-3581-2023, 2023.

Wendisch, M., Brückner, M., Crewell, S., Ehrlich, A., Notholt, J., Lüpkes, C., Macke, A., Burrows, J. P., Rinke, A., Quaas, J., et al.: Atmospheric and Surface Processes, and Feedback Mechanisms Determining Arctic Amplification: A Review of First Results and Prospects of the (AC)³ Project, Bulletin of the American Meteorological Society, 104, E208–E242, https://doi.org/10.1175/BAMS-D-21-0218.1, 2023.

Wernli, H. and Gray, S. L.: Recent advances in understanding extratropical cyclone dynamics and predictability, Quarterly Journal of the Royal Meteorological Society, in press, 2024.

Windmiller, J. M. and Stevens, B.: The inner life of the Atlantic Intertropical Convergence Zone, Quarterly Journal of the Royal Meteorological Society, 150, 523–543, https://doi.org/https://doi.org/10.1002/qj.4610, 2024.

WMO: The 7th WMO Workshop on the Impact of Various Observing Systems on Numerical Weather Prediction, URL https://community.wmo.int/en/meetings/NWP-7, geneva, Switzerland, 2020.

WMO, IOC-UNESCO, ISC, UNEP, and C3S: The 2022 GCOS ECVs Requirements, Tech. rep., WMO, URL https://library.wmo.int/idurl/4/58111, available at https://library.wmo.int/idurl/4/58111, 2022.

Wolde, M., Battaglia, A., Nguyen, C., Pazmany, A. L., and Illingworth, A.: Implementation of polarization diversity pulse-pair technique using airborne W-band radar, Atmospheric Measurement Techniques, 12, https://doi.org/10.5194/amt-12-253-2019, 2019.

World Meteorological Organization: Observing Systems Capability Analysis and Review Tool (OSCAR), URL https://space.oscar.wmo.int/observingrequirements, 2016.

Wu, S.-N. and Soden, B. J.: Signatures of Tropical Cyclone Intensification in Satellite Measurements of Ice and Liquid Water Content, Monthly Weather Review, 145, 4081 – 4091, https://doi.org/10.1175/MWR-D-17-0046.1, 2017.

Yanai, M., Esbensen, S., and Chu, J.-H.: Determination of Bulk Properties of Tropical Cloud Clusters from Large-Scale Heat and Moisture Budgets, Journal of Atmospheric Sciences, 30, 611 – 627, https://doi.org/10.1175/1520-0469(1973)030<0611:DOBPOT>2.0.CO;2, 1973.

Zhang, C., Adames, A. F., Khouider, B., Wang, B., and Yang, D.: Four Theories of the Madden-

Julian Oscillation, Reviews of Geophysics, 58, e2019RG000 685, https://doi.org/https://doi.org/10.1029/2019RG000685, 2020.

Zhang, M.: An Analytical Model of Two-Dimensional Mesoscale Circulation and Associated Properties Across Squall Lines, AGU Advances, 3, e2022AV000 726, https://doi.org/https://doi.org/10.1029/2022AV000726, e2022AV000726 2022AV000726, 2022.

Zuidema, P., Li, Z., Hill, R. J., Bariteau, L., Rilling, B., Fairall, C., Brewer, W. A., Albrecht, B., and Hare, J.: On Trade Wind Cumulus Cold Pools, Journal of the Atmospheric Sciences, 69, 258 – 280, https://doi.org/10.1175/JAS-D-11-0143.1, 2012.

Zuidema, P., Torri, G., Muller, C., and Chandra, A.: A Survey of Precipitation-Induced Atmospheric Cold Pools over Oceans and Their Interactions with the Larger-Scale Environment, Surveys in Geophysics, 38, 1283–1305, https://doi.org/10.1007/s10712-017-9447-x, 2017.

APPENDIX C. WIVERN PERFORMANCE REFERENCE ATMOSPHERE SCENARIOS

The content for Reference Atmoshpere Scenarios will be consolidated during Phase A.

APPENDIX D. REFERENCE FRAMES DEFINITIONS AND ATTITUDE LAW

This appendix defines a set of reference frames definitions and conventions and is fully applicable to anyone working on the WIVERN project at any level. Any document produced within the WIVERN project shall strictly adhere to the definitions and conventions described hereafter.

Four main levels of reference frames are used for attitude determination:

- A set of orbital frames:
  - The Satellite Orbital frame (SOF) and the Satellite Orbital Frame 2 (SOF2)
  - Local Velocity Orbital reference frame
  - Zero-Doppler Orbital Reference Frame (0-DopRF)
  - Local Normal Pointing (LNP) reference frame
  - Yaw Steering Mode (YSM) reference frame
- The Satellite Nominal Reference Frame (SNRF)
- A set of Satellite Reference Frames (SRF):
  - Mechanical Satellite Reference Frame (SRF_{mech})
  - Center of Gravity Centered Satellite Reference Frame (SRF_{COG})
  - Attitude and Orbital Control Subsystem SRF (SRF_{AOCS})
- A set of Instrument Reference Frames (IRF):
  - Static Instrument Reference Frame (IRF_{Stat})
  - Rotating Instrument Reference Frame (IRF_{Rot})
  - Antenna Radio Frequency Instrument Reference Frame (IRF_{AntRF})

The SOF/SOF2 are the master non-inertial orbital reference frames, used as a reference for the computation of the other reference frames. The other orbital frames that are introduced can be of interest to define the attitude guidance as well. However, not necessarily all of them shall be used, but if one or more are used, the nomenclature and notation shall be consistent with this document.

The SNRF is a reference frame to describe the nominal attitude of the satellite. Its definition depends on the attitude law chosen for the satellite.

The SRF are a set of reference frames that correspond with the satellite actual attitude frame that is realised on orbit. They are rigidly attached to the satellite structure. Note that unlike the definition in [RD-26] the orientation of the SRF in space is determined by the actual spacecraft attitude, and not the measured one.

The IRF are reference frames associated with the instrument and can be rigidly attached to the spacecraft or rotating with the antenna.

D.1. Satellite Orbital Frames

Satellite Orbital Frame (SOF)

The Satellite Orbital Frame (SOF) is defined in [RD-26]. It is a right-handed orthogonal reference frame centred on the satellite. It is a non-inertial time-dependent reference frame, defined by the $\vec{X}_s$, $\vec{Y}_s$ and $\vec{Z}_s$ axes, which are specified relatively to the reference inertial reference frame, i.e. the True of Date (TOD) frame.

The $\vec{Z}_s$ axis points along the radial satellite direction vector, positive from the center of the TOD reference frame towards the satellite, the $\vec{Y}_s$ axis points along the transversal direction vector within the osculating orbital plane (i.e the plane defined by the position and velocity vectors of the satellite), orthogonal to the $\vec{Z}_s$ axis and opposed to the direction of the orbital motion of the satellite. The $\vec{X}_s$ axis points towards the out of-plane direction vector completing the right-hand reference frame.

$$\vec{Z}_s = \frac{\vec{r}}{|\vec{r}|}; \vec{X}_s = \frac{\vec{r} \wedge \vec{v}}{|\vec{r} \wedge \vec{v}|}; \vec{Y}_s = \vec{Z}_s \wedge \vec{X}_s$$

where $\vec{r}$ and $\vec{v}$ are the position and inertial velocity vectors of the satellite expressed in the inertial reference frame.

Satellite Orbital Frame 2 (SOF2)

It is customary in Earth Observation to use a reference frame whereby the z-axis is nadir-pointing. In order to avoid confusion, we will distinguish between the SOF reference frame defined above, which follows the definition in [RD-26] and a rotated system SOF2 which is defined as follows: SOF2 is a reference frame sharing the same origin of SOF, i.e. centred on the satellite. It is defined by the $\vec{X}_s$, $\vec{Y}_s$ and $\vec{Z}_s$ axes, which are specified relatively to the theoretical SOF by applying the following:

$$\vec{X}_{s2} = -\vec{Y}_s; \vec{Y}_{s2} = -\vec{X}_s; \vec{Z}_{s2} = -\vec{Z}_s$$

This reference frame provides axes which have directions consistent with the orbital motion and the nadir pointing directions. Please note that in this context the nadir direction is not geodetic nadir but geocentric nadir.

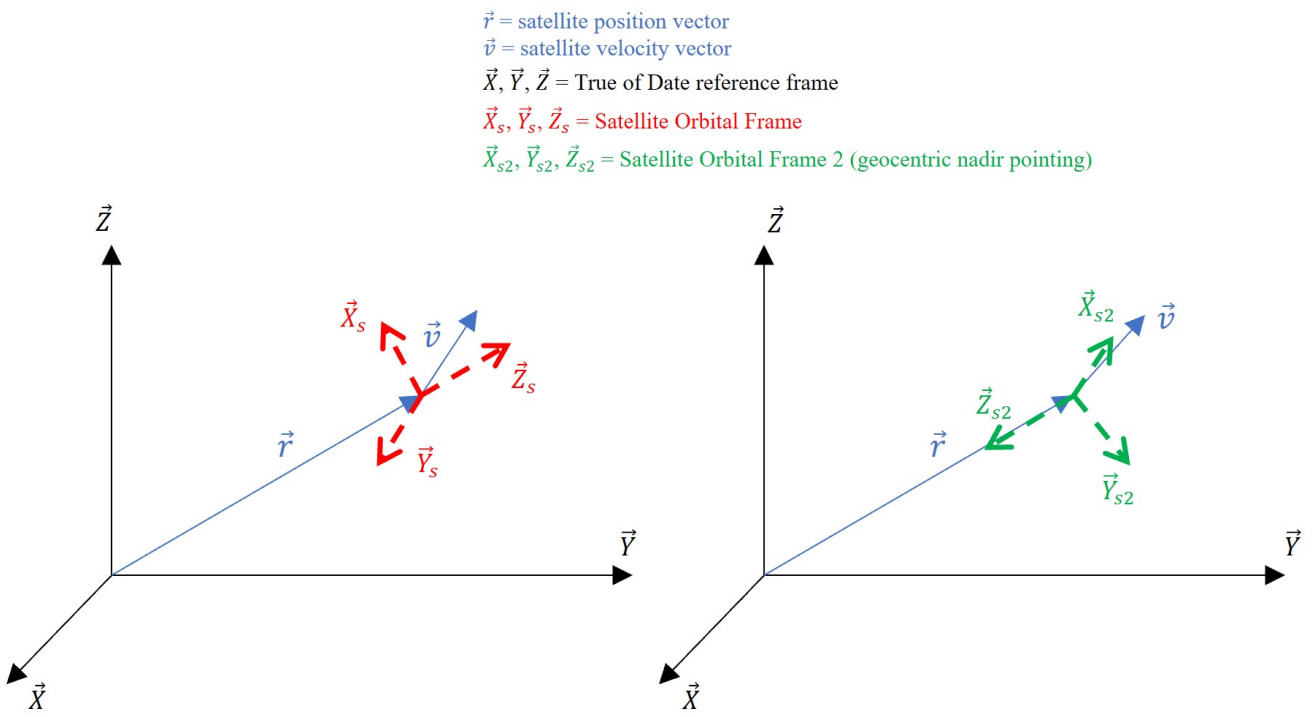

Figure **REF-60**: Satellite Orbital Frames. ($\vec{X}_{s2}$ is in reality not necessarily perfectly aligned with the velocity vector).

Local velocity orbital reference frame

The origin of the Local Orbital Reference Frame, identified by the three axis ($\vec{R}$, $\vec{T}$, $\vec{L}$), is the Spacecraft in-flight centre of mass.
The unit vector $\vec{R}$ (Roulis, Roll) is in the direction of the inertial velocity vector $\vec{v}$:

$$\vec{R} = \frac{\vec{v}}{|\vec{v}|}$$

The unit vector $\vec{T}$ (Tangage, Pitch) is perpendicular to $\vec{R}$ and defined as:

$$\vec{T} = \frac{\vec{R} \wedge \vec{r}}{|\vec{R} \wedge \vec{r}|}$$

where $\vec{r}$ is the vector in the direction of the position vector of the satellite (opposite to the Earth's centre, the geocentre).
The unit vector $\vec{L}$ (Lacet or Yaw) completes the right-handed frame:

$$\vec{L} = \vec{R} \wedge \vec{T}$$

Note that, if the orbit is not perfectly circular, $\vec{L}$ is not necessarily perfectly aligned to the zenith direction. In a similar manner, the Local Orbital Reference Frame is not necessarily aligned with SOF2, since the former is built upon the position vector as primary axis, while the second uses the inertial velocity vector as primary axis.

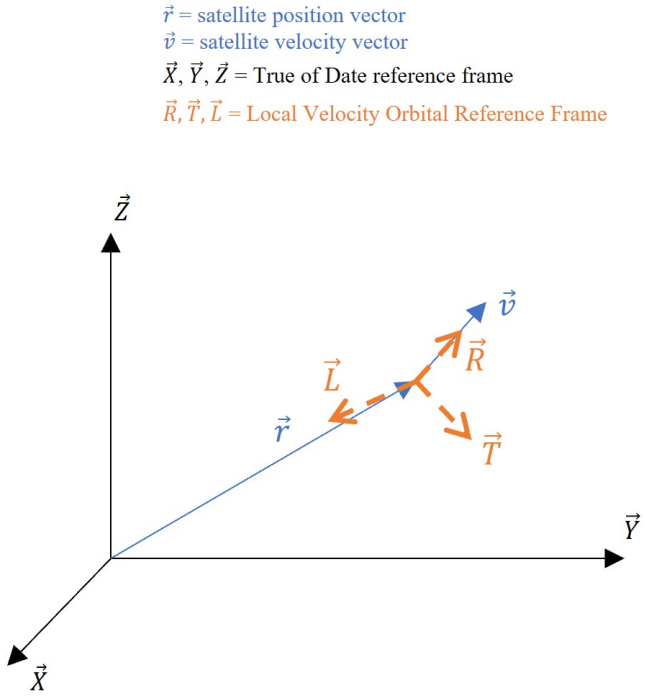

Figure **REF-61**: Local Velocity Orbital Reference Frame

Zero-Doppler Orbital Reference Frame (0-DopRF)

The Zero-Doppler Orbital Reference Frame (0-DopRF), identified by the three axis ($\vec{R}'$, $\vec{T}'$, $\vec{L}'$), has the same definition as the Local Velocity Orbital Reference Frame except that the orbital velocity is corrected for the Earth Rotation and that the geocentric position vector is re-defined as perpendicular to the Earth ellipsoid.
The unit vector $\vec{R}'$ is parallel to $\vec{v'}$ where $\vec{v'}$ is the inertial velocity vector corrected for Earth's rotation.

$$\vec{R}' = \frac{\vec{v'}}{|\vec{v'}|};$$

Note that being $\vec{r}$ the inertial position and $\vec{v}$ the inertial velocity, the inertial velocity corrected for Earth's rotation can be approximated to:

$$\vec{v'} = \vec{v} + \begin{bmatrix} 0 & \omega & 0 \\ -\omega & 0 & 0 \\ 0 & 0 & 0 \end{bmatrix} \vec{r}$$

where $\omega = 0.729211585 \times 10^{-4} rad/s$.
The unit vector $\vec{T}'$ is perpendicular to $\vec{R}'$ and defined as:

$$\vec{T}' = \frac{\vec{R}' \wedge \vec{r'}}{|\vec{R}' \wedge \vec{r'}|}$$

Where $\vec{r'}$ is parallel to the local normal of the Earth's reference ellipsoid (WGS84 model [RD-27]), directed upward and crossing the Spacecraft center of mass. The position vector corrected for Earth's eccentricity can be approximated to:

$$\vec{r'} = \vec{r} + \begin{bmatrix} 0 & 0 & 0 \\ 0 & 0 & 0 \\ 0 & 0 & \beta \end{bmatrix} \vec{r}$$

where $\beta = 0.0060611$

Finally, the unit vector $\vec{L'}$ completes the right-handed frame:

$$\vec{L'} = \vec{R'} \wedge \vec{T'}$$

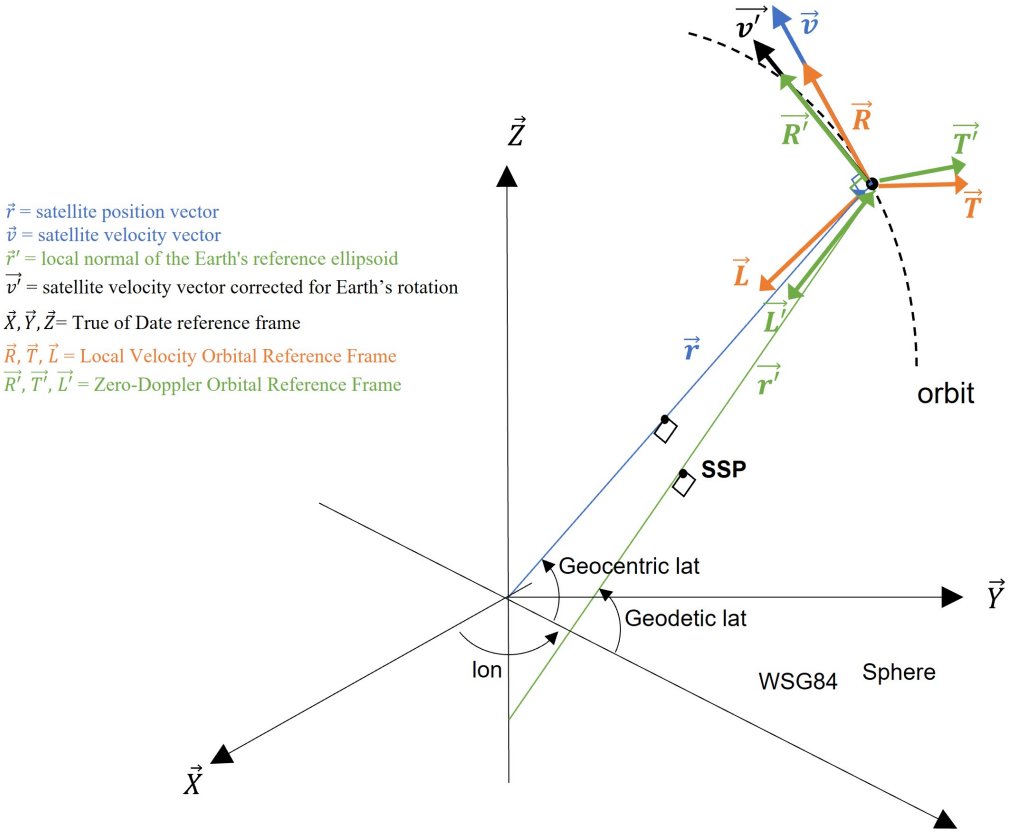

Figure **REF-62**: Local Velocity Orbital Reference Frame and Zero-Doppler Orbital Reference frame.

Local Normal Pointing (LNP) reference frame

The Local Normal Pointing (LPN) reference frame is similar to SOF2 but using as primary target axis the opposite direction of the geodetic nadir $\vec{r'}$ instead of geocentric nadir $\vec{r}$. It can be therefore defined as follows:

$$\vec{Z}_{LPN} = -\frac{\vec{r'}}{|\vec{r'}|}; \vec{Y}_{LPN} = -\frac{\vec{r'} \wedge \vec{v}}{|\vec{r'} \wedge \vec{v}|}; \vec{X}_{LPN} = \vec{Y}_{LPN} \wedge \vec{Z}_{LPN}$$

Yaw Steering Mode (YSM) reference frame

The Yaw Steering Mode (YSM) reference frame is build upon the geodetic nadir $\vec{r'}$ as primary target axis (as done in the LNP reference frame), but uses the inertial velocity vector corrected for Earth's rotation $\vec{v'}$ to define the secondary target. It can be therefore defined as follows:

$$\vec{Z}_{YSM} = -\frac{\vec{r'}}{|\vec{r'}|}; \vec{Y}_{YSM} = -\frac{\vec{r'} \wedge \vec{v'}}{|\vec{r'} \wedge \vec{v'}|}; \vec{X}_{YSM} = \vec{Y}_{YSM} \wedge \vec{Z}_{YSM}$$

D.2. Satellite Nominal Reference Frame

The Satellite Nominal Reference Frame (SNRF) is an ideal right-handed orthogonal attitude frame. The axis definition for this frame depends on the attitude mode and attitude law chosen for the satellite.
The transformation from the Satellite Orbital Frames SOF2 to the SNRF shall be provided by the Prime contractor through the attitude law, using the conventions defined in section $D.5$.
Note also that in pure ideal conditions (i.e. no attitude perturbations, perfect control, etc.) the SRF coincides with the SNRF.

D.3. Satellite Reference Frames

Mechanical Satellite Reference Frame

The Mechanical Satellite Reference Frame (SRF_{mech}) is a right-handed orthogonal body-fixed system of axes with origin (O_{SAT}) located at the center of the launch vehicle interface ring, in the satellite / launcher separation plane at the lower bottom of the satellite. It is fixed to the spacecraft body and invariant for both stowed and deployed configurations.
It is defined by the following axes:

- $\vec{Z}_{SAT}$ is the longitudinal satellite axis, positive upwards in launch configuration.
- $\vec{Y}_{SAT}$ is within the launcher interface plane and is obtained by computing the cross-product between the longitudinal axis of the solar arrays and $\vec{Z}_{SAT}$.
- $\vec{X}_{SAT}$ completes the ortho-normal, right-handed satellite reference frame.

This definition implies that in nominal and ideal conditions, the $\vec{X}_{SAT}$ is approximately oriented as the satellite velocity vector and $\vec{Z}_{SAT}$ is approximately pointed in the direction of nadir, depending on the specific attitude law chosen (i.e. depending on the SNRF definition). However, this is to be interpreted as by design only. In flight the actual direction of geodetic nadir may not be aligned with $\vec{Z}_{SAT}$ since this direction changes with satellite position and attitude as well as due to AOCS errors, whereas the SRF_{mech} remains attached to the structure.

The prime contractor shall use SRF_{mech} as the reference frame for satellite mechanical drawings, CAD models, and in the instrument IRD.

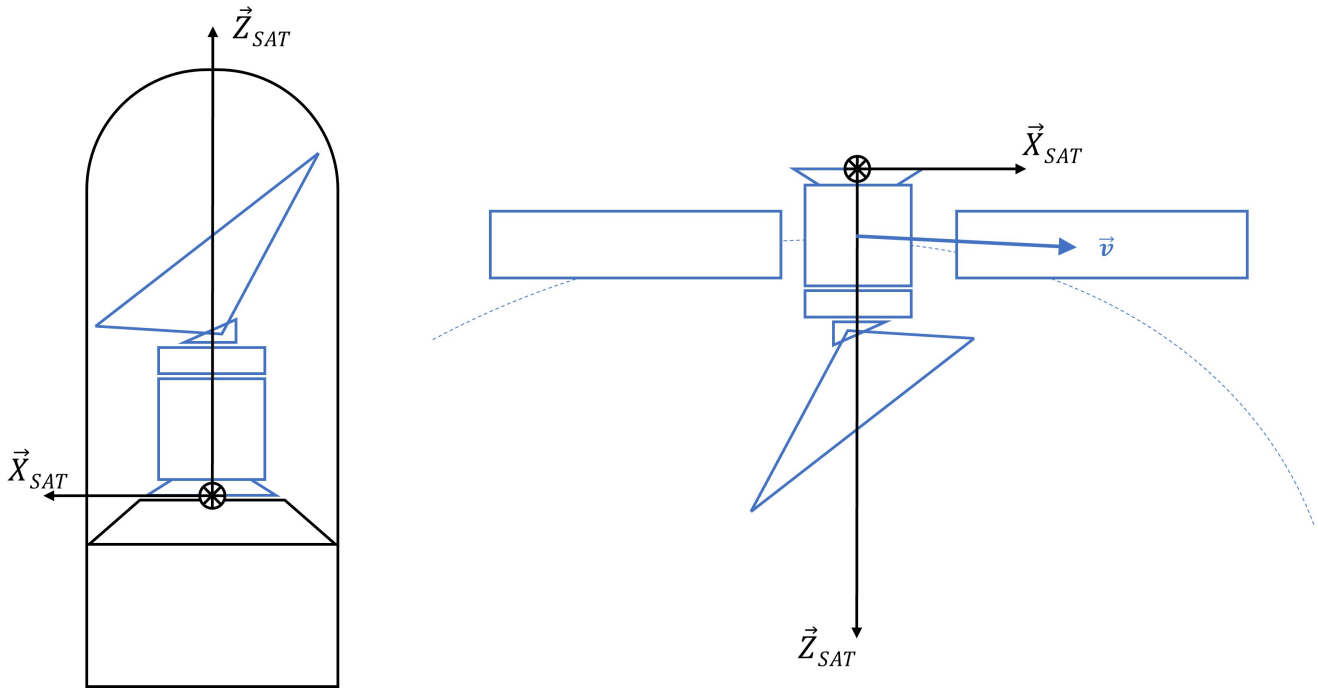

Figure **REF-63**: Illustration of Mechanical Satellite Reference Frame (SRF_{mech}) in launch configuration on the left and in orbit deployed configuration on the right (solar panels configuration is only for illustration purposes).

Center of Gravity Centered Satellite Reference Frame

The Center of Gravity Centered Satellite Reference Frame (SRF_{COG}), is a right-handed orthogonal body-fixed system of axes with origin (O_{COG}) located at the satellite center of gravity. SRF_{COG} is directly derived from SRF_{mech} through a translation in the three orthogonal directions of the frame origin from O_{SAT} to O_{COG} (no rotation expected).

AOCS Satellite Reference Frame

The Attitude and Orbital Control Subsystem SRF (SRF_{AOCS}) corresponds to the satellite actual attitude frame. It is a right-handed orthogonal body-fixed system of axes with origin O_{AOCS}.
O_{AOCS} is expected to be as close as possible to the AOCS reference sensor(s) (e.g. Star Tracker bracket and/or Gyro sensor).
SRF_{AOCS} shall be aligned by design with the satellite nominal reference frame SNRF. This means that any rotation between the two reference frames shall be due to pointing uncertainties or errors.

D.4. Instrument Reference Frames

Static Instrument Reference Frame

The Static Instrument Reference Frame (IRF_{Stat}) is a body mounted reference frame which is fixed with the non-rotating part of the instrument. The IRF_{Stat} is directly derived from the Mechanical Satellite Reference Frame (SRF_{mech}), by applying a translation of the origin (no rotation expected) defined by the payload accommodation on the platform.

Rotating Instrument Reference Frame

The Rotating Instrument Reference Frame (IRF_{Rot}) is attached to the rotary part of the rotary mechanism assembly with $\vec{Z}_{Rot}$ aligned with the rotary mechanism rotation axis. The IRF_{Rot} corresponds to an azimuth rotation φ_{Rot} of the IRF_{Stat} around $\vec{Z}_{Rot}$.
Note that in ideal conditions (i.e. no misalignment, no rotation errors, etc.), the $\vec{Z}_{Stat}$ is parallel to $\vec{Z}_{Rot}$ and φ_{Rot} is equal to the azimuth angle of the actual line of sight.

Antenna RF Reference Frame

The Antenna Radio Frequency Instrument Reference Frame (IRF_{AntRF}) is a reference frame used for the RF characterization of the antenna. Its origin is nominally located on the vertex of the parabola of the instrument reflector. The IRF_{AntRF} is a right-handed orthogonal reference frame, with the first ($\vec{X}_{AntRF}$) and second axis ($\vec{Y}_{AntRF}$) lying on the RF projected aperture plane. The third ($\vec{Z}_{AntRF}$) axis is perpendicular to the RF projected aperture plane and consequently nominally parallel (i.e. assuming no antenna pattern distortions) to the actual line of sight.

In addition, in ideal conditions (i.e. no TED, no mechanical errors, etc.) the IRF_{AntRF} corresponds to the rotation of the elevation angle γ_{Rot} of the IRF_{Rot} around $\vec{Y}_{Rot}$, which implies that the angle between $\vec{Z}_{AntRF}$ and $\vec{X}_{Rot}$ is equal to the elevation angle γ of the actual line of sight.

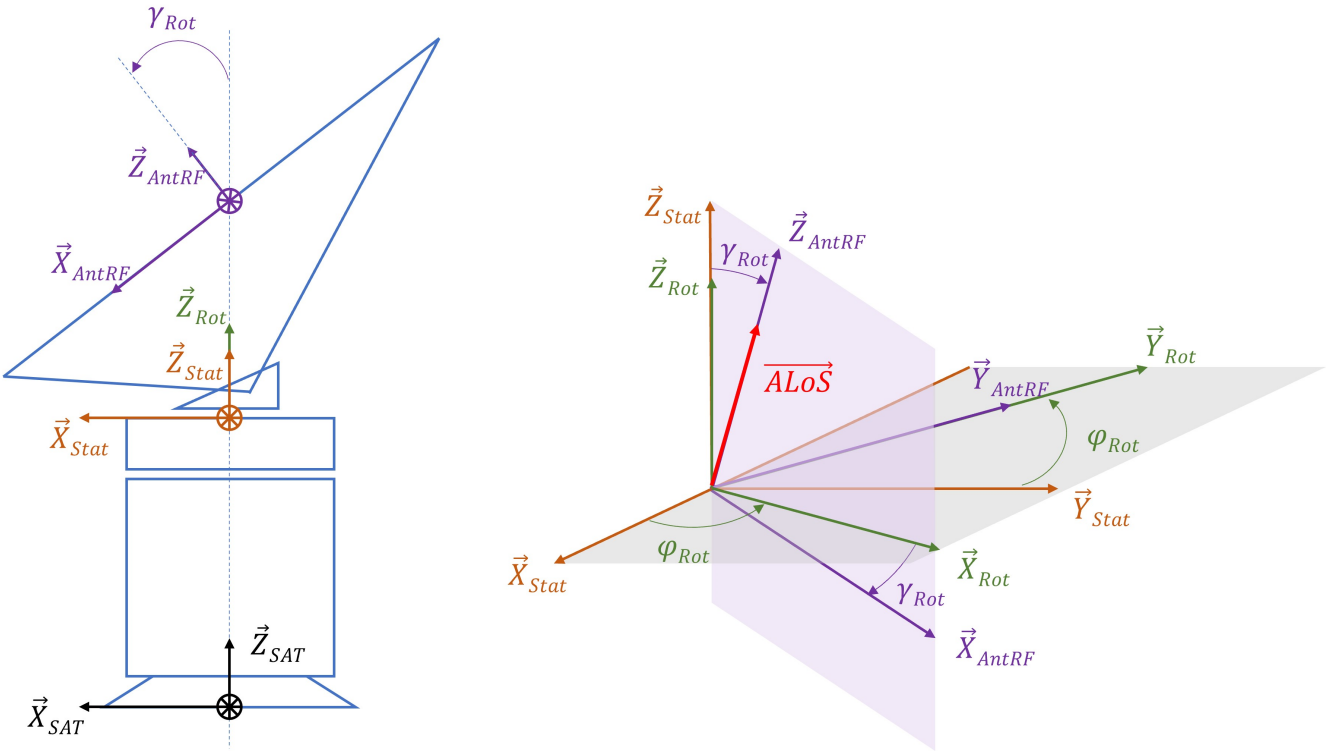

Figure **REF-64**: Illustration of SRF_{mech}, Instruments Reference Frames, i.e. IRF_{Stat}, IRF_{Rot} and IRF_{AntRF}, in nominal and ideal conditions. On the left, the configuration corresponds to $\varphi_{Rot} = 0deg$

It shall be noted that the particular IRF_{Stat} and IRF_{Rot} shown are for illustration only and may have different orientation according to i) the actual accommodation of the instrument, ii) which part of the payload is put in rotation and iii) the flight configuration.

Line of sight

The line of sight of a radar instrument typically represents an axis of symmetry in the antenna radiation pattern, which is often also the direction of peak antenna gain. The WIVERN instrument is a conically scanning Doppler-shift radar. The radiation pattern is defined in the IRF_{AntRF}. Within this frame two definitions for the line of sight are introduced:

- The actual receive beam line of sight ($\vec{ALoS}_{Rx}$) is defined as a virtual axis within the IRF_{AntRF} that is representative for the actual direction of looking for the receive beam.
- The actual transmit beam line of sight ($\vec{ALoS}_{Tx}$) is defined as a virtual axis within the IRF_{AntRF} that is representative for the actual direction of looking for the transmit beam.

All pointing error budgets are calculated with respect to these two axis. There are different ways to define the actual beam line of sight. Within the WIVERN project, it can be defined as the line that connects the origin of the beam reference frame with the centroid of the beam

region delimitated by a power reduction equal to - 3 dB with respect to the peak antenna gain or as the direction of the peak gain of the beam.

D.5. Conventions to describe transformations

Euler Convention and Roll-Pitch-Yaw

The following conventions shall be used to describe with three consecutive elementary rotations a rotation from one reference frame to another.
Rotations shall be intrinsic and around the axes X-$Y^{(1)}$-$Z^{(2)}$ (Tait-Bryan angles) in the following sequence:

- Rotation around X over an angle η (clockwise is positive)
- Rotation around $Y^{(1)}$ over an angle ξ (clockwise is positive)
- Rotation around $Z^{(2)}$ over an angle ζ (clockwise is positive)

Where superscripts $^{(1)}$ and $^{(2)}$ denote axes obtained after the first and second elementary rotations have been applied.

Only when applied to the SOF2 frame, these rotations correspond to consecutive roll, pitch and yaw rotations around body-fixed axes. Roll, pitch and yaw names shall only be used in this context.

The convention specified above differs from the definition of Euler angles specified in [RD-26].

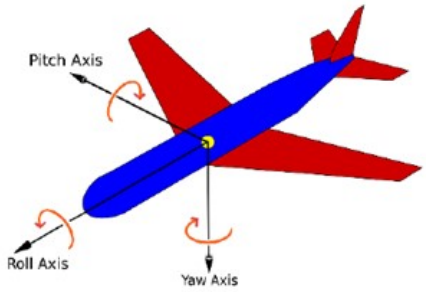

Figure **REF-65**: Sign convention for roll-pitch-yaw angles.

Euler angles shall be used for illustration purposes only. All rotations shall be formally specified using rotation matrices.

Conventions to specify transformation matrices

Transformations between reference frames shall follow the convention of passive (or “alias”) transformations and they shall pre-multiply column vectors.

The transformation from reference frame A to reference frame B is here represented by the transformation matrix R.
This implies that given a point in reference frame A, represented by the column vector $\vec{P}$, then the coordinates in the reference frame B are given by $R \cdot \vec{P}$.
With the Euler convention specified in the previous paragraph, the complete rotation matrix is written following the order from right to left, due to the convention of using passive rotations, as:

$$R = R_Z(\zeta) \cdot R_Y(\xi) \cdot R_X(\eta)$$

where

$$R_X(\eta) = \begin{bmatrix} 1 & 0 & 0 \\ 0 & \cos\eta & \sin\eta \\ 0 & -\sin\eta & \cos\eta \end{bmatrix}; R_Y(\xi) = \begin{bmatrix} \cos\xi & 0 & -\sin\xi \\ 0 & 1 & 0 \\ \sin\xi & 0 & \cos\xi \end{bmatrix}; R_Z(\zeta) = \begin{bmatrix} \cos\zeta & \sin\zeta & 0 \\ -\sin\zeta & \cos\zeta & 0 \\ 0 & 0 & 1 \end{bmatrix}$$

If there is a combination of translation and rotation, the operations sequence shall be specified.

Polar Reference Frame: Azimuth and Elevation

Azimuth (φ) and elevation (γ) angles are defined in any reference frame as follows:

- $X = \cos\varphi \sin\gamma$
- $Y = \sin\varphi \sin\gamma$
- $Z = \cos\gamma$

The look angle is only defined in the reference frame SOF2, when it is synonymous for elevation angle.

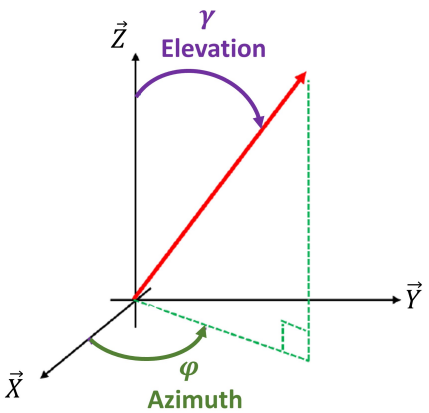

Figure **REF-68**: Polar coordinates

Note: The Greek symbol theta (θ) is not used because it will be used throughout the project to denote incidence angle.

In order to refer to an angle in a specific reference frame, instead of introducing a dedicated definition, a subscript can be used to indicate the reference frame.

D.6. Graphical Synthesis

The following figure provides with a graphical synthesis of the transformations between some of the reference frame previously defined. The prime contractor shall identify all sources of errors, not limited to the main errors indicated in this diagram. Main error sources are included only for the shortest path from SNRF to ALoS. Rotations/translations are indicated for nominal transformations, excluding errors.

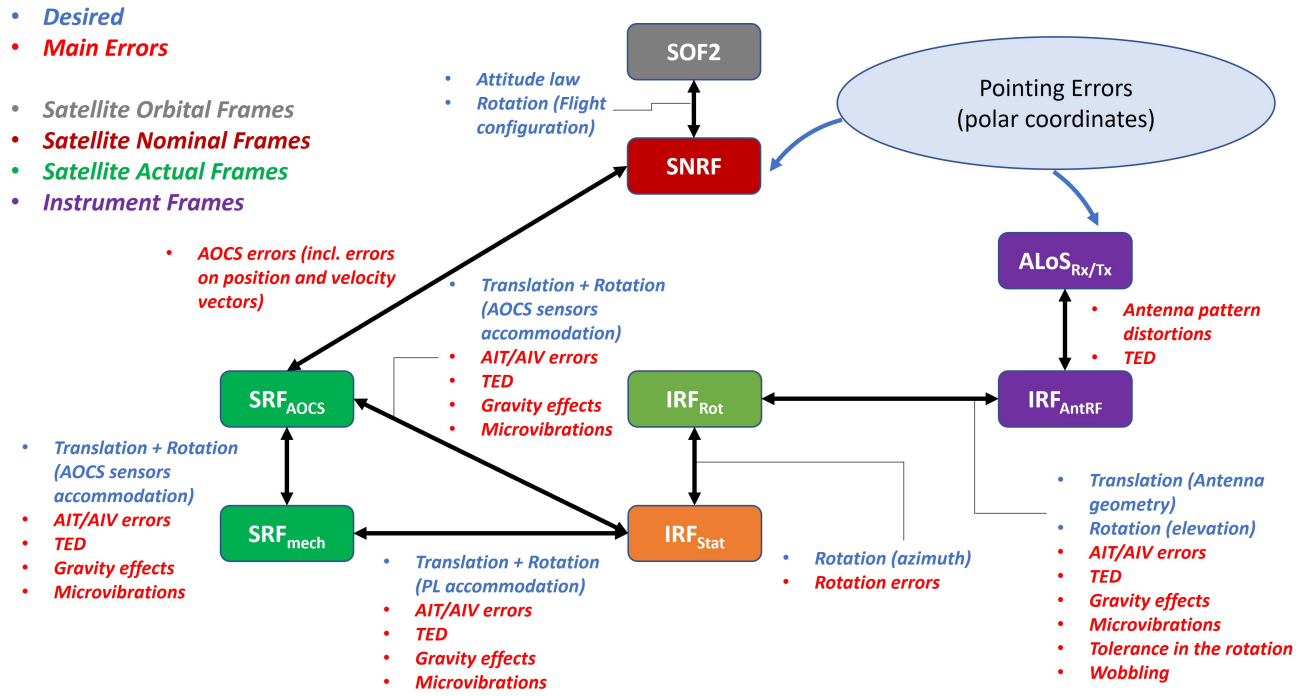

Figure **REF-66**: Overview of reference frame transformations.

D.7. Formulation of pointing errors

The pointing error budgets, whether they are on performance or knowledge, are formulated as errors or uncertainties between the SNRF reference frame and the Actual Line of Sight ($\vec{ALoS}_{Rx/Tx}$) defined in section D.4. The errors shall be expressed as in azimuth and elevation, using the convention from section D.5. The transformation from SNRF to $\vec{ALoS}_{Rx/Tx}$ can be broken down in a chain of transformations as illustrated in Figure REF-66. If the AOCS sensors were located inside the spacecraft, that path would include:

SNRF > SRF_{AOCS} > SRF_{mech} > IRF_{Stat} > IRF_{Rot} > IRF_{AntRF} > $\vec{ALoS}_{Rx/Tx}$

However, in the case of WIVERN, in case the AOCS sensors are located on the static part of the payload, a shorter error path can be obtained:
SNRF > SRF_{AOCS} > IRF_{Stat} > IRF_{Rot} > IRF_{AntRF} > $\vec{ALoS}_{Rx/Tx}$

Following this chain of transformations, the following typical error contributions will be encountered. Note that the allocation of types of error to specific transformations is somewhat arbitrary and only provided as an example. Prime contractor and instrument supplier are expected to come with their own breakdown of the error tree.

- SNRF to SRF_{AOCS}: AOCS errors, including errors on the estimation of satellite position and velocity vectors.
- SRF_{AOCS} to IRF_{Stat} as well as IRF_{Rot} to IRF_{AntRF}: typically including errors that appear as a rotation of the antenna as a whole. These errors can be constant in time, for instance due to gravity effects or AIT errors, or they can be time varying for instance due to thermo-elastic distortions (TED).
- IRF_{Stat} to IRF_{Rot}: typically including errors that affect the ideal conical scanning motion of the antenna beams. These errors can be constant in time, for instance due to a bias in the rotation speed, or they can be time varying for instance due to microvibrations.
- IRF_{AntRF} to $\vec{ALoS}_{Rx/Tx}$: including errors that affect the direction of the peak antenna gain. These errors can be constant in time, for instance due to antenna pattern characterization errors, or they can be time varying for instance due to TED.

For the purpose of end-to-end performance simulations, it is assumed that the antenna patterns are expressed in the IRF_{AntRF}. Any additional distortion to the antenna pattern that would rotate the peak gain away from the z-axis is taken into account by using the actual antenna patterns in the simulation.